UNIVERSITY OF OKLAHOMA

GRADUATE COLLEGE

METHANE MITIGATION IN NATURAL GAS INDUSTRIAL ENGINES: HYDROGEN FUEL BLENDING AND THE INTEGRATION OF CERAMIC ELECTROCHEMICAL REACTORS

A THESIS

SUBMITTED TO THE GRADUATE FACULTY

in partial fulfilment of the requirements for the

Degree of

MASTER OF SCIENCE

By

John Christopher Fisher

Norman, Oklahoma

2025

Downloaded from SHAREOK. Persistent Handle URL: https://hdl.handle.net/11244/341617

METHANE MITIGATION IN NATURAL GAS INDUSTRIAL ENGINES: HYDROGEN FUEL BLENDING AND THE INTEGRATION OF CERAMIC ELECTROCHEMICAL REACTORS

A THESIS APPROVED FOR THE

SCHOOL OF AEROSPACE AND MECHANICAL ENGINEERING

BY THE COMMITTEE CONSISTING OF:

Dr. Pejman Kazempoor, Chair

Dr. Ramkumar Parthasarathy

Dr. Wilson Merchán-Merchán

Dr. Hamidreza Shabgard

©Copyright by JOHN CHRISTOPHER FISHER 2025
All Rights Reserved.

ACKNOWLEDGEMENTS

The last 5 years at the University of Oklahoma have been an unbelievable experience that I could not have done without the support of my friends, family, colleagues, and advisors. I would like to thank my advisor, Dr.Kazempoor, for offering me the opportunity to join his lab and share in his future image of what the renewable energy industry can be when people believe in the future possibilities. Working at the lab for over 3 years provided a purpose to the long nights and early morning spent studying topics that I would have otherwise never learned. I would also like to thank the OU AME faculty for always directing me in the right direction, no matter how difficult it may have seemed at first.

I would like to extend my gratitude to my best friends and roommates Isaac Medina, Landry Vinson, and Raphael Ong that listened and provided me with a mental escape through my undergraduate and graduate education. I would like to thank my colleagues Hugh Nelson and Jaden Norman for making work and school life fun and approachable, and when the topics were not approachable, a common enemy amongst us.

I would like to extend my deepest thanks to my family and partner for always being there when I needed guidance, motivation, and somewhere to escape when work would become overwhelming. To Sara, thank you for listening, supporting, comforting me, and loving me through something I could not do myself.

Table of Contents

Contents

ACKNOWLEDGEMENTS iv

Table of Contents v

List of Tables vi

List of Figures vii

List of Equations x

Abstract: xii

Chapter 1: Introduction 1

Chapter 2: Literature Review 9

Chapter 3: Methodology 16

3.1: Engine Methane Mitigation Technologies 16

3.1.1: Spark Ignition Timing Modification Theory 18

3.1.2: Hydrogen Natural Gas Blending Theory 20

3.1.3: Spark Ignition and Hydrogen Blending Equipment 23

3.1.4: Spark Ignition and Hydrogen Blending Testing Procedures 32

3.1.5: Spark Ignition and Hydrogen Blending Validation Theory and Procedure 33

3.2: PCER Methane Conversion Modeling 34

3.2.1: PCER Theory 35

3.2.2: PCER Modeling Framework 38

3.2.2.1: Mole Balance Model 42

3.2.2.2: Reaction Kinetics Sub Model 44

3.2.2.3: Electrochemical Sub Model 48

3.2.3: PCER Modeling Parameters 54

3.2.3: PCER Model Testing Procedures and Validation 58

3.3: Combined PCER/Engine Modification System Modeling 60

3.3.1: Engine Modeling Methodology and Testing Procedure in HYSYS 60
Chapter 4: Results 62
4.1: Spark Ignition and Hydrogen Blending Results 62
4.1.1: Spark Ignition and Hydrogen Blending Emission Results 64
4.1.1.1: Methane Emissions 64
4.1.1.2: CO_x and NO_x Emissions 70
4.1.2: Spark Ignition and Hydrogen Blending Efficiency Results 76
4.1.3: Spark Ignition and Hydrogen Blending Emission Validation Results 79
4.1.3.1: 55% Load Emissions Analysis for Hydrogen Blending and Spark Timing 79
4.1.3.2: 55% Load Engine Condition Analysis for Hydrogen Blending and Spark Timing 83
4.2: PCER Modeling Results 85
4.2.1: Operating Temperature Impact 85
4.2.2: PCER Flowrate Impact 95
4.2.3: PCER Electrochemical Model 98
4.2.3.1: Electrochemical Operation at Different Operating Temperatures 99
4.2.3.2: Ideal Feedstock Electrochemical Operation at Different Current Densities 102
4.2.3.3: Real World Feedstock Electrochemical Operation at Different Current Densities 112
4.2.4: PCER Validation Data 122
4.3: Aspen HYSYS Modeling Results 122
Chapter 5: Conclusion 125
Citations: 127

List of Tables

Table 1: Zeldovich two-step mechanism for the thermal formation of nitrogen oxide 17
Table 2: AJAX DPC-105 engine specifications [89] 23
Table 3: Equipment utilized in engine testing 25
Table 4: Test parameters for the methane reduction using combined spark ignition timing and blended HNG 32

Table 5: Chemical reactions used in PCER modeling 36
Table 6: Delta Gibbs Free Energy equations for each reaction 46
Table 7: Summary of the reaction kinetics data utilized in the model 47
Table 8: Reaction rate equations utilized in the model 48
Table 9: Model input variable assumptions 54
Table 10: PCER cell geometry 55
Table 11: Emission compounds obtained from the MKS 2030FTIR and NOxO2 amperometric sensors. 56
Table 12: Molar composition for model validation and for DPC105 exhaust stream at 60% load, 0H2%, 11 Degrees BTDC and 60% load, and 20H2%, 11.5 Degrees 57
Table 13: Fuel stream conditions for 60% load testing 62
Table 14: Flow conditions used in the HYSYS model 123
Table 15: HYSYS model and PCER parameters for PCER integration 124

List of Figures

Figure 1: Combustion Chamber Design with Air intake Cutouts 18
Figure 2: Spark Ignition System for an AJAX DPC-105. 19
Figure 3: (a) Pick-up Coil Z-axis slotted bracket, (b) Advancing and Retarding Correlation Diagram 20
Figure 4: (a) Fuel system blending schematic, (b) Natural gas line modification to include an injection line above the angle change in the t-shaped pipe adapter. 21
Figure 5: Aspen HYSYS HNG blending model 22
Figure 6: Volumetric flow rate property for the hydrogen flow rate obtained after setting the product concentration target. 22
Figure 7: AJAX DPC-105 natural gas-fed, two-stroke compressor 24
Figure 8: Engine Operation Schematic 25
Figure 9: Flow meters used in experimentation, (a) Emerson flow meter for natural gas stream, (b) Fox Thermal flow meter for air and/or hydrogen data collection. 27
Figure 10: (left) Mixing tank pressure gauge, (right) hydrogen tank pressure regulator 28
Figure 11: (a) Omega pressure transducer and temperature sensor, (b) Windrock 6400 pressure transducer attachment 29
Figure 12: (a, left) Permanent Magnetic RPM Encoder, (b, right) Windrock Magnetic Encoder 30
Figure 13: MKS analyzer gas stream and equipment 31
Figure 14: NOxCANt amperometric NO_x/O_2 sensor kit to measure oxygen and nitrogen oxides in the engine exhaust stream 31
Figure 15: PCER model operational and structural diagram 35
Figure 16: The geometry of the PCER model 39
Figure 17: Testing procedures for the PCER model 59

Figure 18: Aspen HYSYS engine simulation 61
Figure 19: Natural gas mass flow rates across different hydrogen concentrations and spark ignition timings. The spark timing angles are shown in units of before top Dead center (BTDC). 63
Figure 20: AJAX DPC105 Engine load variation from 60% during testing. 64
Figure 21: methane emission results for hydrogen blending 0-20% mole concentration and ignition timing from 12BTDC to 9BTDC 65
Figure 22: Methane ppm at different spark ignition timing separated by advancing to the left and retarding on the right 67
Figure 23: Change in methane emissions from baseline compared to the hydrogen mole fraction blended into the natural gas stream 68
Figure 24: Percent change in methane emissions for advancing and retarding spark times at hydrogen mole fractions of 0%, 10%, and 20% compared to the baseline angle with no hydrogen addition 69
Figure 25: Mean maximum pressure readings across 251 engine cycles at different spark ignition angle across 0,10, and 20% hydrogen molar fraction 70
Figure 26: Carbon monoxide ppm at 15% O2 across a hydrogen blend mole fraction between 0-20% 71
Figure 27: Carbon dioxide ppm at 15% O2 across a hydrogen blend mole fraction between 0-20% 73
Figure 28: Nitrogen oxides (NOx) ppm emissions at different angles across 0-20% hydrogen mole fraction of blending into natural gas 75
Figure 29: Exhaust temperature vs. blended hydrogen mole fraction 75
Figure 30: Indicated thermal efficiency compared to hydrogen blending mole fraction across different spark timings 77
Figure 31: IMEP compared to the hydrogen blending mole fraction across different ignition spark timing angles 78
Figure 32: Methane emissions in ppm compared to the hydrogen mole fraction blended across spark timing angles 80
Figure 33: Methane emissions compared to a variety of spark timings when the engine fuel is not blended with hydrogen 81
Figure 34: Percent change in methane emissions for advancing and retarding spark times at hydrogen mole fractions of 0%, 10%, and 20% compared to the baseline angle with no hydrogen addition 82
Figure 35: Change in methane emissions compared to the baseline angles across the same hydrogen mole fraction blended into the natural gas stream 83
Figure 36: Exhaust temperatures compared to hydrogen mole fraction blends over a range of spark ignition angles 84
Figure 37: Indicated thermal efficiency compared to the hydrogen mole fraction blend in natural gas over a range of spark timing angles 85

Figure 38: Exit emissions from PCER unit at different temperatures utilizing ideal emissions .. 86
Figure 39: Rate of steam methane reforming along the length of the cell at different temperatures 87
Figure 40: Rate of water gas shift reaction along the length of the cell at different temperatures 88
Figure 41: Rate of methane oxidation along the length of the cell at different temperatures..... 89
Figure 42: Exit emissions from PCER unit at different temperatures utilizing real modified emissions..... 90
Figure 43: Exit emissions from PCER unit at different temperatures utilizing real modified emissions, CO2 and CO enhancement..... 90
Figure 44: Rate of steam methane reforming along the length of the cell at different temperatures 91
Figure 45: Rate of water gas shift reaction along the length of the cell at different temperatures 92
Figure 46: Rate of methane oxidation along the length of the cell at different temperatures..... 93
Figure 47: Temp vs. mole fraction for the modified exhaust emissions with 5% methane added 94
Figure 48: Temp vs. reaction rates for the modified exhaust emissions with 5% methane added 95
Figure 49: GHSV vs. mole fraction from an ideal feed concentration 96
Figure 50: GHSV vs. mole fraction using the modified engine emissions from the engine settings 11.5BTDC with 20% hydrogen addition. 5% methane and 40% water were added for model convergence purposes. 97
Figure 51: Zoomed in GHSV vs. mole fraction using the modified engine emissions from the engine settings 11.5BTDC with 20% hydrogen addition. 5% methane and 40% water were added for model convergence purposes. 98
Figure 52: Temperature vs. operating voltage for an ideal inlet stream at 2,000 a/m^2..... 99
Figure 53: Temperature vs. voltage losses for an ideal inlet stream at 2,000 a/m2..... 100
Figure 54: Temperature vs. operating voltage for a modified real inlet stream at 2,000 a/m2... 101
Figure 55: Temperature vs. voltage losses for a modified real inlet stream at 2,000 a/m2 102
Figure 56: Current density vs. mole fraction for an ideal feed stream at 673K..... 103
Figure 57: Current density vs. operating voltage for an ideal feed stream at 673K 104
Figure 58: Current density vs. reaction rates for an ideal gas feed at 673K 105
Figure 59: Current density vs. voltage losses for an ideal feed stream at 673K..... 105
Figure 60: Current density vs. mole fraction for an ideal feed stream at 873K..... 106
Figure 61: Current density vs. reaction rates for an ideal gas feed at 873K 107
Figure 62: Current density vs. operating voltage for an ideal feed stream at 873K 108
Figure 63: Current density vs. voltage losses for an ideal feed stream at 873K..... 108
Figure 64: Current density vs. mole fraction for an ideal feed stream at 1000K..... 109
Figure 65: Current density vs. reaction rates for an ideal gas feed at 1000K 110
Figure 66: Current density vs. operating voltage for an ideal feed stream at 1000K 111
Figure 67: Current density vs. voltage losses for an ideal feed stream at 1000K..... 111
Figure 68: Current density vs. mole fraction for the modified feed condition at 673K 113
Figure 69: Current density vs. reaction rates for the modified feed case at 673K..... 114

Figure 70: Current density vs. operating voltage with a modified cell feed at 673K 115
Figure 71: Current density vs. voltage losses with a modified cell feed operating at 673K 116
Figure 72: Current density vs. mole fraction for the modified feed condition at 873K 117
Figure 73: Current density vs. reaction rates for the modified feed case at 873K..... 117
Figure 74: : Current density vs. operating voltage with a modified cell feed at 873K..... 118
Figure 75: Current density vs. voltage losses with a modified cell feed operating at 873K 118
Figure 76: Current density vs. mole fraction for the modified feed condition at 1000K 119
Figure 77: Current density vs. reaction rates for the modified feed case at 1000K..... 120
Figure 78: Current density vs. operating voltage with a modified cell feed at 1000K..... 120
Figure 79: Current density vs. voltage losses with a modified cell feed operating at 1000K 121
Figure 80: Temperature vs. methane conversion validation dataset matching this work to Palma et. al. [116] 122
Figure 81: Aspen HYSYS engine model 123

List of Equations

Equation 1: Stoichiometric combustion of methane 16
Equation 2: Half reaction mechanism for the Incomplete combustion of methane..... 17
Equation 3: Load percentage calculation 26
Equation 4: Dry basis emission conversion [97] 33
Equation 5: 15% O2 conversion from operational oxygen content [97] 33
Equation 6: Indicated thermal efficiency equation [97] 34
Equation 7: Indicated mean effective pressure equation [97]..... 34
Equation 8: methane oxidation reaction stoichiometry 37
Equation 9: Steam Methane Reforming Stoichiometry 37
Equation 10: Partial reaction for steam methane reforming over a metal catalyst [111] 37
Equation 11: Water Gas Shift reaction stoichiometry 38
Equation 12: Hydrogen Evolution Reaction stoichiometry 38
Equation 13: Cell active area equation 40
Equation 14: Surface area of the anode equation..... 40
Equation 15: Interconnect area 40
Equation 16: Fuel flowrate across the anode in units of mass flow (kg/s) 41
Equation 17: Mass of catalyst calculation 41
Equation 18: Volume of the anode 41
Equation 19: Conversion of particle density to bulk density..... 41
Equation 20: inlet molar flow per compound 42
Equation 21: Moles for each compound across the cell 42
Equation 22: Concentration along the cell length for each compound..... 44
Equation 23: Mole fraction for a specific compound 44
Equation 24: Partial Pressure for a specific compound 44
Equation 25: Power Law elementary rate equation [115] 45

Equation 26: Arrhenius Equation [107] 45
Equation 27: Equilibrium reaction constant for a reaction used in the model 46
Equation 28: Nernst Equation for an electrolyzer[78], [118] 49
Equation 29: Operating current density 49
Equation 30: Incremented active area along the length of the cell 49
Equation 31: Cell voltage accounting for activation, ohmic, and concentration losses 50
Equation 32: Ohmic overpotential makeup equation 50
Equation 33: resistivity of the PEN structure [122] 50
Equation 34: resistance in pen structure equation [122] 51
Equation 35: Ohmic overpotential of the PEN structure equation 51
Equation 36: Equation to obtain ohmic losses from interconnects in volts 51
Equation 37: Area-specific resistance for nickel-coated metallic interconnect 51
Equation 38: Total activation energy equation 51
Equation 39: overpotential calculation for the anode using the Butler-Volmer Equation 52
Equation 40: overpotential calculation for the cathode using the Butler-Volmer Equation 52
Equation 41: General equation for the exchange current density 52
Equation 42: Exchange current density for the anode made of Ni/CeO2 52
Equation 43: Exchange current density for the cathode made of BCZYYb 53
Equation 44: Concentration overpotential equation 53
Equation 45: Triple phase boundary pressure for water 53
Equation 46: Triple phase boundary pressure for oxygen 53
Equation 47: Triple phase boundary pressure for hydrogen 54
Equation 48: Parts per million (PPM) to percent molar composition conversion equation 56
Equation 49: Calculation used to find the molar concentrations of the DPC105 57

Abstract:

Methane emissions are one of the primary emissions causing global warming. Natural gas-fed industrial engines are one of the key drivers in excessive methane emissions due to partial load operations and combustion inefficiencies that can be controlled with modern methane mitigation strategies. In this thesis engine-based and post-combustion methane mitigation strategies are analyzed including spark ignition timing, hydrogen blending, and post-combustion protonic ceramic electrochemical cells (PCERs). The spark ignition timing is used to control the ignition time of the fuel and the electrochemical cells are considered for the conversion of exhaust methane into hydrogen. Hydrogen blending into natural gas is studied at 0%, 10%, and 20% hydrogen mole fraction and an engine load of 60%. The hydrogen mole fraction is calculated using an Aspen HYSYS model of the engine. The addition of hydrogen into the natural gas stream has resulted in a methane emission reduction of 16.2% and 35.2%. Modification of the ignition spark timing is conducted for the angles of 9°BTDC, 11°BTDC, 11.5°BTDC, and 12°BTDC, with the baseline angle being 11°BTDC. A significant methane emission reduction of 56.4% and 60.9% is observed at 11.5°BTDC, and 12°BTDC respectively due to an increase in combustion efficiency. The hydrogen blending and spark ignition are combined to obtain a methane reduction of up to 73% by improving thermal efficiency, promoting flame propagation, and reducing the methane content in the feed fuel. To remove all of the exhausted methane and convert CO to CO_2 while obtaining a high-value chemical, an electrochemical cell is proposed as a post-combustion catalyst. The PCER model utilized a tubular, direct pass construction without an internal support tube. The model was constructed in engineering equation solver (EES) using a mole and electrochemical balance using a Ni/CeO_2 anode, Ni BCZY electrolyte, and Ni/BCZY cathode. The PCER model was able to obtain

complete methane conversion when operating at 2,000-5,000 A/m^2 and a temperature between 673-780K when being fueled with realistic engine emissions. The technology developed here shows promising solutions for reducing and mitigating methane emissions from industrial engines and combustion devices.

Chapter 1: Introduction

Global warming caused by greenhouse gas emissions has caused more extreme weather fluctuations [1]. These weather events have and will continue to create more destructive flooding events, droughts, and an increase in ocean temperatures [1, 2]. The rise in ocean and global temperatures have begun to melt the glacier mountains located primarily in Antarctica and Greenland, but can also be observed in parts of North America and Asia [3, 4, 5]. This melting was studied on the mountain glaciers of Corbassière Switzerland in a paper published January 2024 by Huber et. al. [6]. In the study, Huber utilized the aerosol content change and ratio of oxygen isotope ^{16}O to ^{18}O called Delta-O-18 from ice cores as paleotemperature proxy data to predict past temperatures and structural stability at the peak of the glacier [7, 8]. Huber identified an instability in the ice cores from 2020 when compared to 2018, finding proof of more melting in the summer that then limited the winter freezing effects due to the higher latent heat storage deeper in the ice core. This melting was validated by studying the release of NH_4 (methane), NO_3 (nitrate), and SO_4 (sulfate) from the ice core, finding a much lower content of these gases in the 2020 core than the 2018 core. This study highlights the speed and scale that global warming is having on the planet.

Greenhouse gases are the primary cause of global warming, with human activities becoming the primary producer of these greenhouse gases since the mid-20th century [9]. The primary greenhouse gases are carbon dioxide (CO_2), methane (CH_4), and nitrous oxide (N_2O), and fluorinated gases. The Environmental Protection Agency (EPA) identified that carbon dioxide, methane, nitrous oxide, and fluorinated gases made up 79.7%, 11.1%, 6.1%, and 3.1% of the total 2022 United States emissions respectively [10]. Although carbon dioxide makes up most of the greenhouse gases present in the atmosphere, methane was found to be 28 times more

potent than carbon dioxide for trapping heat in the atmosphere [11]. Methane also has a much shorter lifetime of between 7-12 years in the atmosphere when compared to the hundreds of years that carbon dioxide resides in the earth's atmosphere. A reduction in methane emissions will reduce global warmer at a quicker rate due to methane's shorter lifespan. [12].

The United States Environmental Protection Agency implemented mandatory reporting of greenhouse gas emissions, which accounts for around 8,000 facilities [13]. In addition to the reporting standards, a waste emission charge was instated in August of 2022 as part of the Inflation Reduction Act and regulations were proposed in January of 2024. The proposed regulations would limit waste greenhouse gas emissions higher than 25,000 metric tons of carbon dioxide equivalent (MTCO2e) by charging $900, $1,200, and $1,500 dollars per metric tons of waste greenhouse gas emission over 2024, 2025, and 2026 respectively [14]. The definition of waste emissions depends on the use, scale, and application, with onshore transport of natural gas having a different threshold than a natural gas processing and refining facility.

Human activities such as agriculture, energy, manufacturing, and waste management make up 50-65% of total global methane emissions. In the United States, Agriculture makes up around 34% of methane emissions from manure management and livestock-produce methane. As livestock such as sheep and cattle digest food, they naturally emit methane as a biproduct of enteric fermentation, making up 25% of U.S methane emissions [10]. Agricultural sources of methane would be difficult to reduce without harming U.S food security. The United States Congressional Budget Office theorized that the U.S population between 2024 and 2054 would grow from 342 million to around 383 million respectively [15]. Along with the U.S population growth, foreign exports of beef, poultry, and pork between 1990 and 2024 grew from around 2 billion pounds to over 19 billion pounds of meat product respectively [16]. With the growth in

the U.S population and the increasing meat export industry, the reduction of livestock for methane mitigation would not be the most effective industry to cut down on. Landfills and flooded lands such as swamps cause 16% and 6% of United States methane emissions respectively. Swamps and landfills both emit methane through the decomposition of the trash and/or natural plant matter found in these environments. The move for reducing landfills has already been in effect, with the recycling rate of total waste increasing from 6.4% to 32.1% between 1960 and 2018 [17]. Reducing methane emissions from swamps is not necessary, as it is a natural phenomenon that must occur to continue the carbon cycle [18]. The energy and industrial sectors are the second largest source of U.S methane emissions, with natural gas and petroleum systems making up 28% of U.S methane emissions [10]. The EPA identified the industrial processes and production sector as having methane levels less than 0.05MMTCO_2 Eq. in the production of carbide, ferroalloys, iron, steel, and petrochemicals [19]. In comparison, the energy and oil sectors account for 37% of total U.S methane emissions and 40.2% of all U.S anthropogenic methane emissions in 2022. If we look at the transmission, processing, and production of oil and gas within the energy sector, we see that reciprocating compressors make up 30%, 6%, and 11% of total methane emissions respectively [20]. In total, compressors within the energy sector make up 3.56% of all U.S methane emissions in 2022. Compressor stations are utilized by the oil and gas industry to provide continuous pipeline pressure for long-distance product transportation. In the United States, the number of compressor stations has increased from 1,730 to 2,002 stations between the years of 1990 and 2022. An estimated number of 7,688 compressors are in operation between these compressor stations, with the count of reciprocating engines decreasing from 6,956 to 4,965 and the number of centrifugal compressors increasing from 698 to 2,723 as of 2022 [21]. At the current scale, replacing all natural gas compressors for

modern four-stroke or centrifugal systems is not financially or logistically realistic within a short period of time. At the same time, a rise in emission restrictions for natural-gas-fed systems has brought a need for methods to reduce methane emissions from these large-scale, natural gas fed compressors.

Methane-emitting systems that utilize combustion such as reciprocating compressors can be modified from the original design to reduce methane emissions by modifying and/or adding pre- or post-combustion systems. For pre-combustion modifications, the air-to-fuel ratio (AFR), spark ignition timing and inlet fuel composition can all be changed to reduce methane emissions. The AFR system modifies the ratio between moles of air to moles of fuel entering the engine. The air-to-fuel ratio is modified to reach either a lean burning condition with excess air after combustion, a rich burning process with an excess of hydrocarbon after combustion, or a stoichiometric combustion condition where both the moles of fuel and air are balanced with no excess [22]. If the system is operating in a lean configuration, the unutilized air will absorb heat from the combustion process, leading to incomplete combustion. This lean condition leads to more VOCs, Carbon Monoxide, and excess methane. On the other hand, a rich-burning condition leads to an incomplete combustion of the input hydrocarbon fuel, leading to a direct exhaust of the hydrocarbon post-combustion. In order to reduce carbon emissions with an AFR manipulation, the goal would be to get as close as possible to a stoichiometric combustion condition.

The next pre-combustion system is to modify the spark ignition timing of the engine to make the air and fuel mixture combust earlier or later than the original setting by the manufacturer. When the spark timing is set to cause combustion before the initial engine setting, it is called advancing the timing, while setting the spark timing to set off the combustion reaction

later is called retarding the timing. When the timing is retarded, the piston moves further in the combustion chamber, increasing the volume of the combustion chamber. This condition reduces the chance of knocking, decreases the power output, and causes a higher emissions output. Knocking occurs when the fuel and air mixture combust before the piston reaches the top of the rotation cycle, causing the combusted fuel mixture to push the crank shaft in the opposite direction. Stopping the knocking phenomena is the primary goal of retarding the ignition timing, and it can also be used when a fuel flame propagation speed is higher in fuel blending conditions. Advancing the spark timing causes the air and fuel mixture to combust before the prescribed timing by the manufacturer. Advancing the timing can reduce the emissions in an engine by providing more volume, and therefore, time for the fuel and air mixture to completely combust. Advancing the spark timing makes the engine more prone to knocking. Additionally, the smaller volume at the time of sparking leads to higher temperatures and pressures within the combustion chamber that may be outside of the material's operating conditions. Advancing the timing of the engine is used when changing the fuel composition to a faster-propagating flame, or when the prescribed timing by the manufacturer is selected for long-term, non-stop operation without consideration for the exhaust emissions.

The final way of modifying the pre-combustion conditions of an engine is to change the fuel composition entering the engine. As the air and fuel mixture is ignited with either an electric spark or through pressure, the rate at which the combustion reaction occurs will depend on the hydrocarbon utilized. Each fuel has a different flame propagation speed and laminar flame speed, along with differing emissions post-combustion. Flame propagation speed is the rate of growth that the flame front experiences relative to the initial point of reference. Laminar flame speed, also called burn velocity, is the propagation velocity of the fuel mixture present in the

combustion chamber relative to the flame front [23, 24]. Natural gas and liquefied petroleum gas have a laminar flame speed of 34 cm/s and 38.25 cm/s respectively, while hydrogen has a flame speed of 275 cm/s at 1atm and 293K [25]. The composition of the inlet fuel of an engine can be blended to include faster flame speed fuels such as hydrogen to obtain complete combustion in natural gas and petroleum fuels [26, 27]. The blending of hydrogen into natural gas-fed engines reduces carbon oxides, nitrogen oxides, and methane emissions [28]. This reduction in emissions is observed because hydrogen fuel lacks a carbon bond commonly found in hydrocarbon fuels, reducing the production of carbon oxides and reducing or eliminating methane exhaust from the engine.

Post-combustion emission reduction systems attempt to either recirculate or convert the excess emissions emitted from the engine. Exhaust gas recirculation (EGR) inputs a portion of the exhaust gas stream into the inlet air-to-fuel mixture to combust the unutilized fuel and reduce the temperature of the exhaust within diluents such as carbon oxides and water [29]. EGR is utilized in heavy-duty transportation systems for marine or freight industries to reduce nitrogen oxides and excess unburned fuel emissions [30]. The other approach to post-combustion emission reduction is to convert harmful emissions to less potent emissions using a heterogenous catalyst. A heterogenous catalyst acts as a catalyst for a reactant while being in a different phase [31]. Diesel and gasoline engines both utilize a catalyst-impregnated monolith made of some form of porous alumina as a support structure, with the catalytic material differing by the fuel used [32, 33]. Gasoline three-way catalysts utilize platinum, palladium, and/or rhodium to convert CO to CO_2, reduce NO to N_2, and the reduction of unburnt fuels [34]. For diesel systems, platinum group metals are utilized in a diesel oxidation catalyst for the oxidation of unburned hydrocarbons, along with the reduction of ammonia and NO_x. For NO_x targeted emissions

reduction in diesel systems, a selective catalytic reduction system (SCR) is employed where ammonia-based urea is injected into the exhaust stream over a vanadium oxide, iron, or copper catalyst. The SCR system is implemented after the diesel oxidation catalyst in cases where standard diesel oxidation catalysts are not enough to meet emission regulation [35]. The use of electrochemical cells for post-combustion carbon capture is a novel and crucial field in carbon reduction. Electrochemical cells rely on chemical and electrical power, with a fuel cell producing power from a hydrogen and/or hydrocarbon feedstock while an electrolyzer produces hydrogen and/or hydrocarbon feedstock with the input of electrical power. The exact feedstocks and reactions depend on the construction, material, and type of electrochemical cell. Protonic Ceramic Electrochemical Cells (PCEC) are a type of electrochemical cell that utilize a proton-conducting electrolyte materials and utilizes a ceramic support [36]. PCECs have a lower migration barrier than oxygen-driven electrochemical cells, allowing protonic ceramic electrochemical cells to operate at a lower temperature while sustaining the required activation energy for cell function [37]. Protonic ceramic electrochemical cells have internal reforming, allowing the cell to utilize both hydrocarbon fuels and alcohol fuels as feedstocks. Protonic cells that reduce hydrocarbons with an input of water, oxygen, and power to produce hydrogen are called Protonic Ceramic Electrochemical Reactors (PCER). PCERs can be used to convert excess methane emissions and carbon monoxide (CO) into carbon dioxide (CO_2) while producing hydrogen (H_2) as a value-added product.

The challenge for reducing greenhouse gas emissions from industrial engines stems from the scale in which they are used today, which also makes them a great target for reducing greenhouse gas emissions. Implementing pre- and post-combustion methane-reduction systems to industrial engines allows for the augmentation and adaptation of current combustion engines.

This approach of modification over replacement allows for a quicker methane reduction strategy while sustaining our current industrial architecture. When implementing these technologies, combining pre- and post-combustion systems into one industrial engine can bring greater efficiency, longevity, and balance to the operation of the engine and the integrated methane-reducing technologies. In this thesis, a combination of hydrogen blending, ignition timing, and protonic ceramic electrochemical reactors will be used to reduce methane emissions from an integral two-stroke natural gas compressor. The blending of hydrogen into natural gas and the ignition timing is tested experimentally on an AJAX DPC-105 compressor. The protonic ceramic electrochemical cell is mathematically modeled to simulate chemical conversion and cell operating conditions. A Balance of Plant (BOP) model is developed in Aspen HYSYS to simulate both the operating conditions and the recirculation of the produced hydrogen from the PCER unit.

Chapter 2: Literature Review

The study of integrated methane mitigation strategies into one study requires literature for individual technologies and any attempts to combine various methane reduction technologies. In this literature review we will look at the modification of engine conditions, the modeling of electrochemical cells, and the combination of various methane reduction strategies. The modification of engine conditions includes changing the feedstock through blending fuels, modifying the air to fuel ratio, changing the fuel injection timing, and changing the spark timing.

Natural gas blended with hydrogen is the primary focus for this section, but the blending of ethanol, gasoline, diesel, biofuels, and ammonia with hydrogen were all observed [38] - [42]. The use of blended natural gas and hydrogen (HNG) is a widely studied field [43] - [57]. We can further differentiate these studies by focusing on uncompressed natural gas [43, 47, 50, 51, 56]. Moreno et. al. studied the impact that blending hydrogen and natural gas at a content of 0, 10, 30, and 50% hydrogen into a 4-stroke, 2-piston engine would have on the thermal efficiency and pollutant emissions. The ignition timing was kept the same in the tests, while equivalence ratios of 1, 0.8, and 0.7 were tested. Moreno found that a blend of 30% hydrogen and 70% natural gas with an equivalence ratio of 0.8 was able to reduce NO_x and CO_2 emissions while sustaining similar Brake Thermal Efficiency [43]. Ingo et. al. studied the performance and emissions of a spark-ignition (SI) engine when using HNG. The researchers kept a constant spark ignition timing and used hydrogen contents of 0, 10, 15, 20, and 25% in the blended HNG fuel. Ingo identified a reduction in hydrocarbon, carbon monoxide, and carbon dioxide emissions at all tested hydrogen contents, along with a faster flame propagation at higher hydrogen contents in the fuel [51]. The engine performance portion of this thesis will be conducting similar experiments to the highlighted studies, with the difference being a smaller hydrogen content of 0,

10, and 20% hydrogen and an emphasis on emissions including methane specifically, carbon oxides, and nitrogen oxides that were not discussed in the previously mentioned studies. A vital difference in this thesis is the use of a two-stroke engine for experimental data, with all papers found discussing hydrogen blending and ignition timing utilized a 4-stroke engine.

If we focus more on the spark ignition timing and less on the inlet fuel conditions, various studies have analyzed spark ignition timing and hydrogen blending from an engine [38, 41, 46, 47, 48, 51, 57, 58]. Nitnaware et. al. studied the impact that maximum brake torque spark ignition timing would have on an engine running on blended hydrogen and compressed natural gas (HCNG). Researchers modified the revolutions per minute (rpm), the HCNG contents by 5% for 0-15% hydrogen, the fuel injection pressure, and the equivalence ratio. Nitnaware observed that a 5% hydrogen blend at 2500rpm allowed for a compromise between nitrogen oxides emissions and engine performance. They observed both a reduction in carbon monoxide and an increase in hydrocarbon and NOx emissions. Ichikawa studied the use of a retrofit kit that would replace natural gas as a feedstock. They modified the spark ignition timing of the hydrogen to match the crank angle at which the natural gas mass fraction was 50% burned. Ichikawa identified a NO_x emission reduction of 25% and a thermal efficiency improvement of 2% [50]. Nitnaware et. al. and Ichikawa modified the spark ignition timing to meet a specific fuel and/or engine condition, while this thesis advances and retards spark ignition timing more generally to identify emission reductions. Additionally, this thesis keeps the engine at set load conditions instead of consistent full load.

With the primary focus of this thesis focusing on combining multiple methane mitigation strategies, a review surrounding this combined system is conducted. The use of exhaust gas recirculation (EGR), spark ignition timing, and HNG blending were the only combined methane

reduction systems that were found in the literature [59] - [61]. The idea proposed by Hu et. al. is to use hydrogen in natural gas engines that utilize EGR as a way of regaining engine power losses that are encountered when using higher levels of EGR. Hu et. al. tested 0-40% hydrogen content HNG in increments of 10%, EGR rates of 0-40% in increments of 5%, and an observed range of spark ignition timing from 15-65BTDC. Hu et. al. found that advanced ignition timing was ideal for an increased EGR rate, and that the introduction of hydrogen allowed for less advancement of the timing [60]. This thesis analyzes spark ignition timing and the blending of hydrogen into natural gas like the observed papers, but EGR is not considered. Outside of EGR, this thesis uses 0-20% H2 blends at a set engine load and spark timing, while Hu et. al. used 0-40% blends at a target ignition timing to reach maximum load conditions. Hu et. al. utilized a 3-piston, 4-stroke engine while this thesis focuses on a single-piston, 2-stroke engine. Outside of direct engine modifications to reduce methane emissions, this thesis proposes the use of a post-combustion protonic ceramic electrochemical reactor (PCER) to reduce exhausted methane emissions. The following section with review literature surrounding the modeling of electrochemical cells for methane reduction.

Electrochemical cells utilize electrical and chemical energy to either produce power or to convert chemicals into a more desired product. Solid Oxide Electrochemical Cells (SOEC) and Protonic Ceramic Electrochemical cells (PCEC) are utilized when converting hydrocarbons because of their high operating temperatures. SOECS operate at 800-1000℃ and PCECs operate at 500-700℃, allowing for internal reforming to occur in the cell [62, 63]. SOEC models utilize oxygen (O-SOEC) for the production and transportation of hydrogen, but these models have been modified to use protons (P-SOEC) for the transport and production of hydrogen [64] - [66]. The term proton conducting solid oxide electrochemical cells refers to a high-temperature cell

that uses an electrolyte that is targeted at proton transport, while sustaining the same solid oxide and/or ceramic oxide membrane [67]. Protonic ceramic electrochemical cells are a specific design of P-SOECs that use proton-conducting ceramics, operate at intermediate temperatures under 700°C, and use proton transport only [68]. Protonic Ceramic Electrochemical Reactors (PCER) are a specific type of PCECs that are designed specifically for chemical manufacturing. Proton Membrane Reactors (PMR) are similar to PCERs, but the literature for PMRs may have them using P-SOEC materials and/or operate at temperatures higher than what would be traditionally considered PCECs [69] - [72]. This thesis focuses on methane conversion using tubular protonic ceramic electrochemical reactors, so PCRs that utilize the same feedstock and chemical reactions will be called PCERs. An emphasis in this literature review will be made on identifying operating temperatures for PCER studies to emphasize the distinction between this thesis and the cited study.

Hydrogen, ammonia, methane, methanol and ethane have all been used as fuel in the modeling and construction of protonic ceramic electrochemical cells [73] - [77]. The use and/or production of these fuels is dependent on the configuration, with a fuel cell configuration utilizing the fuels to produce electrical power, while an electrolyzer configuration requires an input of electrical power. The modeling and production of protonic ceramic fuel cells is targeted chemical manufacturing and power production capabilities [76] - [79]. Lei et. al. constructed and tested a PCFC that produced electricity and ethylene when fueled with ethane. The cell used a BCZYYb electrolyte, a LSCF cathode, and a PSFNCu anode. The cell was able to achieve a power density of 200 mW cm^{-2} and an ethylene yield of 41.6% at 750°C [77]. Norman et. al. developed a mathematical PCFC model to simulate the conversion of methane to benzene while

producing power. The model utilized a Mo/ZSM-5 catalyst and Langmuir-Hinshelwood expressions for kinetic modeling. The model achieved 18% methane conversion and 70% benzene selectivity when operating at 700℃. Research in modeling and developing protonic ceramic electrolyzer cells has been focused on chemical production through the use of either hydrogen or methane [69, 70, 71, 72, 74, 80, 81, 82]. Li et. al. developed a 2D numerical model to simulate the production of hydrogen in a PCEC using a cell input of air and water. The modeled cell utilized a BCZYYb electrolyte, a BCFZY anode, and a Ni-BCZYYb cathode. Le et. al. obtained a faradaic efficiency of 82% and a current density of $0.4 cm^{-2}$ at 600℃. Naji et. al. developed a 2D model PCER using OpenFOAM that converts methane to carbon dioxide (CO_2). The modeled cell utilized a BCZY electrolyte with a Ni-BCZY anode and cathode. The model cell operated at 800℃ and utilized a methane concentration of 23.4%. Naji et. al. was able to obtain a methane conversion of 99.7% at an operating current density of 0.375 A/cm^2 [70]. Clark et. al. constructed and modeled a PCER unit fueled by ammonia (CH_3), methane (CH_4), and biogas to produce hydrogen with a CO_2 exhaust. They manufactured a 36-cell reactor stack utilizing a BZCY electrolyte, a Ni-BCZY anode, and a Ni-BZCY cathode. The PCER stack was modeled using a Multiphysics simulation operating at 750℃ , a mean current density of 0.6 A/cm^2, and a methane concentration of 28.6%. The experimental cell and model were able to obtain complete methane conversion with a >99% recovery of hydrogen [69]. Similar to these studies, this thesis will model protonic ceramic electrochemical reactors that convert methane into carbon dioxide with the production of hydrogen. The model developed in this model will utilize a Ni-CeO_2 anode for the fuel-side reactions, changing the cell kinetics and operating conditions of the cell. The molar concentration of the methane will be much lower than the discussed studies, utilizing unburned methane instead of a consistent, high concentration feed.

Various studies have modeled protonic ceramic electrochemical cells as a combined cycle [74, 76, 83]. Wang et. al. simulated a combined solar power plant and a protonic ceramic electrolysis cell. The solar model consisted of a solar heating unit that feeds the heated liquid into a SCO_2 Brayton cycle. The power generated from the Brayton cycle is fed into a 30,000-cell PCEC unit to generate hydrogen. The PCEC used a multi-physics model that consisted of a BCZY electrolyte, a Ni-BCZY cathode, and a BCZY-SSC anode operating at 650°C. Wang et. al. obtained an overall thermal efficiency of 41.41%, an exergy efficiency of 26.65%, a net power output of 730kW, and a hydrogen production rate of 80.52Nm^3/h [83]. Sasmoko et. al. modeled a methanol-fuel PCFC and gas turbine (GT) combined cycle. The cathode air management system was used for both the cathode of the PCFC and as air for a combustion chamber. The anode stream consists of a steam reformer that feeds a stream consisting of 67% H_2 into the anode, with the exhausted stream from the anode being fed into a combustion chamber. The exhaust from the combustion chamber is used to power a gas turbine. The PCFC was modeled in Thermolib, utilizing a cerium strontium ytterbium oxide (CSYO) electrolyte and platinum electrodes (anode and cathode). The cell was operated at a current density of 800A/m^2 and a temperature range of 1073K-1273K. The proposed PCFC/GT system by Sasmoko et. al. obtained a combined system efficiency of 66.5%. Similar to the model developed by Sasmoko, this thesis will utilize exhausted gases from another system as fuel for the PCEC unit. The primary difference is that this thesis is utilizing a protonic ceramic cell in an electrolyzer configuration as a PCER, while Sasmoko modeled the protonic ceramic cell in a fuel cell configuration [76]. This thesis does not model the power source for the PCER as Wang et. al. had demonstrated, instead focusing on the integration of a PCER into the exhaust stream of an

engine that is fuel by HNG with an integrated hydrogen recirculation system modeled in Aspen HYSYS.

Chapter 3: Methodology

In this section we will be introducing the equipment, theory, and testing procedures for the engine methane mitigation techniques, PCER modeling, and Aspen HYSYS Combined Engine/PCER System. All the equipment utilized in this thesis is sourced from the Renewable Energy and Carbon Management Center at the University of Oklahoma.

3.1: Engine Methane Mitigation Technologies

This section will investigate the theory surrounding how unwanted exhaust emissions are created in a combustion environment. When natural gas is combusted in an engine, hydrocarbon and other harmful emissions are emitted due to a non-stoichiometric combustion condition. For the sake of this analysis, methane will be used because of its high concentration (87-96%) in natural gas [84]. When the engine combustion is balanced stoichiometrically with a theoretical fuel source of methane and an assumption of no dissociation, the exhaust will contain carbon dioxide (CO_2), water (H_2O), and unburned nitrogen (N_2) as shown in Equation 1.

Equation 1: Stoichiometric combustion of methane

$$CH_4 + 2 * (O_2 + 3.76N_2) \rightarrow CO_2 + 2H_2O + 7.52N_2$$

This composition considers the air to be composed of 21% oxygen and 79% nitrogen [85]. When we look at a non-stoichiometric combustion condition, we can have an excess or lack of hydrocarbon fuel, oxygen, nitrogen, and/or other compounds from the air and/and fuel. Methane being present on the product side means that it was not completely combusted, meaning that there was not enough oxygen in the system, the time between the fuel spark and the exhaust port opening was too small, or the flame front was not fast enough to combust all the available fuel. Because the engine is operating in a lean burning condition, the flame front speed and/or the

exhaust port opening too soon are more likely reasons. Carbon dioxide forms from stoichiometric combustion and then there is an excess in air, but carbon monoxide only forms when there is a lack of oxygen as shown in Equation 2 [86].

Equation 2: Half reaction mechanism for the Incomplete combustion of methane

$$2CH_4 + 3O_2 \rightarrow 2CO + 4H_2O$$

Nitrogen oxides, primarily nitrogen monoxide and nitrogen dioxide, are formed when excess air is present in the combustion system. NO_2 is formed from NO and occurs in states of rapid cooling [87]. NO can be formed through thermal, prompt, and fuel sources. Thermal NO is an oxidation reaction from atmospheric nitrogen that is part of the exhaust stream. Prompt NO comes from the reaction of atmospheric nitrogen with hydrocarbon radicals in fuel-rich regions of combustion. Fuel NO comes from the oxidation of nitrogen in the fuel. Because this analysis for chemical kinetics uses methane in a lean-burning condition, we will not be considering fuel NO or prompt NO. Thermal NO stems from the Zeldovich two-strep mechanism shown in Table 1. This mechanism is thermally driven, with the rate constants being exponentially related to the reaction temperature.

Table 1: Zeldovich two-step mechanism for the thermal formation of nitrogen oxide

Mechanism [87]	Rate Constant [88]
$N_2 + O = NO + N$	$k_{thermal,1} = 1.4 \times 10^{14} * e^{(\frac{-37,900}{T})}$
$N + O_2 = NO + O$	$k_{thermal,2} = 6.4 \times 10^{9} * e^{(\frac{-3140}{T})}$

3.1.1: Spark Ignition Timing Modification Theory

The input of fuel and air are both mechanically controlled, with the air intake and exhaust occurring when the piston gets to an opening in the respective engine block sections shown in Figure 1. Because of this design, the ignition timing is the only way to directly modify the firing of the engine.



Figure 1: Combustion Chamber Design with Air intake Cutouts

The spark ignition system utilizes a magnetic strip attached to a rotating flying wheel. When the fly wheel is spinning, the magnetic strip passes a stationary pick-up coil in the shape of a block, initiating the spark system. The spark system utilizes an alternator connected to the pick-up coil, sending a small charge to two ignition coils that initiate the electric spark at two corresponding spark plugs as seen in Figure 2.

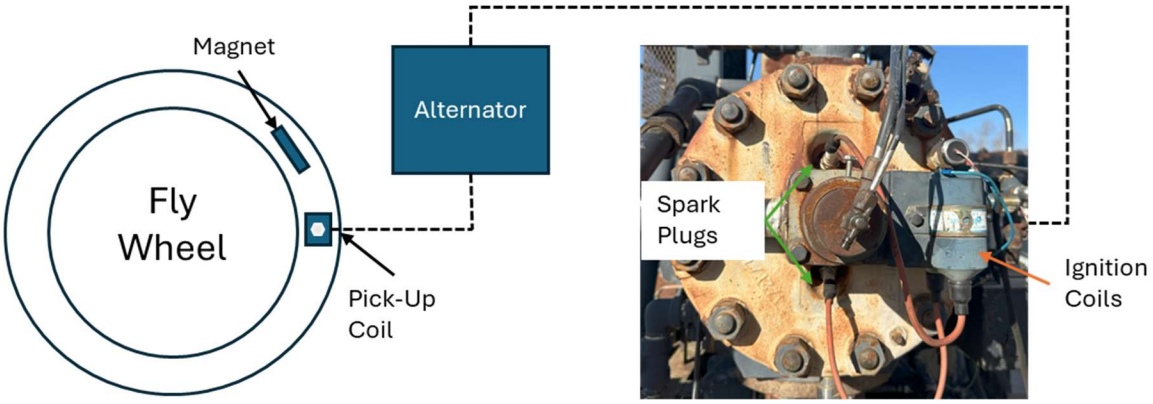

Figure 2: Spark Ignition System for an AJAX DPC-105.

In order to modify the spark timing of the engine, the pick-up coil has been mounted a Z-axis slotted bracket as shown in Figure 3a. When the pick-up coil is moved down, the timing is retarded, and the spark will occur later than originally set. When the pick-up coil is moved up, the timing is advanced, and the spark will occur earlier than originally set. This phenomenon is shown in Figure 3b, with the pick-up coil block movement correlating to a position on the flywheel. The terminology used when describing the timing of the spark event is based on the angle of the crank shaft relative to the piston position in the combustion chamber. When the piston is at the top of the combustion chamber closest to the spark plugs, the piston is at Top Dead Center (TDC). When the piston reaches the lowest point in the combustion chamber furthest from the spark plugs, the piston is at Bottom Dead Center (BDC). This thesis will use the angle before top dead center (ABTDC) as the unit of timing in degrees. The bracket shown in Figure 3a allows for the movement of the pick-up coil up to 9 degrees of retarding the original setting and 5 degrees advancing the original setting. Due to the danger of knocking in the engine, the advancing angles are further limited when compared to retarding angles.

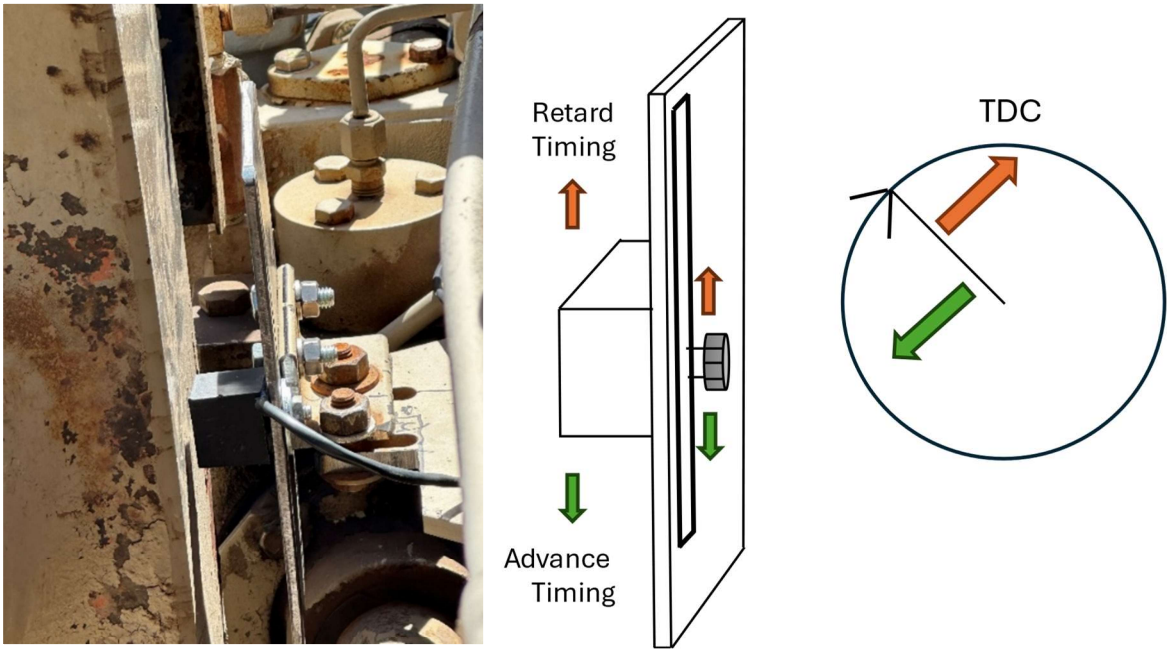

Figure 3: (a) Pick-up Coil Z-axis slotted bracket, (b) Advancing and Retarding Correlation Diagram

3.1.2: Hydrogen Natural Gas Blending Theory

This thesis blends hydrogen into an existing natural gas line that is fed into a mixing tank prior to entering the engine as shown in Figure 4a. The natural gas line is fed into a T-shaped pipe adapter that directs the blended gas into a mixing tank. The blended fuel from the mixing tank is drawn into the engine from the internal pressure of the engine once the pressure reaches high enough to open the fuel port valve. The blending at the T-shaped pipe adapter shown in Figure 4 has a narrow pipe fitted at the bottom entrance that injects hydrogen. The injection pipe is installed slightly above the center line of the T-shaped pipe adapter so as to not restrict the flow of natural gas and to reduce the production of turbulence at the joint.

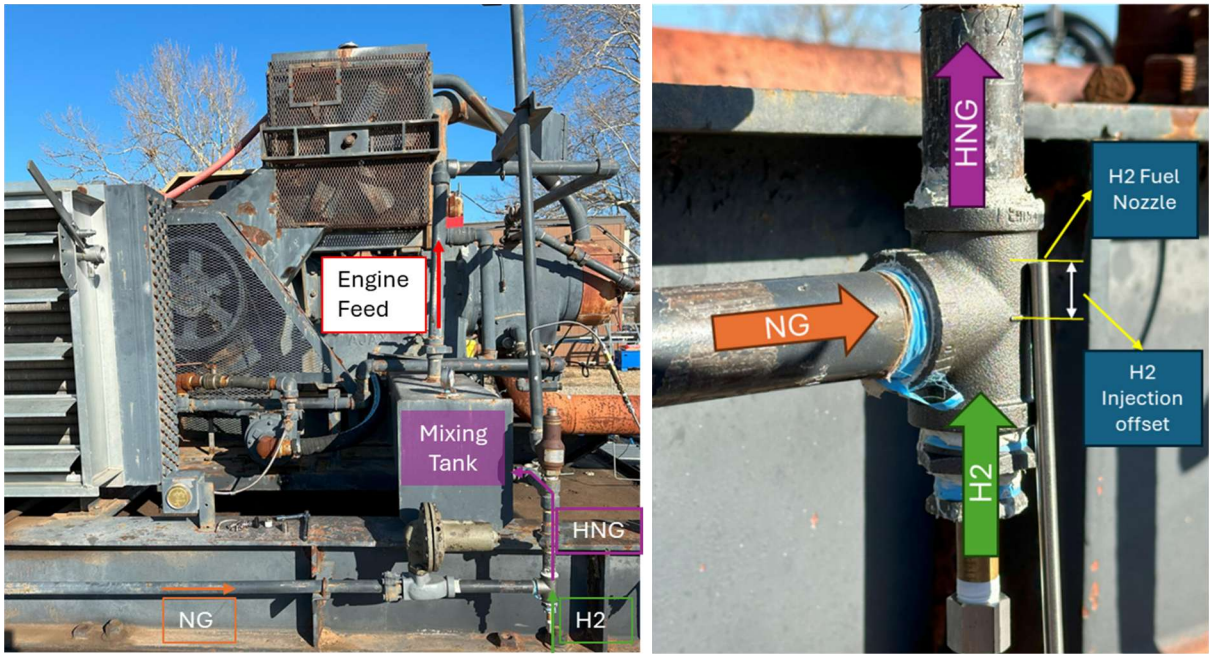

Figure 4: (a) Fuel system blending schematic, (b) Natural gas line modification to include an injection line above the angle change in the t-shaped pipe adapter.

Hydrogen is sourced from a hydrogen tank that is controlled using a pressure regulator. The flow is then modulated with a mechanical directional control flow valve and a mass flow meter to control the hydrogen flow to the mixing tank.

Calculating the hydrogen flow rate is necessary to obtain a specific ratio of natural gas and hydrogen requires knowledge of the temperature, pressure, density, and gas compositions being used within the system. Without a direct measurement system for the composition of natural gas and hydrogen in the mixing tank, Aspen HYSYS was used to simulate the blending phenomenon. The model utilized the mass flow rate and stream temperature from the natural gas flow sensor, the flow regulator pressure from the natural gas line, and the hydrogen tank regulator pressure as the primary input for the model shown in Figure 11.

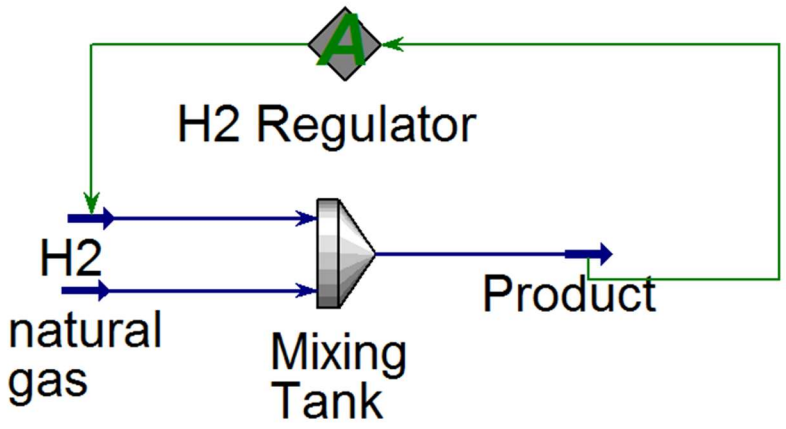

Figure 5: Aspen HYSYS HNG blending model

In order to calculate the target hydrogen content, a simulated regulator was created. The regulator changed the molar flow rate for the hydrogen steam to reach the target hydrogen molar composition in the mixing tank stream, which is called the "product" in Figure 5. The required hydrogen volumetric flow rate, called the "Actual Volume Flow" in the model, is obtains from the "properties" tab within the stream console as shown in Figure 6. The "Actual Volume Flow" from the model takes the operating temperature and pressure into account, providing an accurate density value when calculating volumetric flow.

Stream Name	H2	Vapour Phase
Molecular Weight	2.016	2.016
Molar Density [kgmole/m3]	0.1616	0.1616
Mass Density [kg/m3]	0.3257	0.3257
Act. Volume Flow [ft3/min]	0.8184	0.8184
Mass Enthalpy [kJ/kg]	-250.9	-250.9

Figure 6: Volumetric flow rate property for the hydrogen flow rate obtained after setting the product concentration target.

3.1.3: Spark Ignition and Hydrogen Blending Equipment

Table 2: AJAX DPC-105 engine specifications [89].

Engine Type	AJAX DPC-105
Rated Power (bhp)	105
Rated Speed (rpm)	425
Cylinder Count	1
Stroke	2
Bore x Stroke (in)	12 x 14
Air Intake Mechanism	Naturally aspirated
Swept Volume (in^3)	1583
Ignition Method	Spark ignition
Cooling mechanism	Water-cooled

The engine-based methane reduction strategies utilize an AJAX DPC-105 natural gas compressor shown in Figure 7. The engine is a natural gas-fed, two-stroke, naturally aspirated, and spark-ignition integral compressor as detailed in Table 2. The natural gas engine and compression diagram is shown in Figure 8.



Figure 7: AJAX DPC-105 natural gas-fed, two-stroke compressor

The natural gas engine and compression diagram is shown in Figure 8. The fuel for the engine is drawn directly from the city line and the pressure is controlled by a pressure regulator. The compression side of the engine utilizes a closed circulation system that is controlled through regulators. The natural gas entering the engine is regulated through the suction pressure regulator, and the pressure of the compressed gas coming out of the engine is regulated using a discharge pressure regulator. The compressed natural gas exiting the compressor enters a high-pressure tank that circulates the fuel back to a three-way T-joint pipe adapter that is split between the outlet of the makeup tank and the stream entering the suction pressure regulator. The adapter is used to allow the makeup tank to sustain fuel content in the compression cycle.

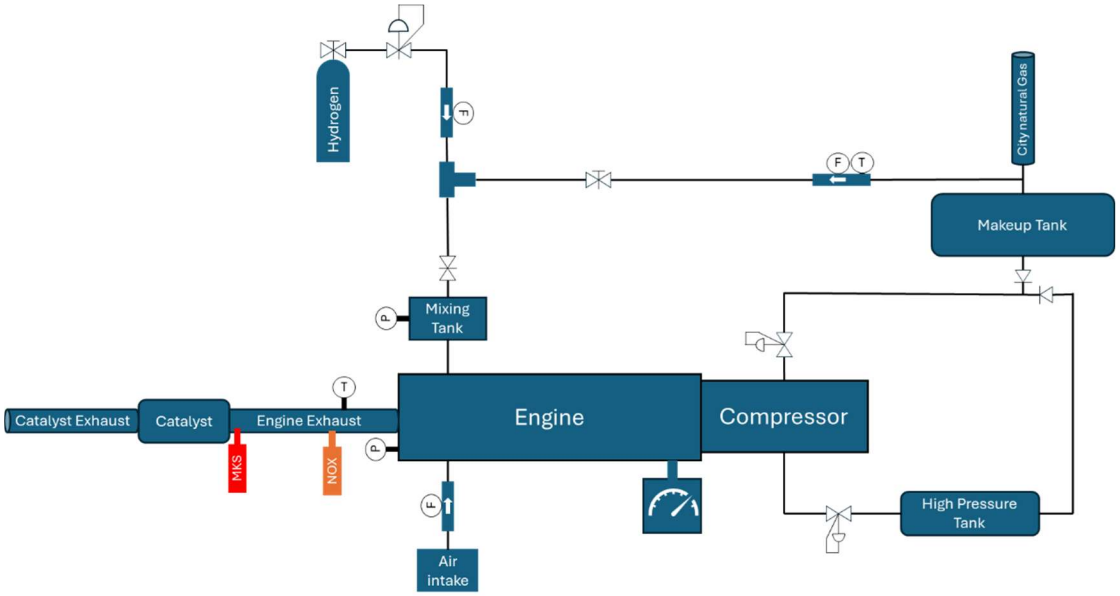

Figure 8: Engine Operation Schematic

Table 3: Equipment utilized in engine testing

Sensor Type	Make	Model
Pressure Transducers	Omega	PX359 [90]
	ChampionX	Windrock 6400 Kit [91]
Pressure Gauge	WIKA	Bourdon Tube Liquid Fill
Flowmeters	Fox Thermal	FT1 [92]
	Emerson	Micro Motion F025S [93]
Temperature	Dwyer Omega	NB1-ICIN-INDUST-TC [94]
Gas Analyzer	MKS	MultiGas 2030 FTIR [95]
	ECM	NOxCANt NO_x/O_2 Module [96]
Engine Speed (RPM)	ChampionX	Windrock 6400 Kit [91]

		Magnetic Pickup
Dial Caliper	n/a	n/a

The calculation for the engine load was conducted utilizing the AJAX Powerflow compressor simulation. The simulation software allows for the calculation of the engine horsepower (HP) with the input of the suction pressure, discharge pressure, and engine RPM. The engine load is calculated by dividing the engine load from Powerflow by the theoretical maximum HP from the system shown in Equation 3.

Equation 3: Load percentage calculation

$$Load\ \% = \frac{HP_{operational}}{HP_{max}}$$

The engine RPM fluctuates as a load is placed on the compressor side when first turning the engine on, with the added pressure on the compressor side actively resisting the engine side. Once the system reaches equilibrium, a slight fluctuation will occur between the suction pressure and the RPM of the engine. Due to this fluctuation, the actual load calculation in Powerflow is made using the average suction pressure, discharge pressure, and engine RPM for verification.

In order to obtain engine operational data, the system is equipped with flow meters, pressure sensors, and temperature sensors detailed in Table 3. To obtain data about engine modifications, an ECM NOxCANt kit NO_x/O_2 amperometric sensor, an MKS 2030 infrared Fourier Transform Infrared Spectroscopy (FTIR) gas analyzer, a dial caliper, and a Windrock 6400 portable engine analyzer kit were used. An Emerson Coriolis flow meter was used to measure the mass flow rate and stream temperature of the natural gas feed shown in Figure 9a. A Fox Thermal flow meter shown in Figure 9b was used to measure the volumetric flow for the

hydrogen inlet feed and the air intake. The flow meter is a thermal mass flow meter that utilizes inlet pressure and temperature to calculate the respective volumetric flow rates.



Figure 9: Flow meters used in experimentation, (a) Emerson flow meter for natural gas stream, (b) Fox Thermal flow meter for air and/or hydrogen data collection.

The collection of pressure data was obtained by either visual or data-collection methods. The mixing tank and fill tank pressures are obtained using a pressure gauge and visual inspection. The hydrogen feed line pressure was set using a pressure regulator, with the pressure data being obtained through visual inspection.

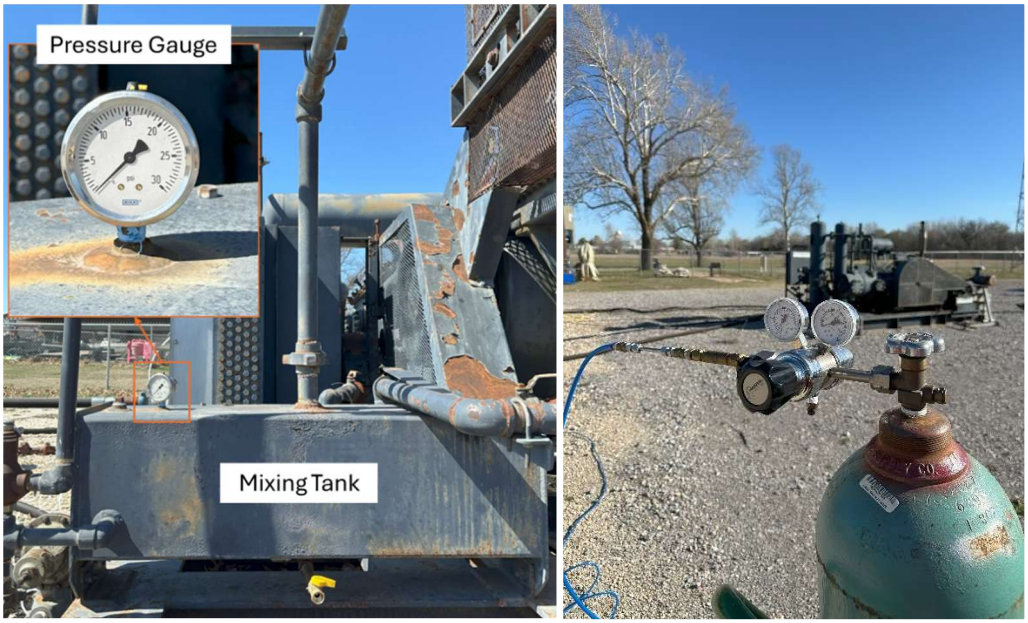

Figure 10: (left) Mixing tank pressure gauge, (right) hydrogen tank pressure regulator

The suction and discharge pressures are collected using an omega PX359 pressure transducer shown in Figure 10. The pressure transducers transfer data digitally, allowing for direct collection and monitoring of the engine. The engine cycle pressure from the combustion chamber is obtained using the Windrock 6400 combustion analyzer connected to a high-temperature and high-pressure-rated pressure transducer shown in Figure 11.

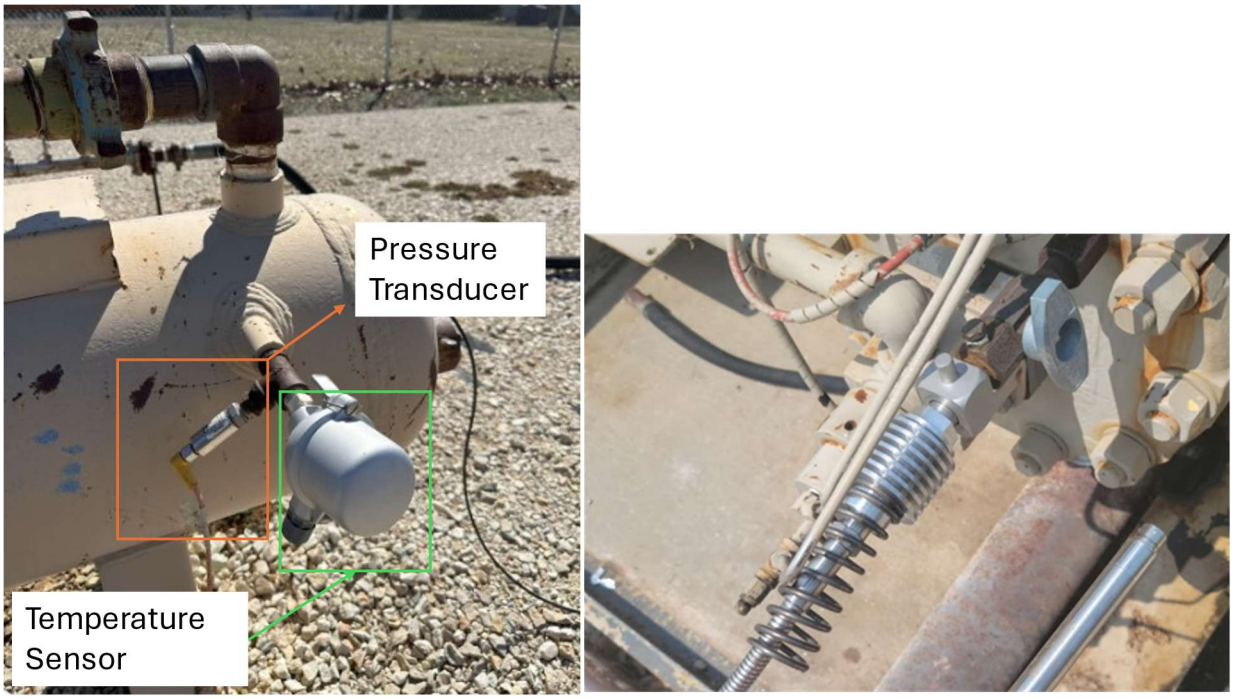

Figure 11: (a) Omega pressure transducer and temperature sensor, (b) Windrock 6400 pressure transducer attachment

All temperature data was collected with Dwyer Omega Protection headed J-Type thermocouples shown in Figure 11. The speed of the engine was obtained through both a Windrock Encoder that connects to the Windrock 6400 and a mounted magnetic pickup on the flywheel cage shown in Figure 12.



Figure 12: (a, left) Permanent Magnetic RPM Encoder, (b, right) Windrock Magnetic Encoder

The emissions data is obtained using an MKS FTIR gas analyzer and a NO_x/O_2 amperometric sensor. The MKS analyzer utilizes a probe connected to the exhaust pipe of the engine before the emissions reach the catalyst. The primary gas data collected from the MKS analyzer includes CO, CO_2, NO, NO_2, H_2O, and CH_4. The gases are transferred in a heated pipe by way of a pump before entering the gas analyzer stored within the lab building shown in Figure 13. The MKS analyzer utilizes liquid nitrogen for cell cooling and a nitrogen gas stream to purge any air from the lines. The ECM NOxCANt kit includes both a NO_x/O_2 amperometric sensor and a digital interface to collect data as shown in Figure 14. The amperometric sensor is used to collect immediate data regarding combined nitrogen oxides (NO_x) and oxygen (O_2) content in the exhaust stream. The NO_x/O_2 sensor allows for the collection of oxygen values that the MKS does not contain, along with an additional source of combined NO and NO_2 data in the form of NO_x.

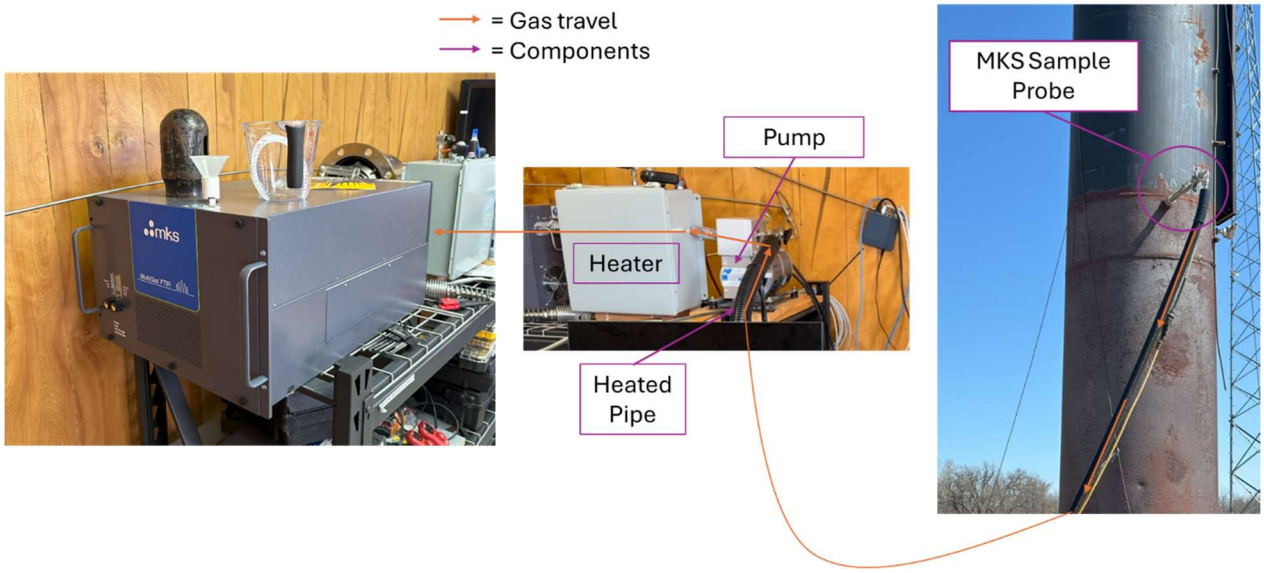

Figure 13: MKS analyzer gas stream and equipment

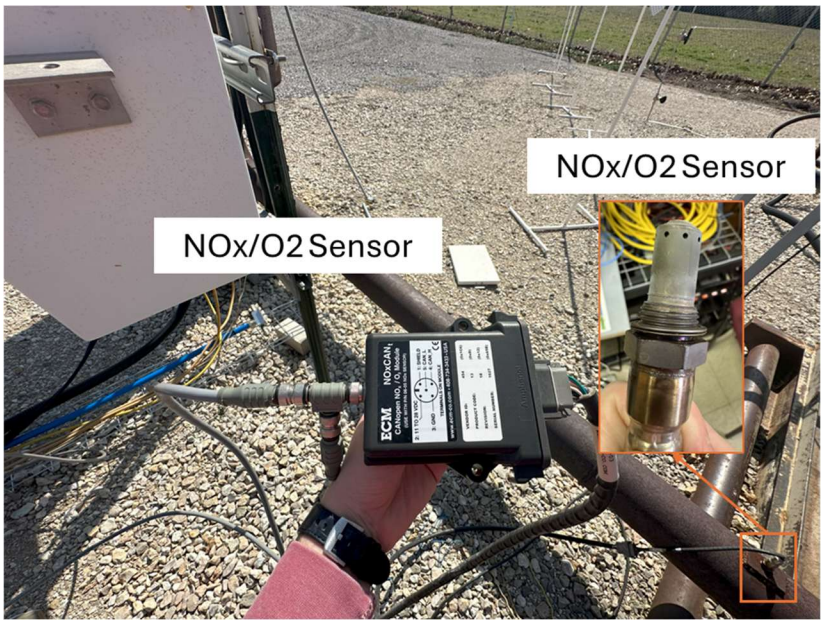

Figure 14: NOxCANt amperometric NO_x/O_2 sensor kit to measure oxygen and nitrogen oxides in the engine exhaust stream

3.1.4: Spark Ignition and Hydrogen Blending Testing Procedures

The spark timing and hydrogen blending will be tested together. The ignition timing baseline is set to 11° BTDC, with all experimentation operating the engine at 60% a load condition with no modification to the air intake system. The spark timing will advance to 12° BTDC in increments of 0.5° and advanced to 9° BTDC in increments of 1°. At each angle, the hydrogen to natural gas concentrations will be modified in the range of 0-20 mole percentage (mol %) H_2 in increments of 10% H_2. The resulting testing conditions can be found in Table 4.

Table 4: Test parameters for the methane reduction using combined spark ignition timing and blended HNG

Angles off Baseline angle	Actual Spark Timing Angle	Inches off 0 for magnet	Hydrogen Mole Fraction (%)	# Tests
-1	12 BTDC	0.47124	0%, 10%, 20%	3
-0.5	11.5 BTDC	0.23562	0%, 10%, 20%	3
0	11 BTDC	0	0%, 10%, 20%	3
1	10 BTDC	0.47124	0%, 10%, 20%	3
2	9 BTDC	0.94248	0%, 10%, 20%	3

All of the emissions data will be converted to a dry basis and an oxygen content of 15% oxygen shown in equations Equation 4 and Equation 5 respectively. In Equation 4 PPM_{wet} represents the gas ppm with water in the line and H_2O % represents the water content in the gas stream. In Equation 5 PPM_{dry} represents the gas stream content if no water was in the line obtained from Equation 4 and O_2% is the oxygen content percentage. This modification to the data allows for a

fair comparison between each run, with fluctuations in the oxygen content and water content impacting the comparability of each run [97].

Equation 4: Dry basis emission conversion [97]

$$PPM_{dry} = \frac{PPM_{wet}}{(1 - H_2O\ \% * 0.001)}$$

Equation 5: 15% O2 conversion from operational oxygen content [97]

$$PPM_{15\%O_2} = \frac{(20.9 - 15)}{(20.9 - \ O_2\%)} * PPM_{dry}$$

The oxygen data is averaged per timing and hydrogen blend setting to obtain a more accurate O_2% reacting from the amperometric NO_x/O_2 sensor.

3.1.5: Spark Ignition and Hydrogen Blending Validation Theory and Procedure

The replicability of the experimental data for the spark timing modification and hydrogen blending will be validated by taking the same operational conditions and equipment but operating the engine at a load of 55%. The impact that the blending and timing modifications have on the engine performance will be validated by analyzing the thermal efficiency of each angle and fuel composition for both 60% and 55% engine loads. The indicated thermal efficiency, η_{ITE}, relates the observed engine operational conditions to the amount of energy provided to the engine in the form of fuel and was introduced by Nguyen [97]. The equation for indicated thermal efficiency, η_{ITE}, is a ratio of the speed in revolution per minute (RPM), swept volume that the piston travels, V_{swept}, and the indicated mean effective pressure (IMEP) to the product of the fuel flow rate entering the engine and the caloric energy that the fuel provides in the form of the heating value (HV) shown in Equation 6.

Equation 6: Indicated thermal efficiency equation [97]

$$\eta_{ITE} = \frac{IMEP * V_{swept} * RPM}{\dot{m}_{fuel} * HV}$$

The IMEP is the average pressure across a piston cycle. This is calculated by first obtaining data from the Windrock pressure sensor, which provides a pressure value at each of the 360-degree crank angles for 251 cycles. The difference in pressure for each section in the combustion chamber is collected and averaged. This value is then divided by the full volume swept shown in Equation 7, which is the volume that the piston traveled to top dead center and bottom dead center twice.

Equation 7: Indicated mean effective pressure equation [97]

$$IMEP = \frac{\sum(P_i - P_{i-1}) * dV}{2 * V_{swept}}$$

The values for the RPM, mass flow rates, pressures, and heating values change for every test due to outdoor temperature and engine conditions, so the input values will be provided in the results section.

3.2: PCER Methane Conversion Modeling

Protonic ceramic electrochemical reactors allow for the conversion of exhaust methane emissions from an engine. The cell is in a tubular configuration where the engine exhaust enters an internal tube coated with catalyst materials on the walls of the tube. An outer tube is mounted around the catalyst-coated tube to capture and transport the produced hydrogen from the cell. All unreacted chemical compounds and products of the hydrogen production process exit from the small tube as shown in Figure 15. This thesis will utilize a PCER constructed with a nickel-

supported Cerium Oxide (Ni/CeO_2) anode, a nickel-supported barium zirconium yttrium cerate (Ni/BCZY) electrolyte, and a Ni/BZCY cathode. Ni/BCZY is a common material for PCER electrolytes, anodes, and cathodes, so this will act as a method of validation for the cell operation. The novel component of the model lies with the use of Ni/CeO_2 for the anode, which has been theorized as reducing the required operational temperature of the cell while sustaining a high rate of methane decomposition [98, 99].

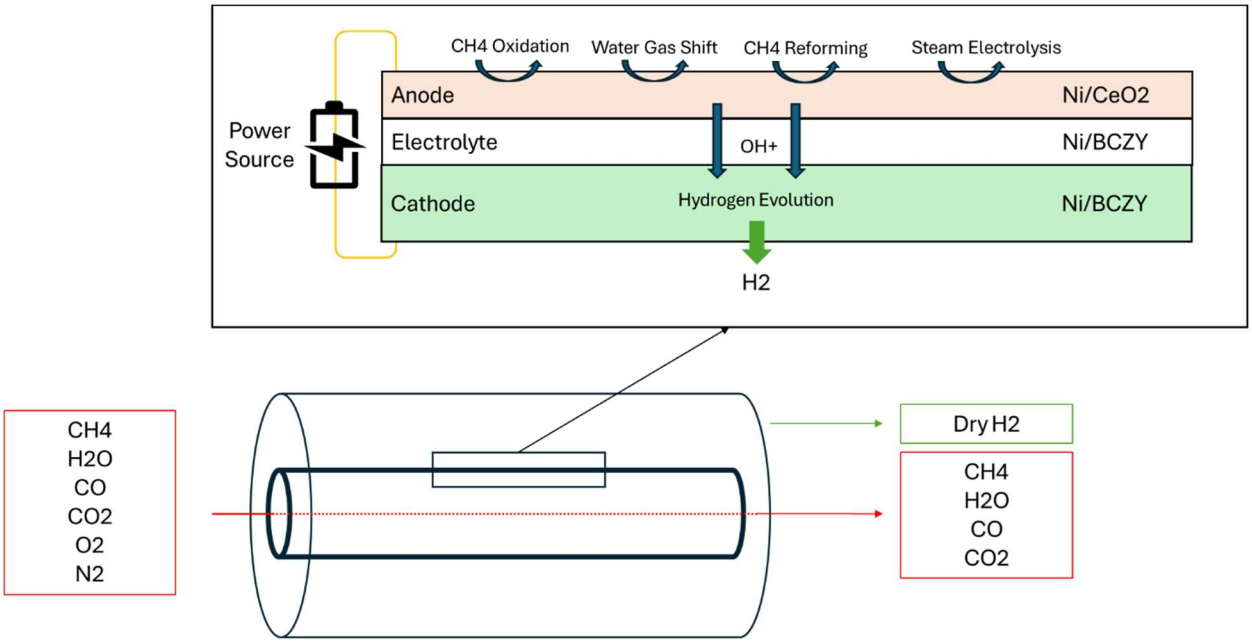

Figure 15: PCER model operational and structural diagram

In this section we will be exploring the development and theory behind a PCER mathematical model equipped with reaction, molar balance, and electrochemical sub models.

3.2.1: PCER Theory

The methane to CO_2 Protonic ceramic electrochemical reactor anode conducts methane oxidation, steam methane reforming, and water gas shift reactions while the cathode conducts the hydrogen evolution reaction. These reactions are summarized in Table 5.

Table 5: Chemical reactions used in PCER modeling

Reaction	Stoichiometry		Enthalpy (kJ/ml)
Methane Oxidation [100], [101]	$CH_4 + 2O_2 \rightarrow CO_2 + 2H_2O$		-802.7
Steam Methane Reforming [102], [103]	$CH_4 + H_2O \rightarrow CO + 3H_2$		+206
Water Gas Shift [102], [104], [105], [106]	$CO + H_2O \rightarrow CO_2 + H_2$		-41.9
Hydrogen Electrolysis	Steam Electrolysis[107], [108]	$H_2O \rightarrow \frac{1}{2}O_2 + 2H^+ + e^-$	n/a
	Hydrogen Evolution [70]	$2H^+ + e^- \rightarrow H_2$	n/a

Methane oxidation (MO) in this thesis is defined as the use of a catalyst to break the C-H bond in the methane and oxidize the respective carbon and hydrogen elements [109]. This allows the formation of carbon dioxide and dihydrogen monoxide, as shown in Equation 8.

Equation 8: methane oxidation reaction stoichiometry

$$CH_4 + 2O_2 \rightarrow CO_2 + 2H_2O \text{ [1]}$$

Methane is considered a very stable compound, requiring a high activation energy to break the present carbon-hydrogen bond. This is also due to the ethane intermediate reactions from CH_4 to CO, with water interactions after each half-cell reactions allowing for the decomposition of CH_3OH to HCHO and finally to CO [110]. Due to this high activation energy, the catalyst must operate at a higher temperature to sustain high rates of conversion [100]. Steam Methane Reforming (SMR) shown in Equation 9 is defined as an endothermic process that uses water vapor to break the C-H bond in CH_4.

Equation 9: Steam Methane Reforming Stoichiometry

$$CH_4 + H_2O \rightarrow CO + 3H_2$$

The catalyst in the SMR process holds the broken carbon molecule through adsorption on the catalyst surface before the gaseous water interacts with the adsorbed carbon molecule to form CO shown in Equation 10 [111].

Equation 10: Partial reaction for steam methane reforming over a metal catalyst [111]

$$CH_4 \rightarrow C(ads) + 2H_2$$

$$C(ads) + H_2O \rightarrow CO + H_2$$

The steam methane reaction is difficult to start because the C-H bond is so stable, requiring a high temperature, pressure, and catalytic activity. The environmental conditions of the PCER

unit can be reduced with more effective catalytic material in the anode. The final reaction for the anode is the Water Gas Shift reaction (WGS) shown in Equation 11. This thesis will use the associative mechanism, also called the Langmuir-Hinshelwood mechanism, for WGS because of the lower operating temperature of the PCER cell. The associate mechanism postulates that the CO and H_2O adsorb onto the catalyst surface, decomposing on the surface to form CO_2 and H_2 [112].

Equation 11: Water Gas Shift reaction stoichiometry

$$CO + H_2O \rightarrow CO_2 + H_2$$

The water gas shift mechanism is vital in the conversion of carbon monoxide to carbon dioxide, with the carbon dioxide being the goal for the PCER exhaust stream. For this thesis, the cathode side will only contain the Hydrogen Evolution Reaction (HER). Hydrogen evolution is an electron-driven mechanism that combines the input power to the cell and the diffused hydrogen to form dry, gaseous hydrogen shown in Equation 12.

Equation 12: Hydrogen Evolution Reaction stoichiometry

$$2H^+ + e^- \rightarrow H_2$$

Hydrogen evolution is an electrochemical process, so the reaction is estimated based on the electrochemical model discussed in section 3.2.2: PCER Modeling Framework instead of being calculated through traditional kinetic equations.

3.2.2: PCER Modeling Framework

The PCER model relies on the modeling framework constructed by Norman et. al., with the mole balance, energy balance, and electrochemical model being the same [78]. The adopted model operates using engineering equation solver (EES) and is modified to include a real-world

exhaust emission composition, varied geometry, different reaction kinetics, and varied diffusion mechanisms. The most significant modification to the model was made in the kinetics sub model and cell geometry, with Norman et. al. utilizing a Mo-ZSM-5 electrolyte and a variety of other materials to source anode and cathode material characteristics, while this thesis will focus on the specific material properties of Ni/BCZY and Ni/CeO_2. Deviation from these materials will be specified, with an experimental version of the modeled cell not in production as of the completion of this thesis

The model is a steady-state, isothermal, 2-D model that is discretized along the length of the cell and at different segments of the cell construction shown in Figure 16. The cell is discretized into 6 partitions, with partition 1 being the fuel entry tube, partition 2-4 being the PEM structure (anode | electrolyte | cathode), partition 5 being the hydrogen transportation tube, and partition 6 being the outer containment tube.

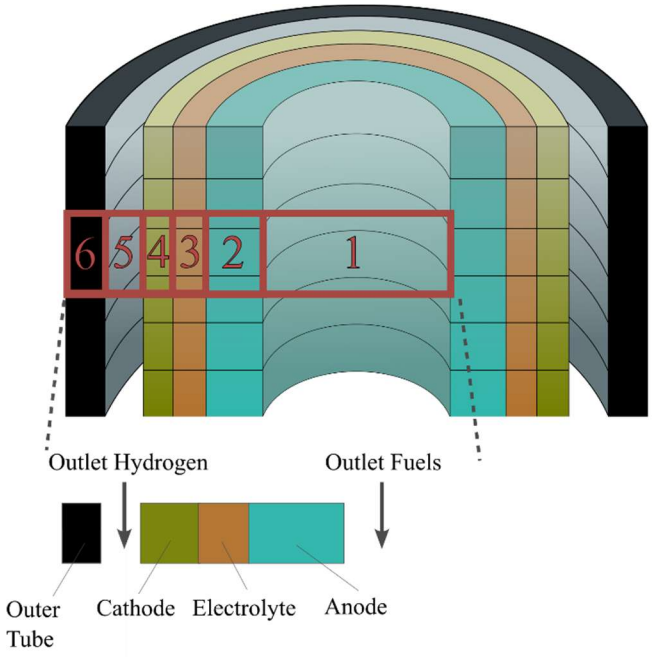

Figure 16: The geometry of the PCER model

The cell is considered symmetric for all layers of the PCER model. The active area of the cell layers is calculated using the average radius of the fuel delivery tube-anode interface and the air delivery tube-cathode interface shown in Equation 13. This equation is utilized in calculating the gas species concentration and utilized throughout the electrochemical sub model. The active area takes the average radius of the fuel delivery tube and the area up to the cathode-air tube interface.

Equation 13: Cell active area equation

$$A = 2 * \pi * \frac{r_4 + r_1}{2} * L_{cell}$$

The anode area is another geometrically significant calculation, being used in calculating the flow rate for the model and the interconnect area. The anode area is calculated using the specific area of an open tube shown in , with t_{an} being the anode thickness and L_{cell} being the cell length.

Equation 14: Surface area of the anode equation

$$A_{anode} = 2 * \pi * t_{an} * L_{cell}$$

The interconnect design utilized by Norman et. al. is adopted into this PCER model. Norman et. al. considered the interconnect to be a rectangular shape along the walls of the inlet tube. This thesis utilizes a tubular PCER without a dedicated feed tube and fuel flow channel, instead using the feed tube walls as the electrode structure itself. Although the method for fuel interaction with the catalyst membrane is different, the same general interconnect area equation is used by Norman in Equation 15 [78].

Equation 15: Interconnect area

$$A_{IC} = 2 * \pi * \left(\frac{r_{average}}{4}\right) * r_{FDT}$$

$$r_{average} = \frac{r[1] + r[4]}{2}$$

The flow rate for the fuel utilizes the Gas Hourly Space Velocity (GHSV) when describing the flow rate in relation to flow over a catalyst. Bobrova provides a specific surface area (SSA) value of 82 m^2/mg for Ni/CeO2 with a nickel loading of 5% [113]. The model that Norman developed uses mass flow in units of Kg/s, so the anode surface area, A_{anode}, was used to convert the specific surface area to grams as shown in Equation 16. The equation requires the conversion of SSA from grams to kilograms and the GHSV needs to be converted to seconds.

Equation 16: Fuel flowrate across the anode in units of mass flow (kg/s)

$$\dot{m} = \left(\frac{1}{SSA * 1000}\right) * \left(\frac{GHSV}{3600}\right) * A_{anode}$$

The final variable that we will discuss is the catalyst mass. Some reaction rates are provided in units of mols per catalyst grams per second (mol/gcat*s), so the mass of the catalyst must be calculated. Using Equation 17, the mass of the anode catalyst can be obtained. The density of a catalyst material, calculated in Equation 19, must be converted from particle density to the bulk density to account for the porosity of the material [114].

Equation 17: Mass of catalyst calculation

$$m_{cat,ni} = \rho_{bulk} * V_{anode}$$

Equation 18: Volume of the anode

$$V_{anode} = \pi * L_{cell} * ({r_3}^2 - {r_2}^2)$$

Equation 19: Conversion of particle density to bulk density

$$\rho_{bulk} = (1 - \phi) * \rho_{particle}$$

3.2.2.1: Mole Balance Model

The mole balance model is built on the reactions occurring on the anode and cathode surfaces. The molar flow of each inlet compound is balanced for the water gas shift (WGS), steam methane reforming (SMR), methane oxidation (MO), and hydrogen evolution reaction (HER). The molar flow for each compound, N_c, is derived by first obtaining the inlet molar concentrations and then finding the molar concentration along the cell. Because the mole balance model is considered to be steady state, the molar flow is the number of moles for each compound. The inlet molar flow for each compound, $N_{c,o}$, is found by multiplying the total inlet mass flow rate, $\dot{m}_{fuel/air}$, to the mole fraction, X_c, and dividing that product by the molar mass of the compound, MM_c, shown in Equation 20.

Equation 20: inlet molar flow per compound

$$N_{c,o} = \frac{X_c * \dot{m}_{fuel/air}}{MM_c}$$

We then derive the molar concentration for each compound across the cell, $N_{c,i}$, by dividing the mass of each compound by the molar mass for the respective compound shown in Equation 21.

Equation 21: Moles for each compound across the cell

$$N_{c,i} = \frac{m_c}{MM_c}$$

The mole count, N, is the variable used when balancing the reactants and products from each reaction. The reactions occurring in the cell are the driving variables for changing the fuel concentrations along the cell. Because of this, the reactions are in the unit of moles as well due to the steady state nature of the model. The mole balance model calculates the current mole count of a given compound by subtracting the precious mole count for those compounds and then

either adding or subtracting the mole count that is being produced or utilized in the reaction kinetics sub model. In order to simulate the diffusion of hydrogen to the air side, a diffusion coefficient is added called $r_{diff}[i]$. The diffusion of hydrogen is important because fuel accumulation in the fuel channel would cause any reaction that creates hydrogen to run in reverse due to a high hydrogen concentration. Adding in the diffusion of the hydrogen allows for more accurate reaction kinetics to take place along the length of the cell.

$$0 = N_{CH_4}[i-1] - N_{CH_4}[i] - r_{sr}[i] - r_{mo}[i]$$

$$0 = N_{CO}[i-1] - N_{CO}[i] - r_{wgs}[i] + r_{sr}[i]$$

$$0 = N_{H_2}[i-1] - N_{H_2}[i] + r_{wgs}[i] + 3 * r_{sr}[i] + 2 * r_{her}[i] - r_{diff}[i]$$

$$0 = N_{CO_2}[i-1] - N_{CO_2}[i] + r_{wgs}[i] + r_{mo}[i]$$

$$0 = N_{H_2O}[i-1] - N_{H_2O}[i] - r_{wgs}[i] - r_{sr}[i] + 2 * r_{mo}[i] - 2 * r_{her}[i]$$

$$0 = N_{N_2F}[i-1] - N_{H_2F}[i]$$

$$0 = N_{O_2F}[i-1] - N_{O_2F}[i] - 2 * r_{mo}[i] - r_{her}[i]$$

$$0 = N_{H_2A}[i-1] - N_{H_2A}[i] + r_{diff}[i]$$

$$r_{diff}[i] = 0.8 * (r_{wgs}[i] + 3 * r_{sr}[i] + 2 * r_{her}[i])$$

Other important variables that are calculated within the mole balance model are the partial pressure and compound concentrations, which are used in the reaction kinetics and useful to know for the model user. The concentration for each compound is derived by looking at the current mole count, $N_{c,i}$, at the specific location along the cell and dividing it by the cell volume, at that segment shown in Equation 22. The volume is the product of the active area, A_{active}, by

the channel height, $h_{air/fuel}$, of either the fuel or air, depending on the compound that is being solved.

Equation 22: Concentration along the cell length for each compound

$$C_{c,i} = \frac{N_{c,i}}{A_{active} * h_{air/fuel}}$$

The partial pressure is dependent on the change in the mole fraction of each compound as the reactions either produce or utilize specific compounds. The total mole count for the air and fuel must first be calculated so that the mole count of each individual compound, $N_{c,i}$, can be divided by the total fuel or air value, $N_{air\ or\ fuel,i}$, to obtain the mole fraction at that point along the length of the cell, $X_{c,i}$, shown in Equation 23.

Equation 23: Mole fraction for a specific compound

$$X_{c,i} = \frac{N_{c,i}}{N_{air\ or\ fuel,i}}$$

The partial pressure can now be obtained for the respective compound, $P_{c,i}$, by multiplying the mole fraction for the respective compound by the total pressure at the specific tube length, $P_{tot,i}$, shown in Equation 24.

Equation 24: Partial Pressure for a specific compound

$$P_{c,i} = P_{tot,i} * X_{c,i}$$

3.2.2.2: Reaction Kinetics Sub Model

Reaction rates require some balance between the equation reaction constant and either the partial pressure or concentration. The partial pressure and concentration are obtained using the mole balance, while the specific reaction constants and reaction rate equations must be obtained

theoretically and verified experimentally. The reaction rate equations depend on the order of the equation, with a zero-order reaction equation only requiring the reaction constant and a first-order rate equation being the product of the reaction rate constant and either the concentration or the partial pressure. Higher-order reaction rate equations become more complicated, but for elementary reactions, the power law equation can be used shown in Equation 25. The rate equation diverges from the rate equation when working with non-elementary reactions, requiring density functional theory modeling and experimental validation [115]. Because this PCER model consists of only non-elementary, higher-order chemical reactions, the reaction rate equations were obtained through various studies.

Equation 25: Power Law elementary rate equation [115]

$$-r_a = k_a C_a^{\alpha} C_b^{\beta}$$

The reaction constant, k, determines the rate and direction of a reaction, with the units changing for every reaction order. The reaction constant can be found using the Arrhenius equation, which correlates the activation energy, E_a, and the operating temperature shown in Equation 26. An Arrhenius plot allows for the graphing of the temperature on the x-axis and the experimentally obtained reaction constant on the y-axis to obtain the activation energy and the pre-exponential factor, A. All of the reaction constants obtained from various studies presented the data in either an Arrhenius plot or in tabular form with the activation energy and pre-exponential factor directly presented.

Equation 26: Arrhenius Equation [107]

$$k = Ae^{\frac{-E_a}{R*T}}$$

The PCER sub model used in this thesis utilizes the water gas shift, steam methane reforming, methane oxidation, and the hydrogen evolution reaction as the reaction basis. The model is built on partial pressure, molar concentration, change in Gibbs, and the reaction constants that are sourced from external papers. EES can obtain Gibbs free energy, G, of any compound with an input of temperature and pressure using a built-in library of data. The obtained G values are then organized in the same balance as the stoichiometry to find the Delta Gibbs, ΔG_r, for the respective reaction to indicate the reaction direction shown in Table 6.

Table 6: Delta Gibbs Free Energy equations for each reaction

Variable	Delta Gibbs Balance
Methane Oxidation, ΔG_{mo}	$g_{CO_2} + 2 * g_{H_2O} - g_{CH_4} - 0.5 * g_{O_2F}$
Steam Reforming, ΔG_{SR}	$g_{CO} + 3 * g_{H_2} - g_{CH_4} - g_{H_2O}$
Water Gas Shift, ΔG_{wgs}	$g_{H_2} + g_{CO_2} - g_{CO} - g_{H_2O}$
Hydrogen Evolution, ΔG_{HER}	$g_{O_2} + g_{H_2} - g_{H_2O}$

The equilibrium reaction constant for each reaction can now be obtained by dividing the ΔG_r by the ideal ga constant, R, and the temperature of the PEN (Positive, Electrolyte, Negative) structure, T_{PEN}, and then raising that product to find the exponential value shown in.

Equation 27: Equilibrium reaction constant for a reaction used in the model

$$KQ_r = e^{\frac{\Delta G_r}{R * T_{PEN}}}$$

The reaction constants and rate equations are less intuitive to obtain because they can only be obtained and validated experimentally. The water gas shift reaction (WGS) and the methane steam reforming (SR) reaction utilize reaction kinetics obtained by Palma et. al. when

they studied the impact that Adding CeO_2 has to an Al_2O_3-based methane reformer. The study utilized a wash coat slurry reactor and real-world kinetic data to calibrate a kinetic model for SMR and WGS. The CeO_2-Al_2O_3 catalyst has 5% nickel within the CeO2 catalyst when obtaining the reaction constant [116]. The methane oxidation reaction rate equation and rate constants are obtained from Chen et. al. where they studied the accuracy of different kinetic models that predict methane oxidation. The study utilized a packed-bed reactor containing a 2% nickel supported CeO_2 catalyst operating at temperatures between 360-460℃. This study will use the second-order reduced Mars-van Krevelen, MvK II reduced, rate equation and the supporting reaction constants that Chen et. al. found to be the most accurate for methane oxidation using a Ni/CeO_2 catalyst [117]. The methane oxidation rate equation by Chen et. al. utilized the units of millimoles per gram of nickel catalyst, so equations Equation 17 was used to convert the reaction rate to mmol/s before being multiplied by 1000 to get mol/s. Furthermore, the equilibrium constant of water for methane oxidation is unitless, so it is multiplied by the inverse of the system pressure. The hydrogen evolution reaction is based entirely on the current density of the cell and the electron count, n, which is set as a standard value of 4 electrons. All the reaction rate equations used in the model have been summarized in Table 8.

Table 7: Summary of the reaction kinetics data utilized in the model

Stoichiometry	Reaction Constant Equation
$CO + H_2O \rightarrow CO_2 + H_2$ [116]	$K_{EQ,SR} = 10267 * 10^{10} * e^{(B)}$ $B = -0.125z^4 + 0.3665z^3 + 0.5810z^2 - 27.134z + 3.2770$
	$k_{SR} = \frac{856 * m_{cat}}{60} * \frac{1}{1.027 * 10^{10}} * e^{\left(\frac{-71000}{R*T_{PEN}}\right)}$
	$K_{EQ,WGS} = e^{(-0.2935*z^3+0.6351*z^2+4.1788*z+0.3169)}$

$CH_4 + H_2O \rightarrow CO + 3H_2$ [116]	$k_{WGS} = 11190 * \left(\frac{g_{cat}}{60}\right) * e^{\left(\frac{-33000}{R*T_{PEN}}\right)}$
$CH_4 + 2O_2 \rightarrow CO_2 + 2H_2O$ [117]	$k_{MO,CH_4} = e^{\left(-10.63 * \left(\frac{1000}{T_PEN}\right) + 57.95\right)} * \left(\frac{g_{cat}}{1000 * 133.32}\right)$
	$k_{MO,O_2} = e^{\left(-4.41 * \left(\frac{1000}{T_PEN}\right) + 51.58\right)} * \left(\frac{g_{cat}}{1000 * 133.32}\right)$
	$k_{MO,H_2O} = e^{\left(\frac{331.1}{R}\right)} * e^{-\left(\frac{-202000}{R*T_{PEN}}\right)} * \frac{1}{P}$

Table 8: Reaction rate equations utilized in the model

Reaction Type	Reaction Rate Equations
WGS, [116]	$r_{WGS,i} = k_{WGS,i} * \left(P_{CO,i} * P_{H_2O,i} - \frac{1}{KQ_{WGS,i}} * P_{CO_2,i} * P_{H_2,i}\right)$
SR, [116]	$r_{SR,i} = k_{SR,i} * \left(P_{CO,i} * {P_{H_2,i}}^3 - \frac{1}{KQ_{SR,i}} * P_{CH_4,i} * P_{H_2O,i}\right)$
MO, [117]	$r_{MO,i} = \frac{k_{O_2,i} * {p_{O_2,i}}^{0.5} * k_{CH_4,i} * p_{CH_4,i}}{k_{O_2,i} * {p_{O_2,i}}^{0.5} * (1 + K_{H_2O,i} * p_{H_2O,i}) + k_{CH_4,i} * p_{CH_4,i}}$
HER	$r_{HER} = \frac{i_{cell}}{n_{HER} * F}$

3.2.2.3: Electrochemical Sub Model

The electrochemical model for a protonic ceramic electrochemical reactor is developed in this thesis using the same framework as Norman, with modifications made to the constants utilized [78]. The Nernst equation represented the ideal, open-current voltage that the cell

operates at. The Nernst equation for a protonic ceramic electrochemical cell in an electrolyzer configuration is shown in Equation 28.

Equation 28: Nernst Equation for an electrolyzer[78], [118]

$$E_{Nernst} = \left(\frac{\Delta G_{HER}}{(n_{he} * F)}\right) + \left(\left(\frac{R * T_{pen}}{(n_{her} * F)}\right) * \ln\left(\frac{P_{H_2O}}{P_{h_2} * P_{O_2}}\right)\right)$$

The operating current for the cell is a controlled variable in the model and is modified by changing the current density as shown in Equation 29. The active area, $A_{active,increment}$, uses an incremental length split up by the number of increments along the cell as shown in Equation 30. Splitting up the cell length into multiple parts allows for the HER reaction rate to correlate to each step within the cell and not the total length within the first iteration of the model.

Equation 29: Operating current density

$$i_{cell} = \frac{j_{cell}}{A_{active,increment}}$$

Equation 30: Incremented active area along the length of the cell

$$A_{active,increment} = (2 * pi * (L_cell/NZ) * ((r[1] + r[4]) / 2))$$

Electrical losses, either referred to as overpotential or polarization, are incurred by the interconnects, the cell structure, and diffusion limitations by the cell. Ohmic overpotential, η_{ohmic}, stems from electrical losses through the interconnects and PEN structure [119]. Activation overpotential, $\eta_{activation}$, are losses that come from the need to overcome a specific energy barrier before electrochemical reactions can begin. In this thesis the electrolysis reaction incurs losses from the anode and cathode [120]. Concentration overpotential, $\eta_{concentration}$, is based on the resistance incurred when gas species are interacting and entering/exiting the PEN structure [121]. These losses are accounted for in Equation 31 by adding them to the Nernst open-circuit voltage. This convention is used because the Nernst voltage is the minimum voltage

supplied to allow for the cell to operate, with the sum of the losses indicating the actual required voltage for the electrolyzer to operate. The Nernst equation and respective overpotentials use voltage as the units to keep the calculations consistent.

Equation 31: Cell voltage accounting for activation, ohmic, and concentration losses

$$V_{cell} = E_{Nernst} + \eta_{activation} + \eta_{ohmic} + \eta_{concentration}$$

In the next section, these losses will be reviewed for modeling PCERs.

The Ohmic overpotential is made up of the PEN structure and interconnect losses shown in Equation 32.

Equation 32: Ohmic overpotential makeup equation

$$\eta_{ohmic} = \eta_{ohmic,PEN} + \eta_{ohmic,interconnect}$$

The ohmic resistance from the PEN structure relies on the current of the cell and electrode conductivity. The cell conductivity over a range of temperatures is extrapolated from Baral et. al. where they studied electrical properties of a Ni/NCZY cell [122]. The extrapolated conductivity equation from Baral et. al. is shown in Equation 33 [122].

Equation 33: resistivity of the PEN structure [122]

$$\sigma_{PEN} = -0.7667 * T_{PEN} + 2844.9$$

The units for conductivity, σ_{PEN}, of the cell were provided in $\frac{S}{m}$, which is the reciprocal to $\frac{\Omega}{m}$. The thickness of the PEN structure, t_{PEN}, and the active surface area, A_{active}, was used to obtain resistance, r_{pen}, in units of ohms (Ω) shown in Equation 34. The final equation for the ohmic resistance in the PEN structure, $\eta_{ohmic,PEN}$, is shown in Equation 35.

Equation 34: resistance in pen structure equation [122]

$$r_{pen} = \frac{t_{PEN}}{\sigma_{PEN} * A_{active}}$$

Equation 35: Ohmic overpotential of the PEN structure equation

$$\eta_{ohmic,PEN} = i_{cell} * r_{pen}$$

The ohmic losses from the interconnects, $\eta_{ohm\ \ ,interconnect}$, are obtained using the same equation framework as Norman et. al. shown in Equation 36 but with the interconnect area utilized, A_{IC}, because the area specific resistance (ASR), asr_{inter} ($\frac{\Omega}{m^2}$), is used instead of the conductivity.

Equation 36: Equation to obtain ohmic losses from interconnects in volts

$$\eta_{ohmic,interconnect} = i_{cell} * 2 * \left(\frac{asr_{inter}}{(A_{IC})}\right)$$

The area specific resistance is used from Huang et. al. where they studied the impact that oxide coatings have on metallic interconnects. The ASR across various temperatures were derived from graphs found in the work by Huang et. al. for nickel-coated interconnects and shown in Equation 37 [123].

Equation 37: Area-specific resistance for nickel-coated metallic interconnect

$$asr_{inter} = 0.0158 * e^{-0.009 * T_{PEM}}$$

The activation overpotential is calculated by adding the activation overpotential of the anode,$\eta_{act,an}$, and the cathode, $\eta_{act,ca}$ as shown in Equation 38.

Equation 38: Total activation energy equation

$$\eta_{act} = \eta_{act,an} + \eta_{act,ca}$$

The Butler-Volmer equation is used to calculate the activation overpotentials for the anode and the cathode as shown in Equation 39 and Equation 40 respectively [78], [124].

Equation 39: overpotential calculation for the anode using the Butler-Volmer Equation

$$i_{cell} = J_{0,an} * \left(e^{\left(\frac{\alpha_{an,an} * F * \eta_{act,an}}{R * T_{PEN}}\right)} - e^{\left(\frac{\alpha_{an,ca} * F * \eta_{act,an}}{R * T_{PEN}}\right)} \right) * A_{active}$$

Equation 40: overpotential calculation for the cathode using the Butler-Volmer Equation

$$i_{cell} = J_{0,ca} * \left(e^{\left(\frac{\alpha_{ca,an} * F * \eta_{act,ca}}{R * T_{PEN}}\right)} - e^{\left(\frac{\alpha_{ca,ca} * F * \eta_{act,ca}}{R * T_{PEN}}\right)} \right) * A_{active}$$

The symmetry factors, $\alpha_{an/ca,an/ca}$, represent the conversion balance between electrical and chemical energy, with more complex reactions requiring more energy at different components of the cell [125]. The symmetry factors for the anode were selected to be an even 0.5:0.5 because a more precise value was not found, and the symmetric assumption is common in electrochemical modeling. The symmetry factors for the cathode are obtained from Zhu et. al. and shown in Table 9. The exchange current density for the anode, $J_{0,an}$, and cathode, $J_{0,ca}$, are calculated using the method that Norman et. al. utilized shown in Equation 41. The activation energies, E_a, are modified from Norman et. al., using the anode activation energy for Ni/CeO_2 from Yang et. al. [126] and the cathode activation energy for activation energies for BCZYYb from Zhu et. al. [127] as shown in Equation 42 and Equation 43 respectively [78, 127].

Equation 41: General equation for the exchange current density

$$J_{o,an/ca} = J_o^* * e^{\frac{-E_a}{R * T_{PEN}}}$$

Equation 42: Exchange current density for the anode made of Ni/CeO2

$$J_{o,an} = 9.577 * 10^8 * e^{\frac{-25086}{R * T_{PEN}}}$$

Equation 43: Exchange current density for the cathode made of BCZYYb

$$J_{o,an} = 8.817 * 10^9 * e^{\frac{-8260}{R*T_{PEN}}}$$

The concentration overpotential is calculated using the same format and values as Norman et. al. because studies surrounding the concentration overpotential for Ni/CeO_2 were not found at the time of completing this thesis. The concentration overpotential considers the partial pressure for the oxygen, hydrogen, and water involved in the HER reaction as shown in Equation 44. The concentration losses at the cathode considers the ratio of partial pressures of the triple phase boundary and the bulk hydrogen because the cathode side should only consist of hydrogen. The anode concentration losses consider the diffusion site reduction while limit the transportation of hydrogen.

Equation 44: Concentration overpotential equation

$$\eta_{concentration} = \frac{R * T_{PEN}}{2 * F} * \ln\left(\frac{P_{H_2A,TPB}}{P_{H_2A,bulk}}\right) + \frac{R * T_{PEN}}{2 * F} * \ln\left(\frac{P_{H_2O,bulk} * {P_{O_2,TPB}}^{0.5}}{P_{H_2O,TPB} * {P_{O_2,bulk}}^{0.5}}\right)$$

The triple phase boundary pressures for water, $P_{H_2O,TPB}$, oxygen, $P_{O_2,TPB}$, and hydrogen, $P_{H_2,TPB}$, and are calculated using Equation 45, Equation 46, and Equation 47 respectively. The diffusivity coefficients found in Table 9 are directly used from Norman et. al. with their work quoting difficulty in model convergence when using values from literature [78].

Equation 45: Triple phase boundary pressure for water

$$P_{H_2O,TPB} = P_{H_2O} + \left(\frac{R * T_{PEN} * t_{an}}{2 * F * D_{ca} * 10^5 * j_{cell}}\right)$$

Equation 46: Triple phase boundary pressure for oxygen

$$P_{O_2,TPB} = P_{O_2} - \left(\frac{R * T_{PEN} * t_{an}}{4 * F * D_{ca} * 10^5 * j_{cell}}\right)$$

Equation 47: Triple phase boundary pressure for hydrogen

$$P_{H_2A,TPB} = P_{H_2A} - \left(P - P_{H_2A}\right) * \left(\frac{R * T_{PEN} * t_{ca}}{2 * F * D_{an} * 10^5 * j_{cell}}\right)$$

3.2.3: PCER Modeling Parameters

The model operates within certain constraints, assumptions, and input conditions. Table 9 outlines the model input variables that the model utilizes to operate.

Table 9: Model input variable assumptions

Variable	Operating Condition
Inlet Fuel Temperature (T_fuel_in)	600-1000K
Intel Air Temperature (T_air_in)	600-1000K
Current Density (J_cell)	2,000-10,000 A/m^2 [78], [128]
Inlet Pressure	101325 Pa
GHSV (1/h)	1,000,000-10,000,000 [113]
Universal Gas Constant (R)	8.314 J/mol*K
Faraday's Constant (F)	96485.4 C/mol
Pressure Change (ΔP)	$P[i] = p[i-1] - \frac{0.04}{NZ}$ [78]
Specific Anode Surface Area (SSA)	82 m^2/g [113]
Symmetry Factor, cathode (anode:Cathode)	0.3:0.7 [127]
Symmetry Factor, anode (anode:Cathode)	0.5:0.5
Anode Diffusivity Coefficient (D_{an})	3*10^{-5} [78]
Cathode Diffusivity Coefficient (D_{an})	3*10^{-6} [78]
Porosity (ϕ)	0.35[129]
Particle Density	8900kg/m^3[130]

The cell geometry uses the values shown in Table 10. The anode, cathode, electrolyte thickness is obtained as part of the project specifics for the Department of Energy project titled "Highly Replicable, and Integrated System for Mitigating Methane Emissions from Natural Gas Engines[131]." The fuel delivery tube thickness is obtained from Norman et. al. by adding the fuel delivery tube, tube thickness, and fuel conversion section between the pipe exterior and the anode. The air channel height was selected to correlate to air channel heights found in literature [124]. Due to various designs for the air channel design such as the one from Norman et. al. at 1mm and Naji et. al. with a height of 20mm, the impact that the air channel thickness has to hydrogen production will be analyzed.

Table 10: PCER cell geometry

Variable	Operating Condition
Cell Length	0.125m
Anode Thickness (t_an)	0.004m
Cathode Thickness (t_ca)	$20\ x\ 10^{-6}$m
Electrolyte Thickness (t_el)	$15\ x\ 10^{-6}$m
Fuel Delivery Tube Thickness (t_FDT)	$3\ x\ 10^{-3}$m
Fuel Delivery Tube radius (r_FDT)	$3\ x\ 10^{-3}$m
Air Channel Height (h_AirCh)	$2\ x\ 10^{-3}$m
Outer Tube Radius	0.08m

The model utilizes a real-world feedstock composition from an AJAX DPC 105. In order to obtain the composition of the exhaust gases from the respective engines, the MKS 3200 Gas

Analyzer was utilized. The MKS provides values in either percent composition or in parts per million (ppm). The terms in percentage do not need any further modifications while the specific chemical in ppm, ppm_i, is divided by 10,000 to obtain percentage as shown in.

Equation 48: Parts per million (PPM) to percent molar composition conversion equation

$$\%_i = \frac{ppm_i}{10{,}000}$$

The MKS outputs hydrocarbons, nitrous oxides, carbon oxides, water content, volatile organic compounds (VOC), and unburned fuels such as ethane and diesel from a natural gas-fed engine for example. The MKS does not output air content, so a piezoelectric NOx/O2 sensor is used. A summary of the primary emissions that the MKS and the NOx/O2 sensor output are in Table 11.

Table 11: Emission compounds obtained from the MKS 2030FTIR and NOxO2 amperometric sensors.

Gas	Analyzer Type	Parts Per Million (PPM) or %
NO, NO2, N2O, NH3, NOx	MKS	PPM
H2O	MKS	%
CO, CO2	MKS	%
CH4	MKS	PPM
VOC	MKS	PPM
Ethane, Ethylene, Propylene, Butane, Diesel Oil	MKS	PPM

O2	NOx/O2 Sensor	PPM

The fractional composition in percent is the sum of the present chemicals in the stream as shown in Equation 49.

Equation 49: Calculation used to find the molar concentrations of the DPC105

$$\%_{tot} = 1 = \sum \%_i + \%_i{}^c$$

$$\%_i{}^c = (1 - \sum \%_i)$$

Where $\%_i$ are each present chemical, the sum of the sensor compositions is the Total Senor Composition (TSC) from the MKS and NOx/O2 sensors, and the sum of the other components from the exhaust stream that were not directly measured. The sum of these unmeasured values is called the sum complement composition percent $\%_i{}^c$ shown in Equation 49. For the PCER model, the Nitrogen content was the sum complement composition percent from the sensor-obtained composition. The emission results from the hydrogen blending and spark ignition timing at a baseline at 11°BTDC with no hydrogen blending and at the optimized 11.5°BTDC with a hydrogen mole fraction of 20% are used in the PCER model. These emission results are shown in Table 12.

Table 12: Molar composition for model validation and for DPC105 exhaust stream at 60% load, 0H2%, 11 Degrees BTDC and 60% load, and 20H2%, 11.5 Degrees

Emission Type	11°BTDC, 0 H_2% (Mole Fraction %)	11.5°BTDC, 20 H_2% (Mole Fraction %)	Ideal Model Condition (Mole Fraction %)

CH4	0.275 + (5)	0.081 + (5)	0.25
H2O	6.893 + 40 Added	9.210 + 40 Added	0.75
CO	0.013	0.011	0
CO2	3.386	2.900	0
H2_fuel	0	0	0
H2_air	0	0	0
O2_fuel	9.99	10.704	0
N2 ($\%_i{}^c$)	39.443	37.094	0

We can see from the data that 79.443% of the composition is made up of nitrogen from the air, with water content, CO2, and oxygen making up a majority of the measured concentrations. These results are validated with comparisons to stochiometric combustion and literature on internal combustion natural gas (ICNG) engines shown in Equation 1. Due to the model requiring a high quantity of water to effectively operate the cell, a water concentration of 40% is added to the testing emissions for effective model convergence. Additionally, the electrochemical losses for concentration require at least 5% methane in the modified emissions to obtain a positive concentration loss. Although the negative losses are small enough to be considered negligible, the distinction will be made in this thesis within the results section.

3.2.3: PCER Model Testing Procedures and Validation

The PCER model is evaluated based on the concentration, the flow rate, and the electrochemical settings as shown in Figure 17. The concentration testing will focus on the impact that temperature has on the PCER unit by studying the exit concentration from the cell. The flow rate testing will focus on varying the flow rate to understand the impact that high flow

rates have on PCER reaction kinetics and the impact that this has to the exiting gas concentrations. The electrochemical cell operation will be tested by modifying the current density. The Nernst voltage, voltage losses, and estimated operating cell voltage will be analyzed for a range of current densities at an operating temperature of 673K, 873K, and 1000K. The temperature variation is important to study because the reaction kinetics vary drastically depending on the operating temperature of the cell. The flow rate and electrochemical tests will utilize both an idealized inlet gas composition and the engine emissions from the stark timing and hydrogen blending with 40% H_2O added to all engine cases. The concentration testing will also include the baseline emissions from the spark timing work.

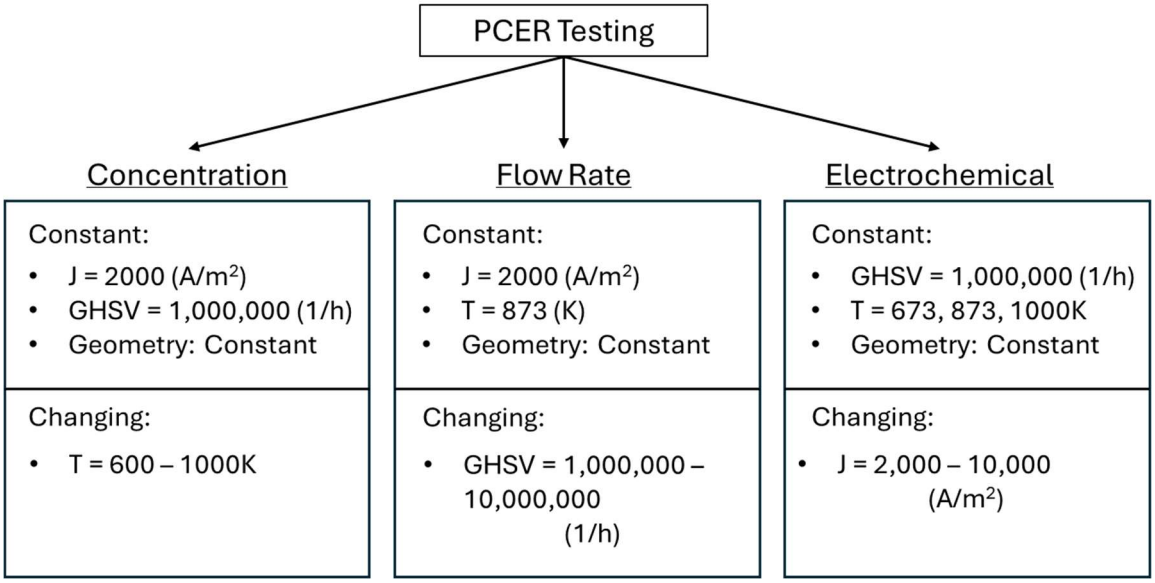

Figure 17: Testing procedures for the PCER model

As later discussed in this thesis, the concentration testing reveals that the engine emissions require an added 5 mol% of methane to reduce the likelihood of the reaction kinetics to go backwards and utilize hydrogen. Because of this, the modified engine emissions for the flow rate and electrochemical testing will add 5 mol% of methane to the observed concentration.

A tubular PCER utilizing Ni/CeO2 for the anode and Ni/BCZY for the electrolyte and cathode has not been manufactured at the time of completing this thesis. Because of this, the results will be used as rough estimates to complete the combined mass balance analysis in Aspen HYSYS and obtain a theoretical value as to the minimum operational temperature that the cell could operate at while mitigating methane emissions. The reaction kinetics for SMR and WGS are validated by matching the methane conversion percentage while operating the model at the same inlet composition, temperature range, and similar flow rate.

3.3: Combined PCER/Engine Modification System Modeling

The combination of engine modification experimental data and modeling data from the PCER model is conducted using Aspen HYSYS. Aspen HYSYS is a process flow and equipment simulation software that allows for the modeling of engineering equipment. In this section we will be looking at the modeling theory and procedures taken in modeling the combined ignition timing, hydrogen blending, and PCER exhaust conversion cell. The HYSYS model integrates heaters, control valves, and a hydrogen balance system to optimize system operation.

3.3.1: Engine Modeling Methodology and Testing Procedure in HYSYS

The Aspen HYSYS model is used to simulate system components that either do not exist or are not directly measured. This thesis the HYSYS model is utilized to (1) obtain flow rates for blending hydrogen in the natural gas stream of an AJAX DPC 105 natural gas compressor and (2) to simulate the pre-stream treatment between the DPC 105 exhaust and the PCER unit. The hydrogen blending is depicted in the hydrogen blending results section, so the HYSYS modeling section focuses on the exhaust gas treatment. The exhaust gases measured with an MKS 2030 FTIR are used in the “exhaust” stream for when the engine is set to 11.5° BTDC with a hydrogen blend of 20 mol% as shown in Figure 18. Adjusters are utilized to modify the molar flow rate of

the water and methane stream to match the composition that is used in the PCER testing. The blended stream is sent through a heater to increase the stream temperature to 500℃ to obtain an estimate for the relative size requirements for the heater.

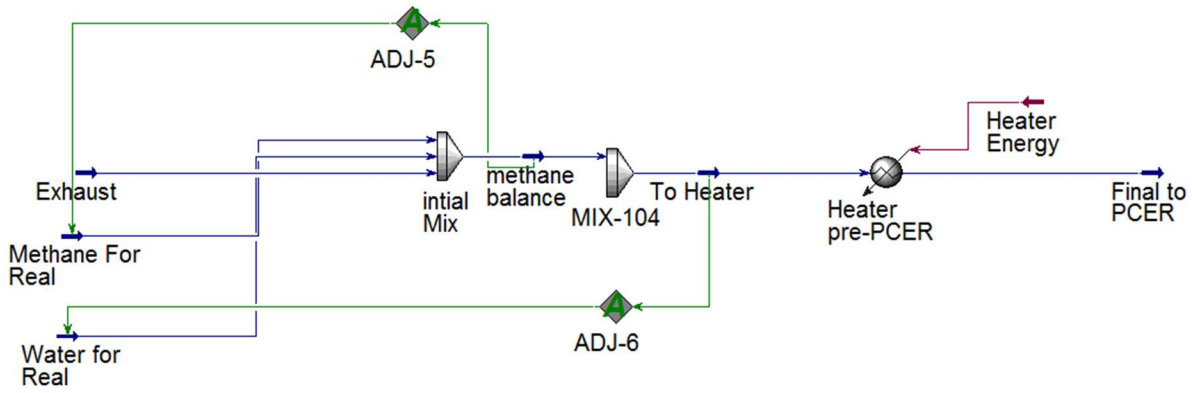

Figure 18: Aspen HYSYS engine simulation

Chapter 4: Results

4.1: Spark Ignition and Hydrogen Blending Results

The operational parameters for the 60% engine load data are summarized in Table 13. The variation in mass flow when no hydrogen is added, as shown in Figure 19, occurs because the input natural gas is balanced between the compression and combustion sections of the engine, with variations being considered for each condition change and engine turn off and restart to change the angle. The fuel line temperature was found to have a large impact on the mass flow rate of the natural gas supply, with higher fuel temperatures dropping the natural gas mass flow and lower temperatures increasing the mass flow.

Table 13: Fuel stream conditions for 60% load testing

Angle (BTDC)	H2%	Temperature (F)	NG M Flow (lb/min)	Heating Value (KJ/Kg)	H2 V Flow (scfm)
12	0	98.01	0.45	54600	0
	10	97.47	0.43	55690	0.325
	20	98.54	0.41	57040	0.730
11.5	0	91.77	0.46	54600	0
	10	93.89	0.43	55690	0.325
	20	95.77	0.41	57040	0.730
11A	0	51.21	0.54	54600	0
	10	50.37	0.51	55690	0.354
	20	51.51	0.48	57040	0.801
11R	0	43.31	0.54	54600	0
	10	44.89	0.51	55690	0.354

	20	45.76	0.48	57040	0.801
10	0	50.93	0.51	54600	0
	10	52.01	0.48	55690	0.331
	20	51.61	0.46	57040	0.74
9	0	52.05	0.51	54600	0
	10	52.23	0.48	55690	0.331
	20	52.07	0.46	57040	0.74

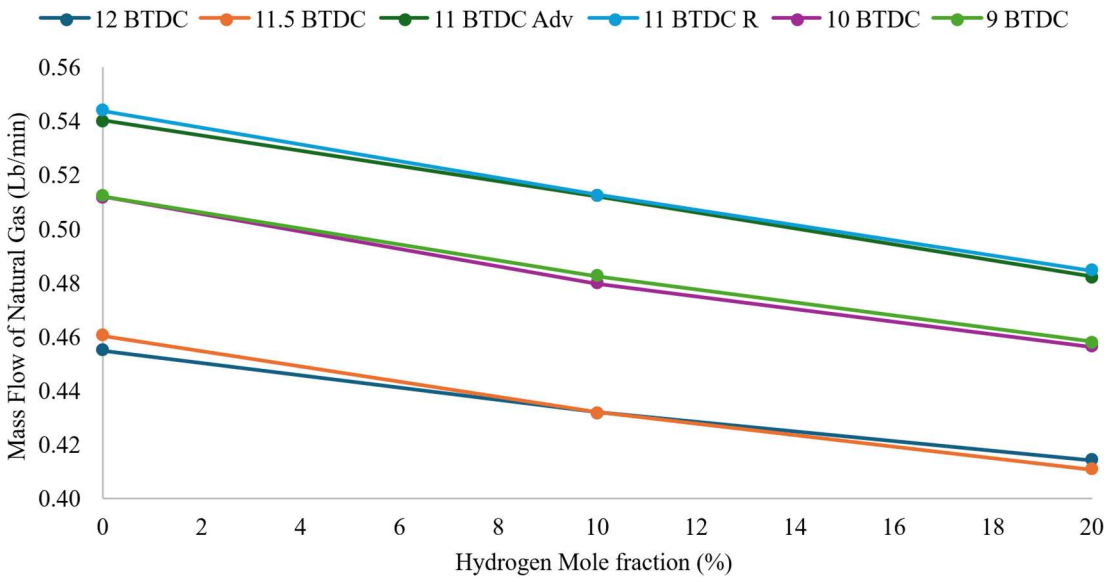

Figure 19: Natural gas mass flow rates across different hydrogen concentrations and spark ignition timings. The spark timing angles are shown in units of before top Dead center (BTDC).

The engine load was found to vary up to 2.8% engine load for time advancing and 1.5% engine load for time retarding across different hydrogen percentage shown in Figure 20. This variation occurs when the temperature changes during the day and the fuel flow rates change between engine startup and shutdown. This variation is analyzed as we look at the emission data and

thermal efficiency. With the engine operational characteristics analyzed, we will now look at the engine emissions when modifying the fuel contents and spark ignition timing.

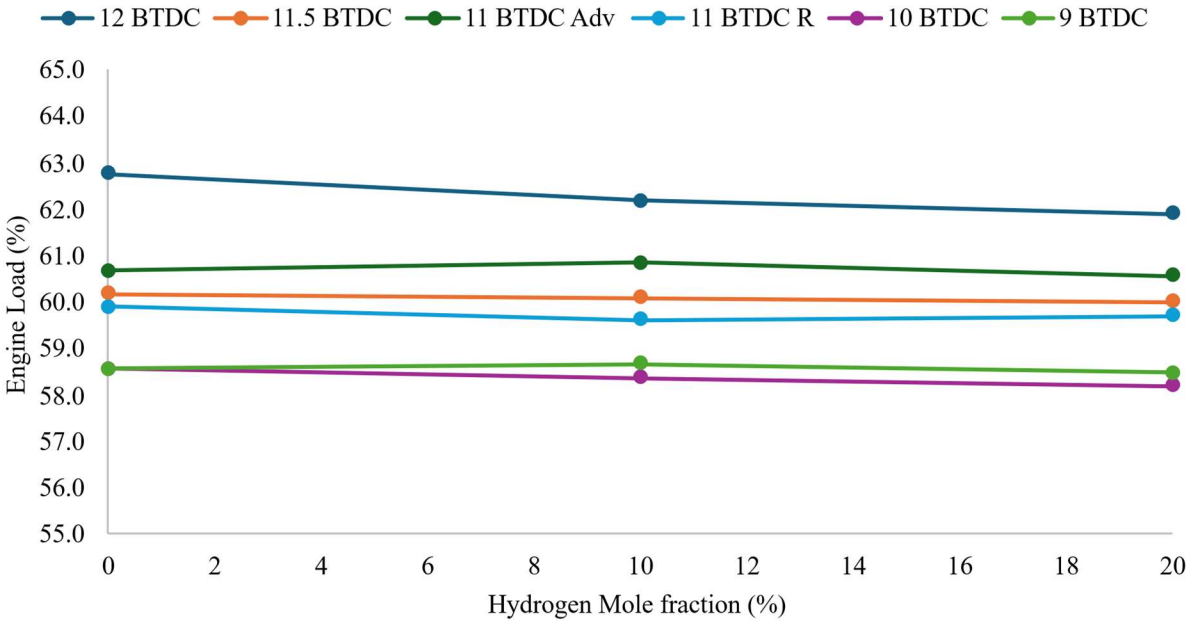

Figure 20: AJAX DPC105 Engine load variation from 60% during testing.

4.1.1: Spark Ignition and Hydrogen Blending Emission Results

4.1.1.1: Methane Emissions

The methane emissions results shown in Figure 21 will be reviewed by separating the advancing and retarding datasets, with both timing events containing their own baselines shown as “11BTDC Adv” and “11BTDC R” respectively. This difference is taken because the data was taken on different days, changing the MKS gas analyzer calibration. Although this should not impact the results, the distinction will still be made. The hydrogen blending is found to unanimously reduce the methane emissions from the engine at all spark timing angles. When looking at advancing the spark timing, the addition of 10% and 20% hydrogen at a spark timing of 11° BTDC resulted in a 16.2% and 35.3% reduction in methane emissions respectively. The

baseline of 11° BTDC for retarding spark timing also saw a reduction in methane emissions, with the addition of 10% and 20% hydrogen resulting in a methane emission reduction of 14.1% and 24.8% respectively. The observed reduction in methane emissions can be accounted for by a decrease in hydrocarbon content in the fuel and an increase in thermal efficiency. The mechanism for which the methane reduction takes place is validated by analyzing the thermal efficiency.

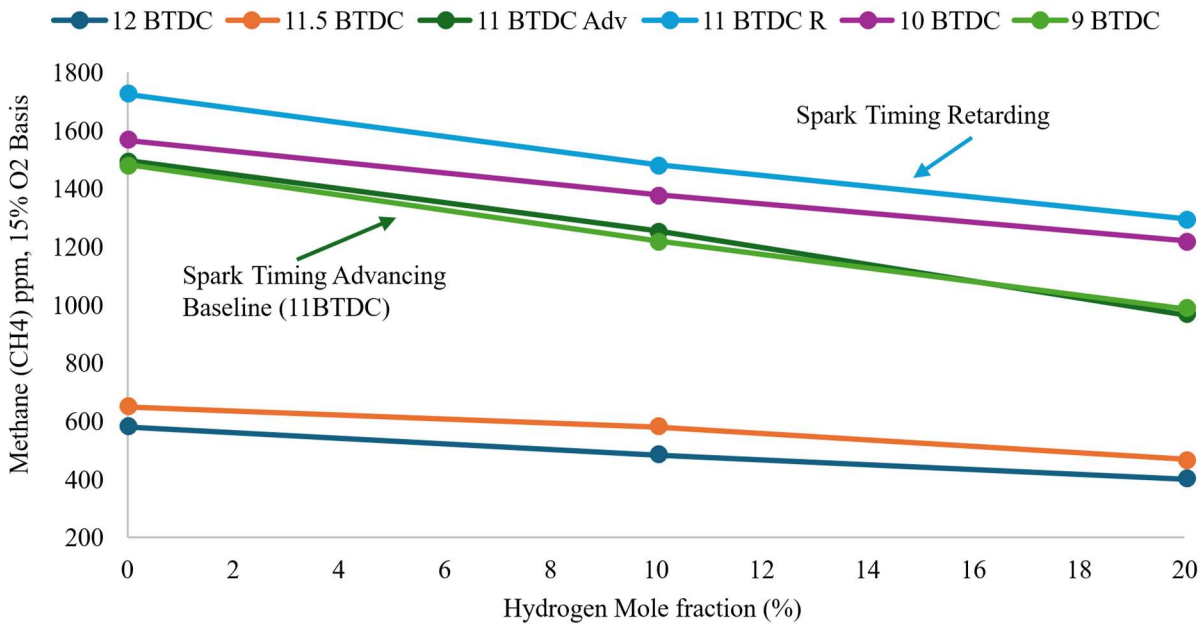

Figure 21: methane emission results for hydrogen blending 0-20% mole concentration and ignition timing from 12BTDC to 9BTDC

Methane emission reductions are also observed at different angles when hydrogen blending is conducted, with 9° BTDC and 12° BTDC being used to represent the changes for retarding and advancing the spark timing respectively. When the engine is set to 9° BTDC, the methane emissions at 10% and 20% hydrogen mixes were reduced by 17.5% and 33.2% respectively from 9° BTDC at 0% H_2. When the engine is set to 12° BTDC, the methane

emissions at 10% and 20% hydrogen mixes were reduced by 16.7% and 30.8% respectively from 12° BTDC at 0% H_2. The impact that hydrogen blending has at a set spark ignition timing angle was quite similar, showing that the hydrogen reduced methane emissions due to the reduction in methane content for that angle. We will now investigate the impact that Spark timing has on methane emissions and then look at the combined effect of blending hydrogen and modifying the spark ignition timing.

Modifying the spark ignition timing changes the time at which the spark fires in the piston cycle, either reducing or increasing the combustion chamber volume that the flame has to propagate whether the timing is retarded or advanced respectively. This will in turn either reduce or increase the time that the combustion process has to occur before the gases are exhausted. To study the direct impact of modifying the spark timing, the methane emissions are graphed in Figure 22 at a condition when no hydrogen is blended into the fuel stream. By isolating the change in methane content without adding hydrogen, we can see the impact that spark timing has on the emissions.

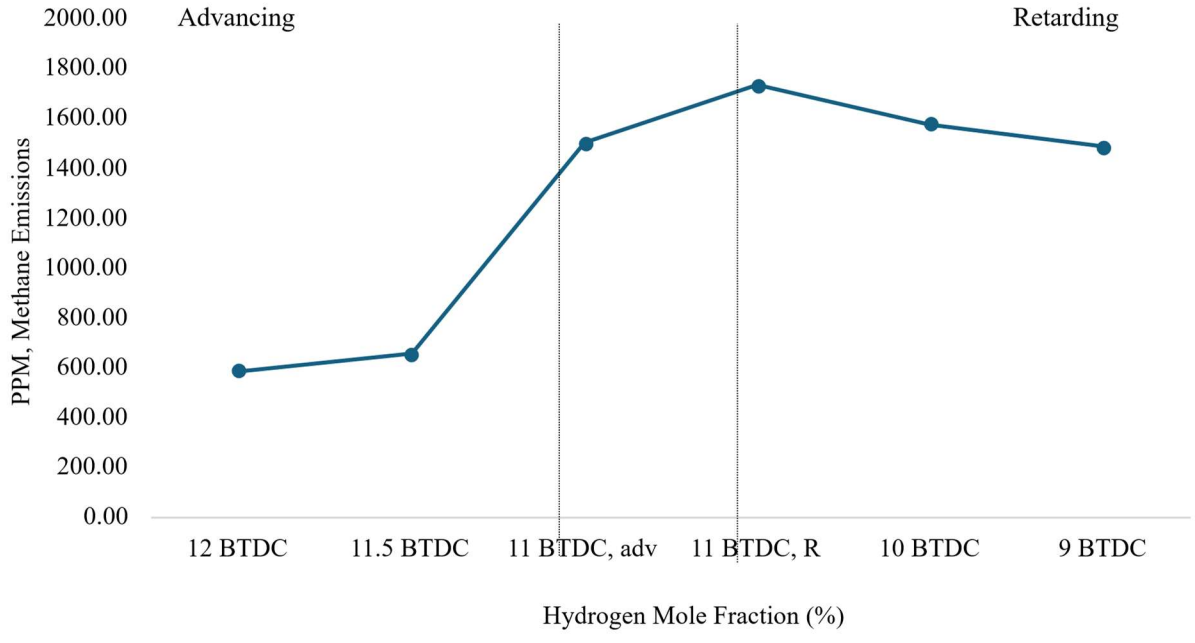

Figure 22: Methane ppm at different spark ignition timing separated by advancing to the left and retarding on the right

Advancing the timing to 11.5° BTDC and 12° BTDC resulted in a 56.4% and 60.9% reduction in methane emissions. Retarding the timing to 10° BTDC and 9° BTDC resulted in a 9.3% and 24% reduction in methane emissions. The methane emissions were found to drop when the timing was modified from the baseline angle of 11° BTDC, with advancing the spark timing having a greater effect on the methane output when compared to retarding the spark timing. We can now further into the impact that spark timing across the different hydrogen blending concentrations while still only analyzing spark timing conditions by focusing on the difference that spark timing makes at the same hydrogen content conditions from the baseline conditions. This represents the difference in methane emissions from the baseline spark timing at the same hydrogen blend, so a setting of 12° BTDC at 20% hydrogen blend would represent the methane change from 11° BTDC at 20% hydrogen. With this clarification being made, we can see in Figure 23 that modifying the spark timing reduced the methane concentration for both advancing and retarding of the spark timing. Advancing the timing had a far greater reduction in methane emissions when compared to retarding the spark timing across all hydrogen concentrations, which validates the observations from Figure 22 where hydrogen is not considered. For the spark advancing data, the difference in hydrogen inclusion makes less of an impact as more hydrogen is added, showing that the impact that spark timing has on methane emissions is reduced. This phenomenon occurs because hydrogen is already reducing methane emissions at the baseline angle, reducing the impact that hydrogen blending has at higher angles. The difference that hydrogen blending had to the retarding spark data is more complex, with 10° BTDC benefiting slightly at a change of 9%, 7%, and 6.1% at 0-20% hydrogen mole fractions respectively. At 9° BTDC, the later spark

timing starts to impact the combustion efficiency, with the faster flame propagation that a blended natural gas and hydrogen fuel line would offer. The change in methane emission was found to be 14.2%, 17.6%, and 23.8% for 0-20% hydrogen mole fraction respectively. The effectiveness that spark timing has when compared to blending hydrogen at the baseline angle was found to make less of an impact at 10° BTDC when compared to 9° BTDC which saw a reduction in methane emissions at all the comparative hydrogen mole fractions. Now the impact that hydrogen blending and spark timing is conducted.

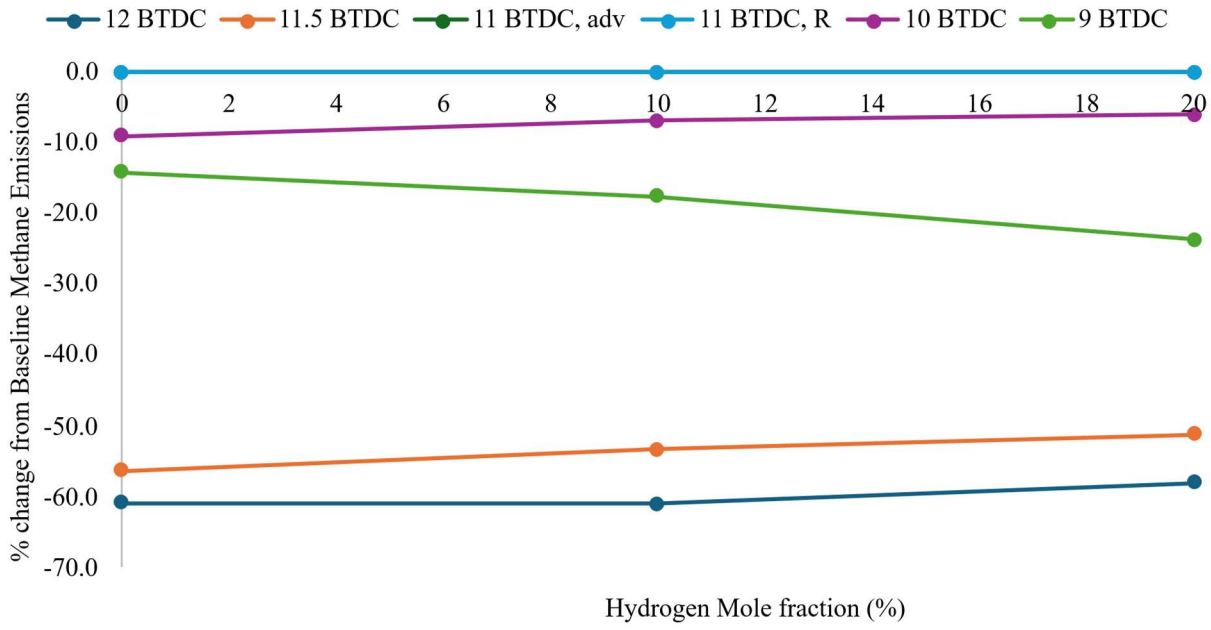

Figure 23: Change in methane emissions from baseline compared to the hydrogen mole fraction blended into the natural gas stream

An analysis of how the timing and the blending impacted the methane emissions is conducted by comparing the emission values from each angle and hydrogen content to the baseline angle, 11° BTDC, with no added hydrogen. This data is presented in Figure 24, with the hydrogen blending and spark angle change reducing methane emissions for all angles from the baseline measurements. Advancing the timing is observed to have the largest methane emission

reduction effect, with 12° BTDC at a hydrogen mole fraction of 20% observing a methane emission reduction of 72.9%.

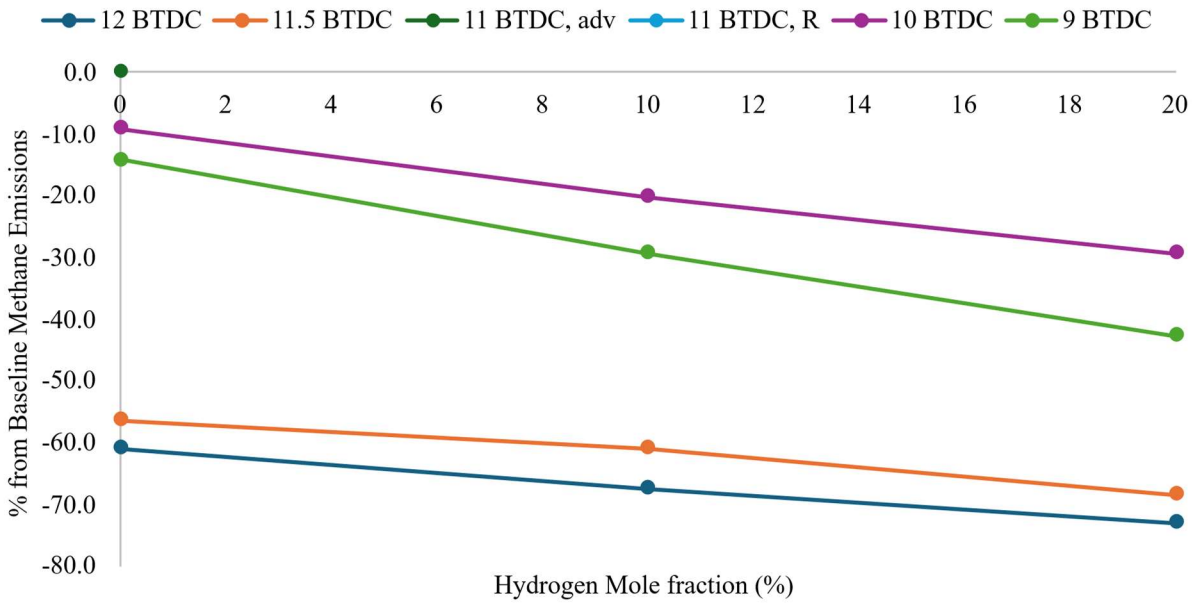

Figure 24: Percent change in methane emissions for advancing and retarding spark times at hydrogen mole fractions of 0%, 10%, and 20% compared to the baseline angle with no hydrogen addition

Although these results would indicate that advancing the timing would have a greater effect, the average peak pressure per angle and indicated mean effective pressures need to be analyzed.

The mean peak pressure represents how much force is being applied to the piston across 251 piston cycles. In combination with the IMEP, these pressure values can be used to validate the safety of operating the engine at a specific spark timing. We can see from Figure 25 that the maximum pressure values for the retarding spark timing are reduced, which is to be expected. With less time for the combustion process to occur, the flame propagation would not have enough time to build up as much pressure as the baseline setting. The surprising result for the retarding dataset is that the mean peak pressure was not increased when hydrogen was included,

meaning that the thermal efficiency must have increased in order to obtain a lower methane emission value. This theory will be validated by looking at the thermal efficiency data in the next section. Advancing saw lower pressures up until the angle and H_2% of 12° BTDC at 20% where the mean peak pressure matched the 11° BTDC at 20% condition. Analyzing the peak pressures demonstrates that the modification of the spark ignition timing with hydrogen blending does not impact the in-cylinder pressure to an unsafe condition.

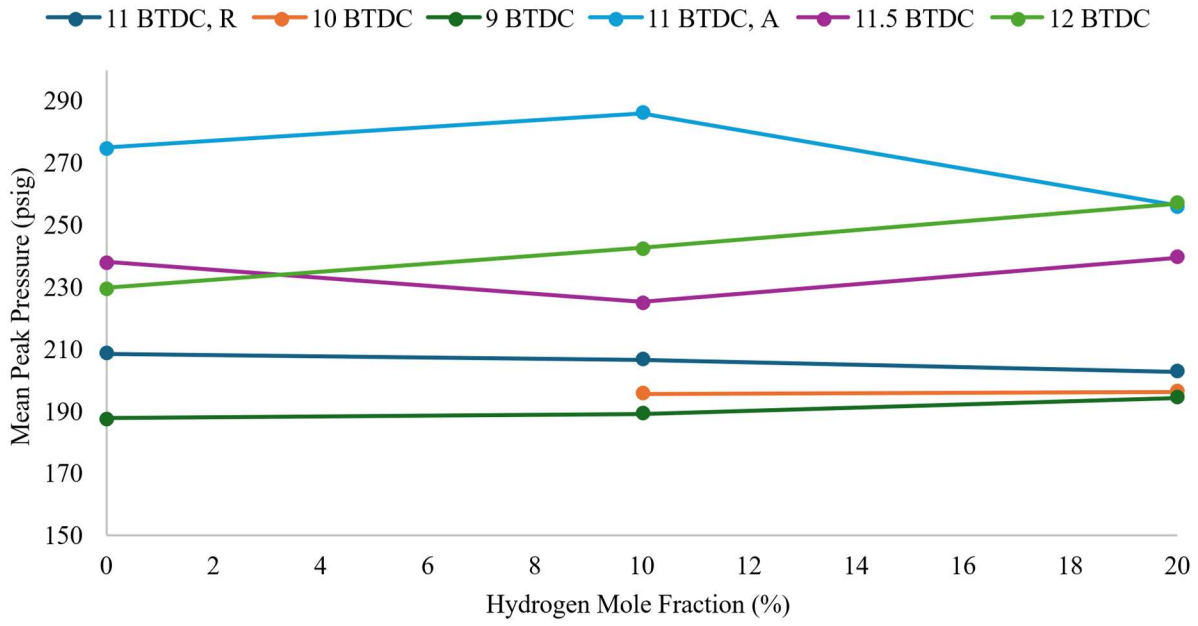

Figure 25: Mean maximum pressure readings across 251 engine cycles at different spark ignition angle across 0,10, and 20% hydrogen molar fraction

4.1.1.2: CO_x and NO_x Emissions

Carbon oxides, CO_x, are calculated by adding the carbon monoxide, CO, and carbon dioxide, CO_2, contents coming from the exhaust stream of the engine. CO_x are based on available oxygen and carbon molecules, with CO being the first in the reaction path and then converted if another oxygen is available. The CO and CO_2 exhaust from the AJAX DPC-105 at a load of 60%

are shown in Figure 26 and Figure 27 respectively. CO and CO_2 are inversely proportional for engine efficiency, with a higher CO concentration indicating less complete combustion and a higher CO_2 indicating more complete combustion. The CO concentration in Figure 26 was found to increase as hydrogen was added, with the exception of 11.5° BTDC and at 11° BTDC with a hydrogen mole fraction of 20%.

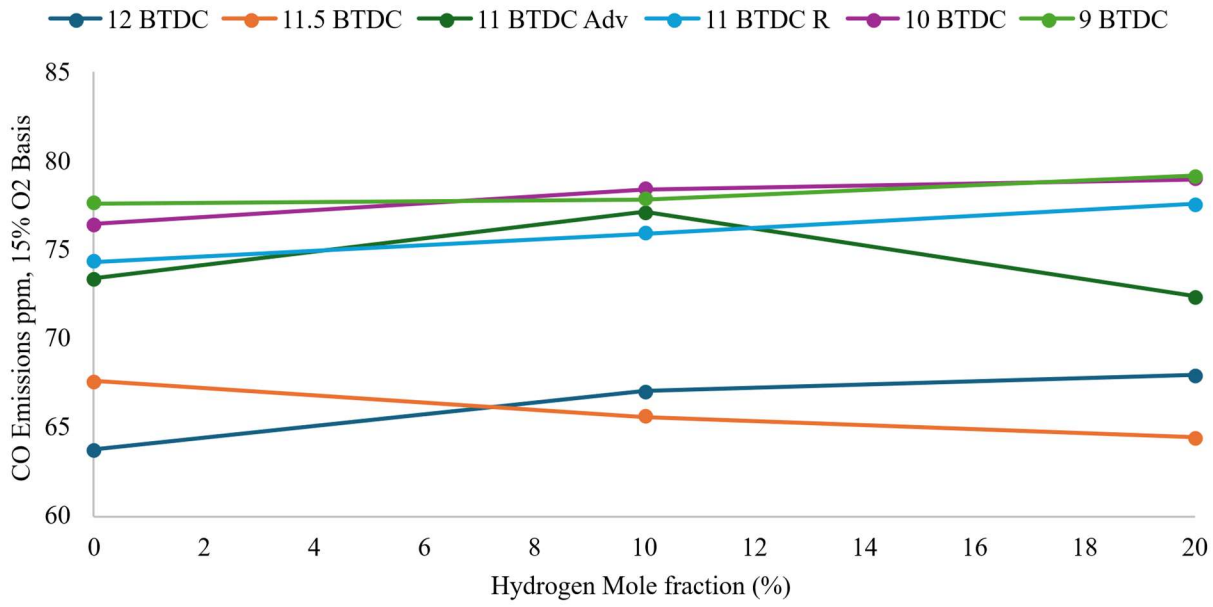

Figure 26: Carbon monoxide ppm at 15% O2 across a hydrogen blend mole fraction between 0-20%

Retarding the spark timing was found to increase the CO emission output at all hydrogen blends. At a setting of 10° BTDC, the difference between the baseline and modified time at the same hydrogen concentration observed an increase of 2.9%, 3.2%, and 1.8% difference at 0%, 10%, and 20% hydrogen blend respectively. When we look at the difference between the baseline with no hydrogen and the modified time at different blends, an increase of 2.9%, 5.5%, and 6.3% are observed at hydrogen blends of 0%, 10%, and 20% mole fraction respectively. At a setting of 9° BTDC, the difference between the baseline and modified time at the same hydrogen concentration observed an increase of 4.4%, 2.5%, and 2% difference at 0%, 10%, and 20%

hydrogen blend respectively. When we look at the difference between the baseline with no hydrogen and the modified time at different blends, an increase of 4.4%, 4.8% and 6.5% are observed at hydrogen blends of 0%, 10%, and 20% mole fraction respectively. These increases, although observed, are statistically insignificant below a 5% emission variation. Advancing the spark timing reduced the CO emissions when compared to the baseline, but the trends between the two concentrations seemed to follow opposite patterns when hydrogen was added. When 11.5° BTDC is compared to the baseline set to no hydrogen addition, a reduction of 7.9%, 10.6%, and 12.2% is observed at a hydrogen mole fraction of 0%, 10%, and 20% respectively. When 12° BTDC is compared to the baseline set to no hydrogen addition, a reduction of 13.2%, 8.7%, and 7.4% is observed at a hydrogen mole fraction of 0%, 10%, and 20% respectively. The 12° BTDC condition got worse as more hydrogen was added to it, which is the opposite trend to The baseline and 11.5° BTDC spark timings. This trend continues with the CO_2 data shown in Figure 27, with 12° BTDC emission increasing consistently by 5.1% and 6.6% as hydrogen is added to the fuel stream in mole fractions of 10% and 20% respectively. In contrast, the advancing baseline had a reduction in methane emissions of 3.9% and 6.9% as hydrogen mole fractions of 10% and 20% were added to the fuel stream. All the retarding timings and an advanced timing of 11.5 ° BTDC all increases the CO_2 emissions when 10% hydrogen is added to the stream and then drops back down at a hydrogen mole fraction of 20%.

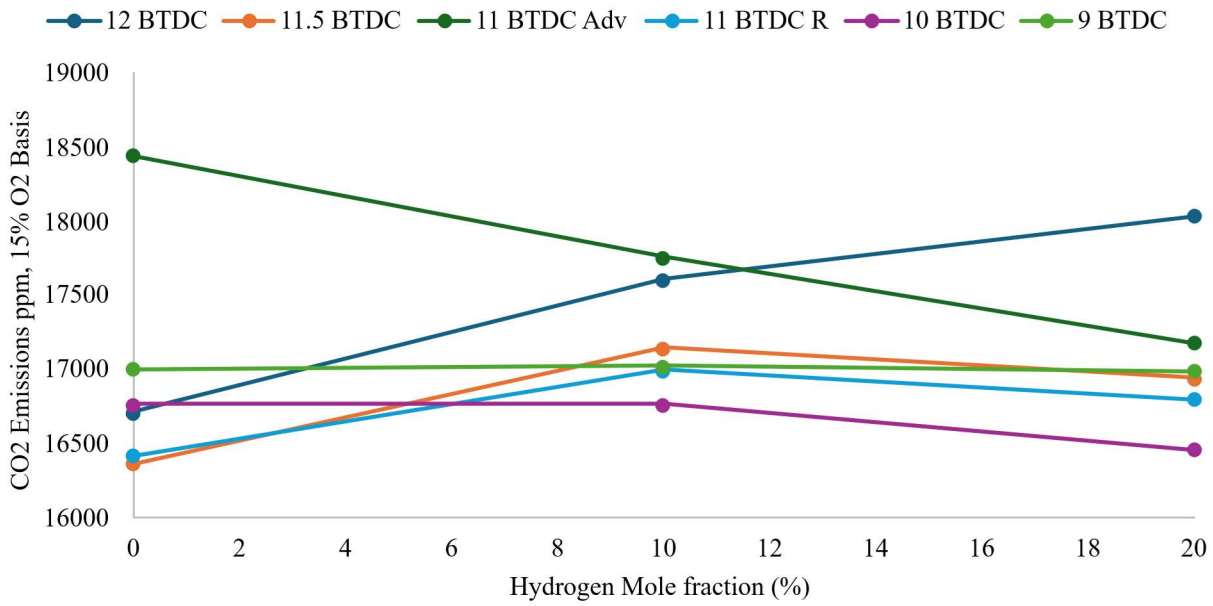

Figure 27: Carbon dioxide ppm at 15% O2 across a hydrogen blend mole fraction between 0-20%

The increase in CO and CO_2 that 12° BTDC observed could be an indication that the spark is occurring too early, with more time to complete the combustion reaction reducing the time needed for the oxidation reaction to occur between the CO and CO_2. The conversion requires proper time and temperature to complete the reaction, so the faster flame propagation may be restricting this reaction and instead favoring the incomplete combustion of methane and oxygen to CO.

Nitrogen Oxides, NO_x, mostly nitrogen oxide, NO, and nitrogen dioxide, NO_2, are directly related to the combustion temperature as discussed in previous sections. The results for nitrogen Oxides are shown as the sum of nitrogen oxide and nitrogen dioxide. The NO_x results in Figure 28 are found to reduce across all spark timing angles as more hydrogen is added. When we look at specific spark angles, advancing and retarding the timing is found to reduce NO_x emissions when compared to baseline. When the NOx trends are compared to the temperature in Figure 29, we see that the addition of hydrogen does reduce the operational temperature. When

the timing is advanced, 11.5° BTDC was found to reduce NO_x emissions less than 12° BTDC. When we compare this to the temperature trend, a general increase in temperature is observed as the timing is further advanced. The retarding data saw a similar trend to the advancing data when comparing the temperature trends and the NO_x emission data. The NO_x emissions are reduced at 9° BTDC more than at 10° BTDC, with the emissions at 10° BTDC being lower than at 11° BTDC. The exhaust temperature with no hydrogen addition saw a direct increase as the spark timing was retarded. When the hydrogen was added, the differences between the retarding spark timings and the baseline were diminished. When the timing is compared to the baseline with the same hydrogen content, 10° BTDC saw an increase of 1.6%, -0.5%, and 0.4% at 0%, 10%, and 20% hydrogen mole fraction respectively. At 9° BTDC, an increase of 4.1%, 3.4%, and 4.1% is observed at 0%, 10%, and 20% hydrogen mole fraction respectively. These differences would be considered negligible for 9° BTDC and 10° BTDC spark timings respectively. This would indicate that adding hydrogen at a concentration of 10% negates the impact that modifying the angle has on retarding the spark timing.

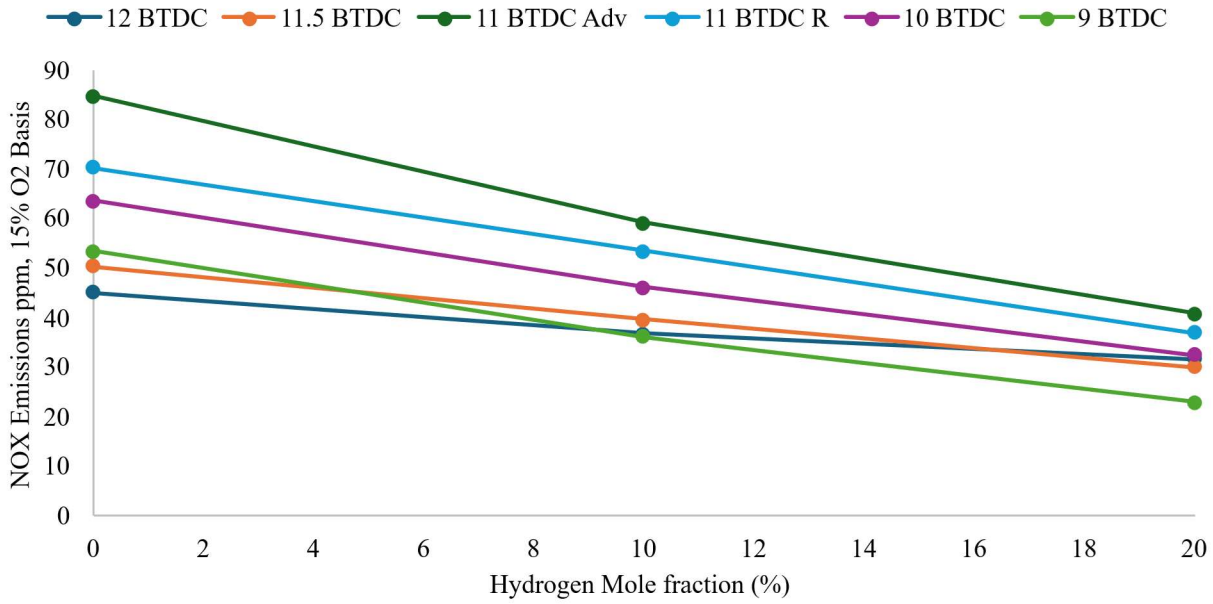

Figure 28: Nitrogen oxides (NOx) ppm emissions at different angles across 0-20% hydrogen mole fraction of blending into natural gas

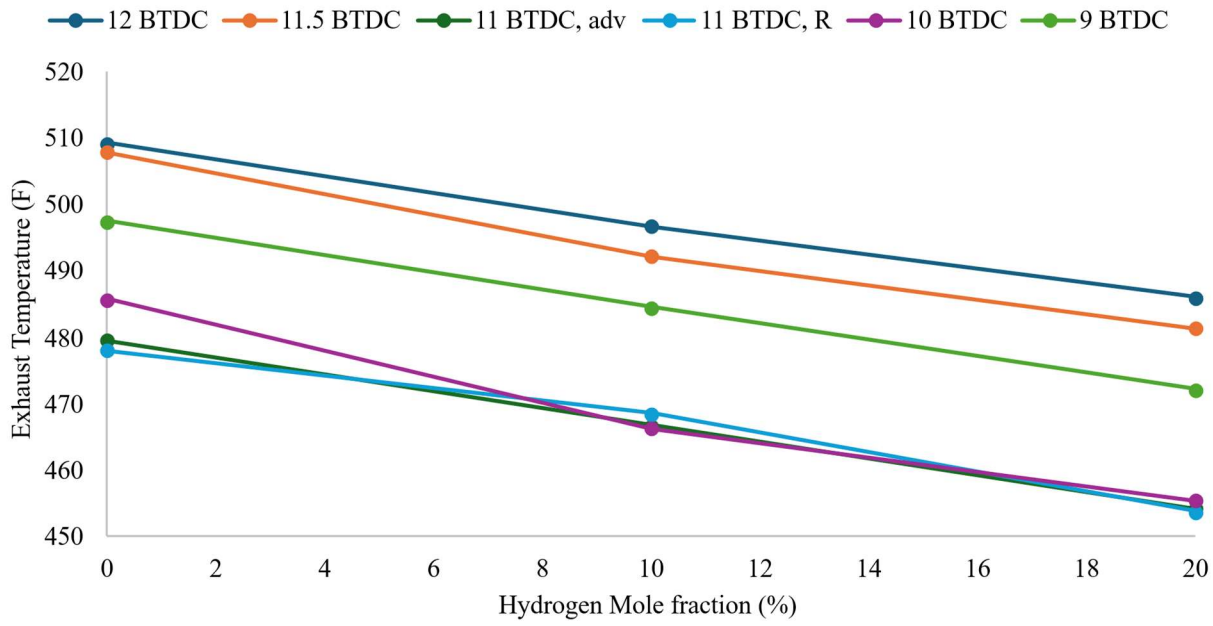

Figure 29: Exhaust temperature vs. blended hydrogen mole fraction

The emission results for methane, CO_x, and NO_x indicate that advancing the spark timing to 11.5° BTDC would provide the best balance of emissions, but this hypothesis will be validated by analyzing the indicated thermal efficiency.

4.1.2: Spark Ignition and Hydrogen Blending Efficiency Results

The thermal efficiency is dependent on the combustion chamber volume, combustion pressure, engine RPM, fuel flow, and thermal energy that the fuel provides. The thermal efficiency is used to validate the results obtained in the emission analysis. We will first look at the impact that spark timing has on the thermal efficiency without hydrogen addition and then look at the impact that hydrogen addition has on the thermal efficiency has on each angle. We can see in Figure 30 that advancing the spark timing increases thermal efficiency for both 11.5° BTDC and 12° BTDC with an observed increase of 16% and 19% respectively. Retarding the spark timing to 10° BTDC and 9° BTDC observed an increase of -0.15% and 3.58% respectively. These results indicate that advancing spark timing increases the thermal efficiency, while advancing has minimal impact on the thermal efficiency of the system.

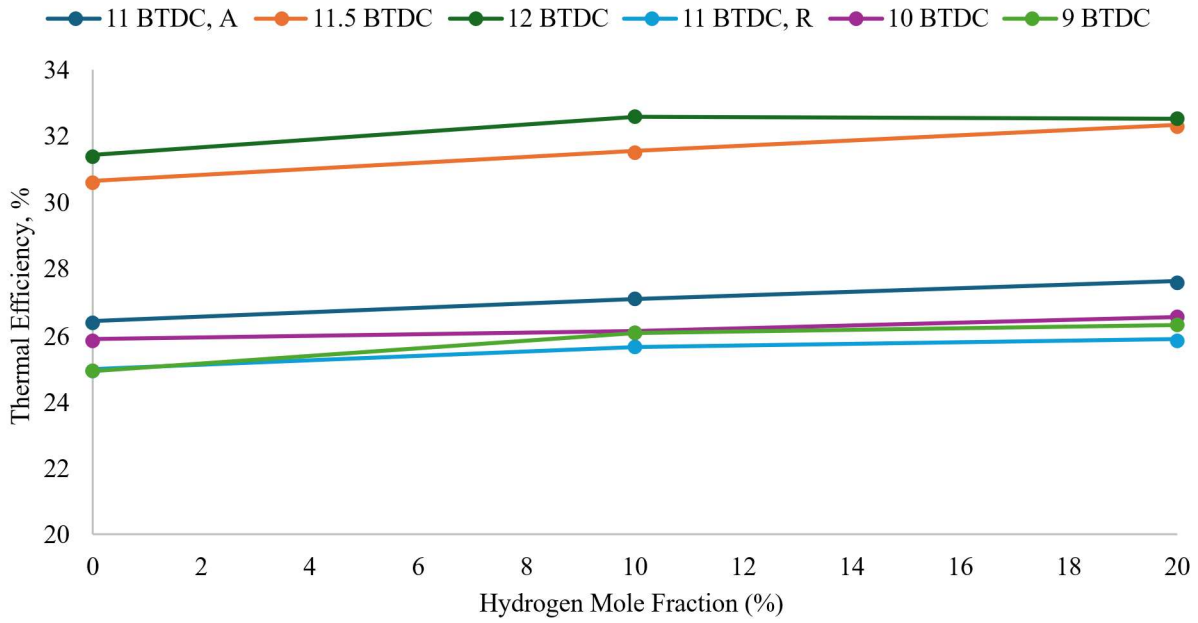

Figure 30: Indicated thermal efficiency compared to hydrogen blending mole fraction across different spark timings

This result makes sense when we look at the mean effective pressure in Figure 31, with retarding of the spark timing also reducing the effective pressure of the combustion cycle. The advancing data did see a reduction in effective pressure, but not to the extent than what was observed in the retarding data.

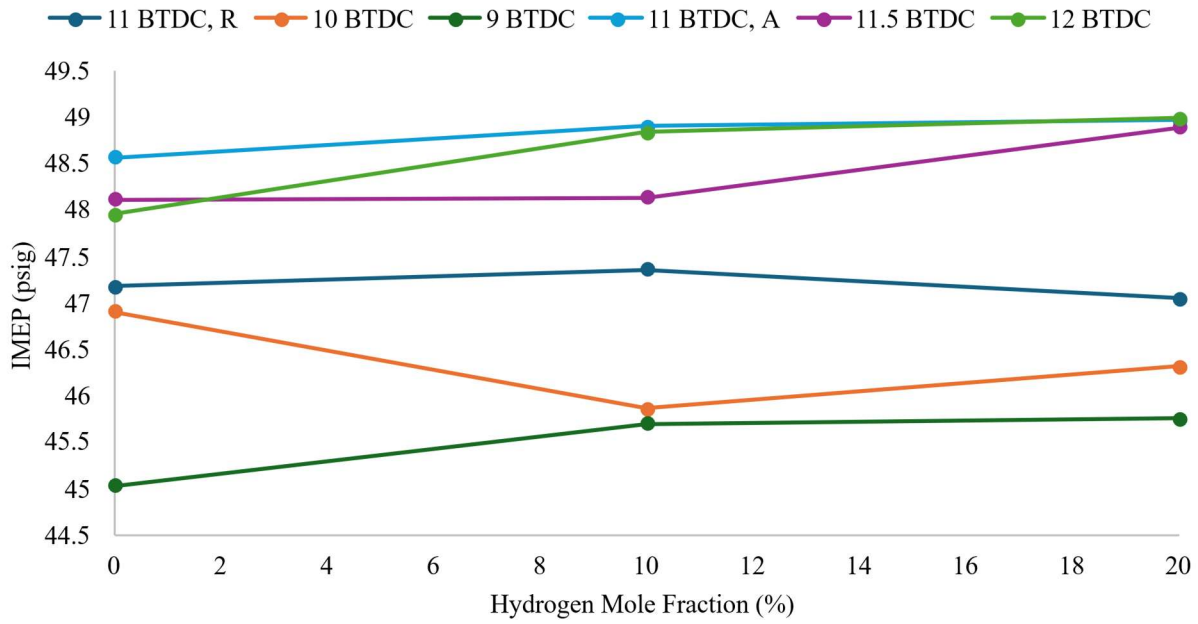

Figure 31: IMEP compared to the hydrogen blending mole fraction across different ignition spark timing angles

When hydrogen is blended into the fuel line, the difference between 10% hydrogen blending and 20% hydrogen blending was found to be minimal. When the baseline is compared to 10% hydrogen blending, the advanced and retarded spark timings are found to increase thermal efficiency. At 11.5° BTDC, blending hydrogen to 10% and 20% mole fraction saw an increase in efficiency of 0.9% and 1.2% respectively. At 12° BTDC, blending hydrogen to 10% and 20% mole fraction saw an increase in efficiency of 1.2% and 1.1% respectively. The advancing baseline of 11° BTDC saw an increase of 0.7% and 1.2% with a blending mole fraction of 10% and 20% respectively. The small differences that 11° BTDC, 11.5° BTDC, and 12° BTDC observed when hydrogen concentrations were increased indicates that the spark timing angle has no further impact to the thermal efficiency past the initial increase when no hydrogen is added. Although the difference would be considered insignificant, 12° BTDC saw a slight reduction in thermal efficiency when more hydrogen was added. This result further indicates that 11.5° BTDC is a more optimal angle when combined with hydrogen blending, as consistent increase was observed as more hydrogen was added. The retarding spark timing angles noticed a smaller variation as hydrogen was added. At a spark angle of 10° BTDC, the addition of 10% and 20% hydrogen resulted in an efficiency gain of 0.25% and 0.68% respectively. At a spark angle of 9° BTDC, the addition of 10% and 20% hydrogen resulted in an efficiency gain of 1.15% and 1.38% respectively. The baseline spark angle of 11° BTDC saw an efficiency gain of 0.69% and 0.89% when 10% and 20% hydrogen was added to the fuel stream respectively. The baseline spark angle observed a greater impact to the efficiency when compared to 10° BTDC, with 9° BTDC observing a marginal gain in efficiency. The efficiency of 9° BTDC at 10% hydrogen was able to match that of 10° BTDC, indicating that the blending of hydrogen at 10° BTDC does not

make much of an impact. After analyzing the emissions and engine operational conditions, the 11.5° BTDC with a hydrogen mole fraction blend of 20% into the natural stream provides the best overall engine conditions and emission reductions.

4.1.3: Spark Ignition and Hydrogen Blending Emission Validation Results

In order to validate the observed emission and thermal efficiency results, the results were repeated on the AJAX DPC-105 at a load of 55% load at spark angles of 10°-, 11°-, and 12° BTDC, with 9°BTDC and 11.5°BTDC being excluded to keep the angle changes within +/- 1°BTDC from a baseline angle of 11°BTDC. The emissions are analyzed, followed by the IMEP, mean peak pressure, and efficiency results. Due to the lower load condition the results will not be directly compared, but instead the general trends will be compared. A lower load on the engine will lead to higher general emissions, so the combustion characteristics will differ slightly from a 60% load condition.

4.1.3.1: 55% Load Emissions Analysis for Hydrogen Blending and Spark Timing

The methane emission results for 55% load, as shown in Figure 32, have similar trends for both advancing and retarding spark data. When hydrogen was blended into the natural gas stream, the baseline for advancing saw a reduction of 40% and 65.7% methane emissions at hydrogen mole fraction blends of 10% and 20% respectively. At a spark angle of 12°BTDC, methane emissions were reduced by 32.6% and 55.6% at hydrogen mole fraction blends of 10% and 20% respectively. Switching to the retarding baseline, a methane emissions reduction of 54.6% and 75.9% is observed at hydrogen blending percentages of 10% and 20% respectively. At a spark angle of 10°BTDC, methane emissions were reduced by 28.3% and 55.9% at hydrogen blends of 10% and 20% respectively. Although the emissions are observed to be higher at 55% load, the trends seem to be the same as the ones observed at a load of 60%.

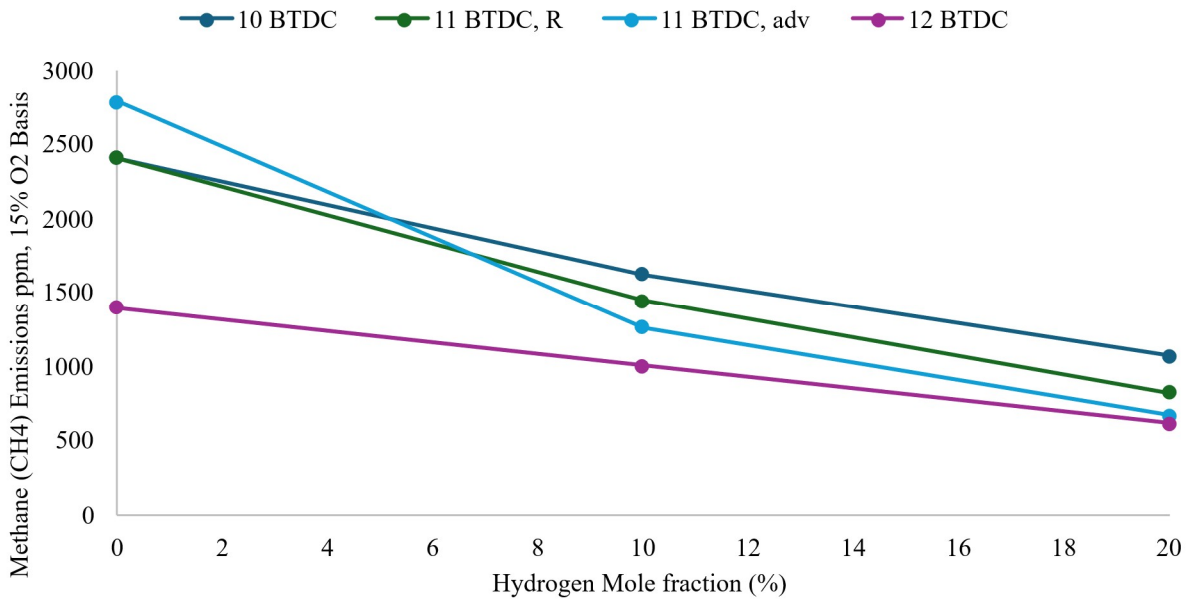

Figure 32: Methane emissions in ppm compared to the hydrogen mole fraction blended across spark timing angles

We can now compare the impact that spark timing has on a lower load by comparing the methane reduction without the addition of hydrogen shown in Figure 33. Retarding the spark timing seems to have no impact on the methane emissions with a difference of 0.04% at a spark timing set of 10°BTDC. Advancing the spark timing to 12°BTDC did see a reduction in methane emissions of 49.9%, which would be considered statistically significant.

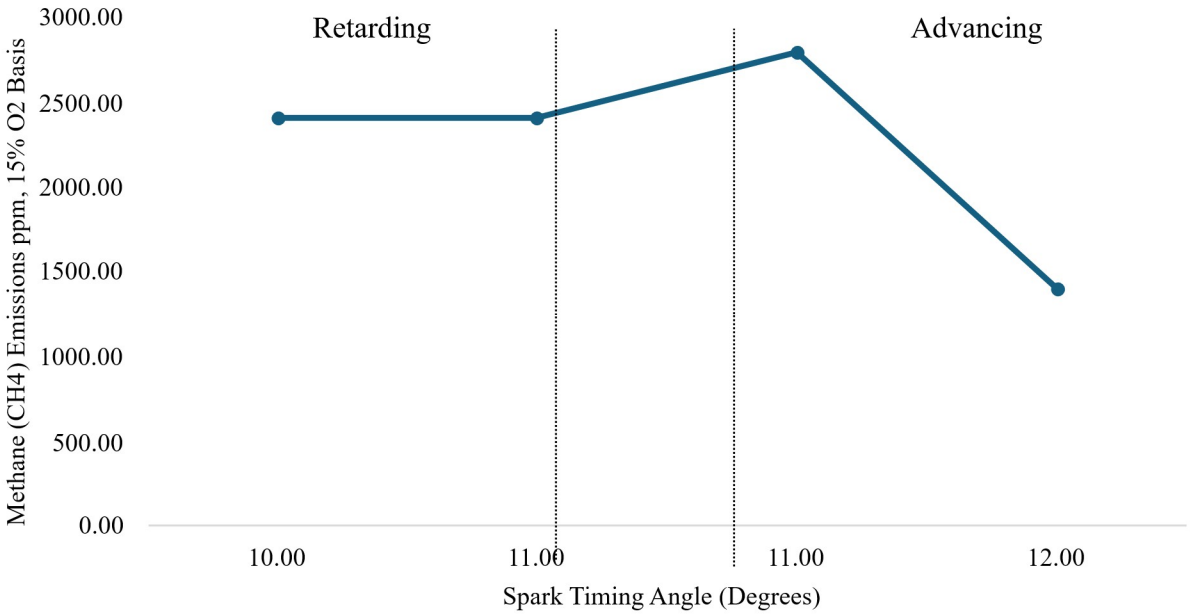

Figure 33: Methane emissions compared to a variety of spark timings when the engine fuel is not blended with hydrogen

The impact that hydrogen blending and spark timing has on methane emissions can be observed by comparing the combination spark timing and hydrogen blending values to the baseline angle with no hydrogen added as shown in Figure 34. Advancing the spark timing to 12°BTDC saw a methane emission reduction of 49.9%, 64%, and 77.9% at a hydrogen blended mole fraction of 0%, 10%, and 20% respectively. Retarding the spark timing saw a reduction of 0%, 32.5%, and 55.6% for hydrogen contents of 0%, 10%, and 20% respectively. These results indicate that hydrogen blending is generally positive, but they are comparing the difference from the baseline with no hydrogen added. If we directly compare the methane emissions from each angle at the same hydrogen content, we can see the distinction between the impact that hydrogen blending has to the system and the spark timing. The advancing dataset at 12°BTDC saw a methane reduction of 49.9%, 20.8%, and 8.3% at a hydrogen blend of 0%, 10%, and 20% respectively.

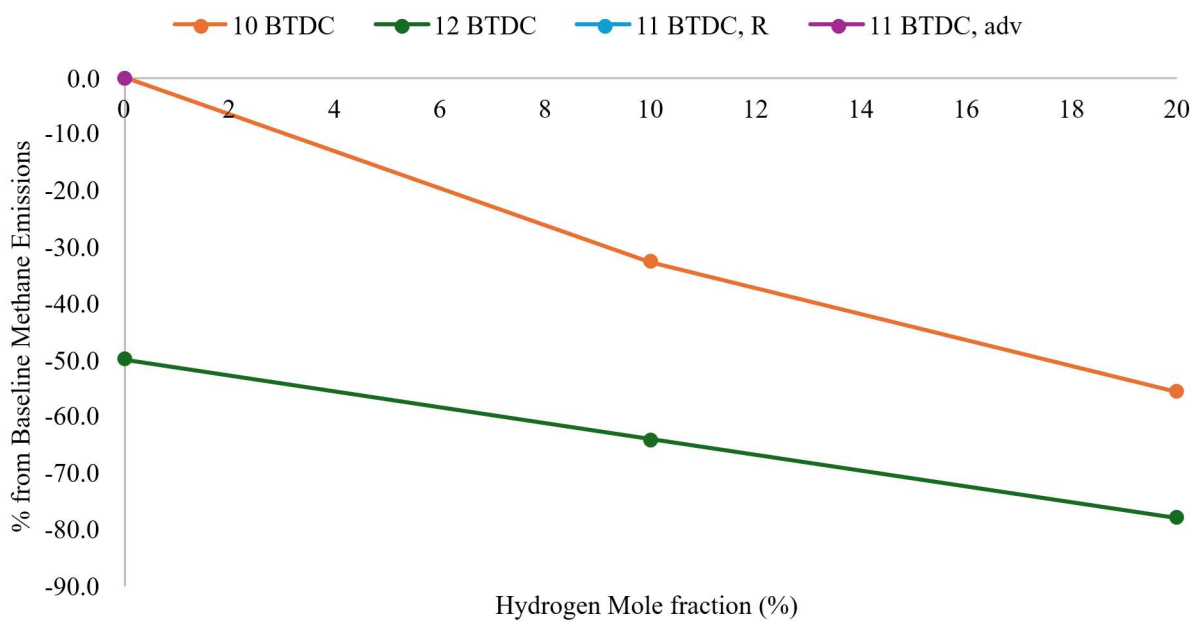

Figure 34: Percent change in methane emissions for advancing and retarding spark times at hydrogen mole fractions of 0%, 10%, and 20% compared to the baseline angle with no hydrogen addition

The difference in methane emissions that the angle change makes becomes less significant when more hydrogen is blended into the system, indicating that the combustion is already being corrected with the addition of hydrogen as shown in Figure 35. A difference of 20.8% and 8.3% is still considered statistically significant, so the modification to the spark timing is still considered to be impactful. The retarding dataset at 10°BTDC when directly compared to the baseline at the same hydrogen content saw an increase in methane emissions of 0.04%, 12.5%, and 29.3% at a hydrogen mole fraction of 0%, 10%, and 20% respectively. This result stems from the drastic benefit that blending hydrogen has to the engine efficiency at the baseline angle of 11°BTDC, with further retarding of the ignition spark hurting the reductions observed from the addition of hydrogen. We will now need to look at the combustion exhaust temperature and operational pressures to further understand what is happening to the engine.

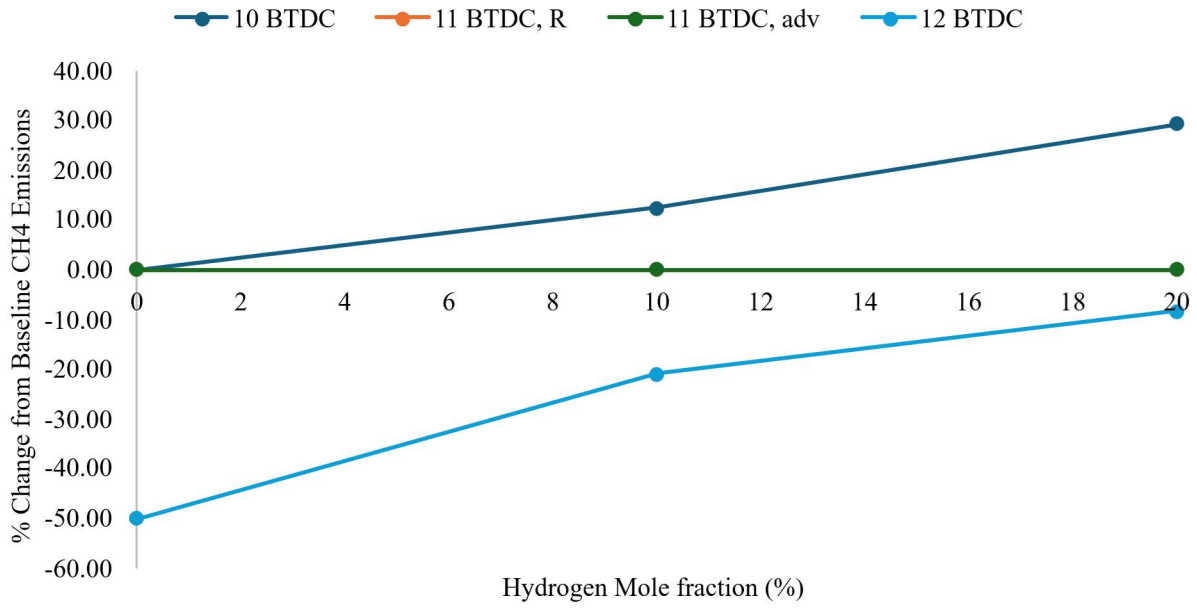

Figure 35: Change in methane emissions compared to the baseline angles across the same hydrogen mole fraction blended into the natural gas stream

4.1.3.2: 55% Load Engine Condition Analysis for Hydrogen Blending and Spark Timing

A lower engine load will result in lower combustion temperatures, with 55% load temperatures shown in Figure 36 being generally lower than the 60% load data. The general temperature trend was the same as 60% load data, with advancing the spark timing increasing the combustion temperature and retarding the spark timing reducing the spark timing. Advancing the spark to 12°BTDC saw a reduction of 4.3°F, 2.8°F, and 6.2°F at hydrogen blending mole fraction of 0%, 10%, and 20% respectively when compared to the 60% load equivalent. Retarding the spark to 10°BTDC saw a temperature reduction of 22.8°F, 8.3°F, and 0.4°F at a hydrogen blending mole fraction of 0%, 10%, and 20% respectively when compared to the 60% load equivalent. The large temperature drop for the retarding dataset reduces the effectiveness of the

combustion reaction, so the addition of hydrogen would increase the energy in the combustion system.

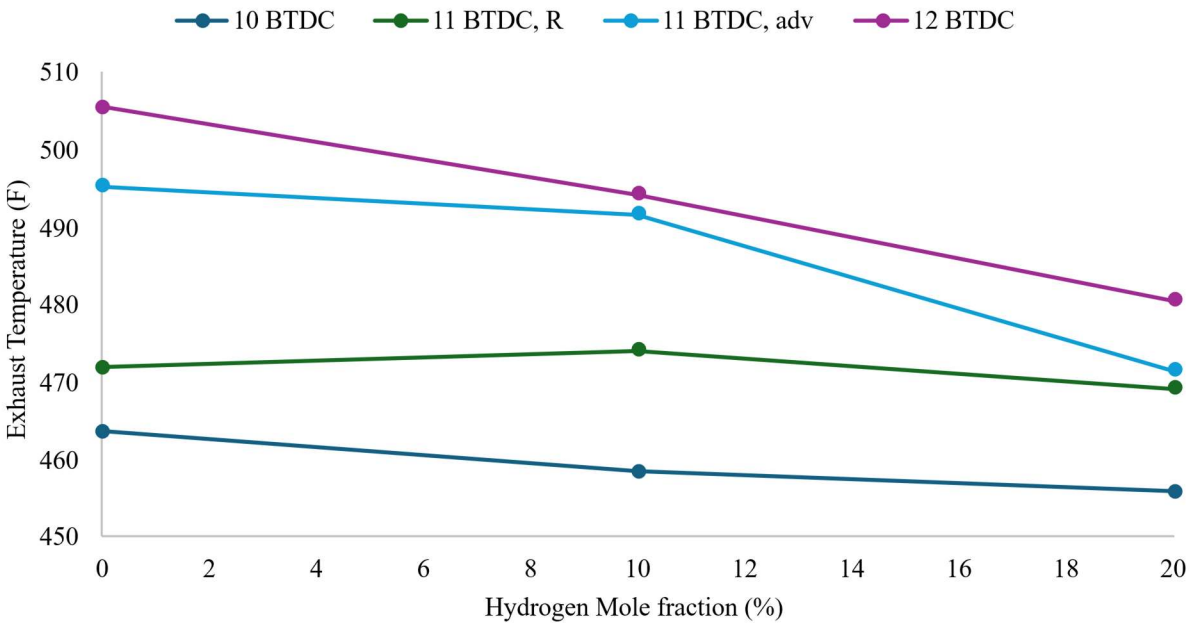

Figure 36: Exhaust temperatures compared to hydrogen mole fraction blends over a range of spark ignition angles

The indicated thermal efficiency for a load of 55% shown in Figure 37 was found to follow the generally hypothesized reduction in thermal efficiency when the spark timing is retarded, with an advanced timing increasing the indicated thermal efficiency. These results not only validate the similar trends observed at 60% load condition, but they are more decisive for the benefit of advancing spark timing.

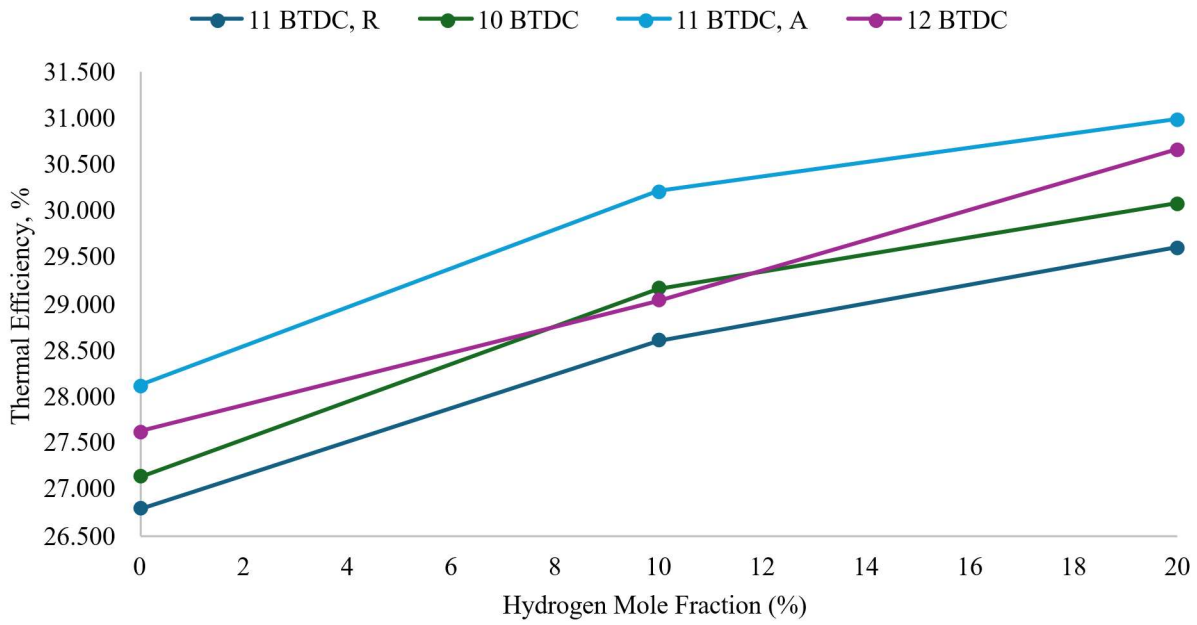

Figure 37: Indicated thermal efficiency compared to the hydrogen mole fraction blend in natural gas over a range of spark timing angles

4.2: PCER Modeling Results

The PCER modeling results will study the impact that temperature, flow rate, and current density have on the concentration along the cell, the reaction rates along the cell, the required operational voltage, and the incurred voltage losses.

4.2.1: Operating Temperature Impact

The change in temperature and inlet concentration has a significant impact on the reaction kinetics within the cell. We will compare the ideal modeling case to the modified emission condition found when the engine is set to an angle of 11.5°BTDC and blended with 20 H_2%. The exit mole fraction of each compound at different temperatures is shown in Figure 38. The methane is found to be fully converted when the cell operates above 865K. The CO_2 at that temperature reaches its production peak while keeping CO to a minimum. This relationship

between CH_4, CO, and CO_2 would indicate that the cell should not be run higher than around 873.15K (600°C) to avoid any backward reactions. The reaction rates for water gas shift, steam methane reforming, and methane oxidation have been graphed to verify the mole fraction trends. The steam methane reforming reaction in Figure 39 shows the reaction rate at each step along the length of the cell. Steam methane reforming is seen being the most active at the entrance of the cell where the methane concentration is high. As the gases move along the cell, the methane is converted and the reaction rate drops. We can see that after 865K, the reaction rate halfway along the cell, R_SR[5], changes trajectory and begins to drop. A trend is observed where the lower the temperature of the cell, the switch point happens later in the cell. This makes sense, with lower temperatures requiring more catalytic material to convert the methane to the same quantity as increasing the temperature.

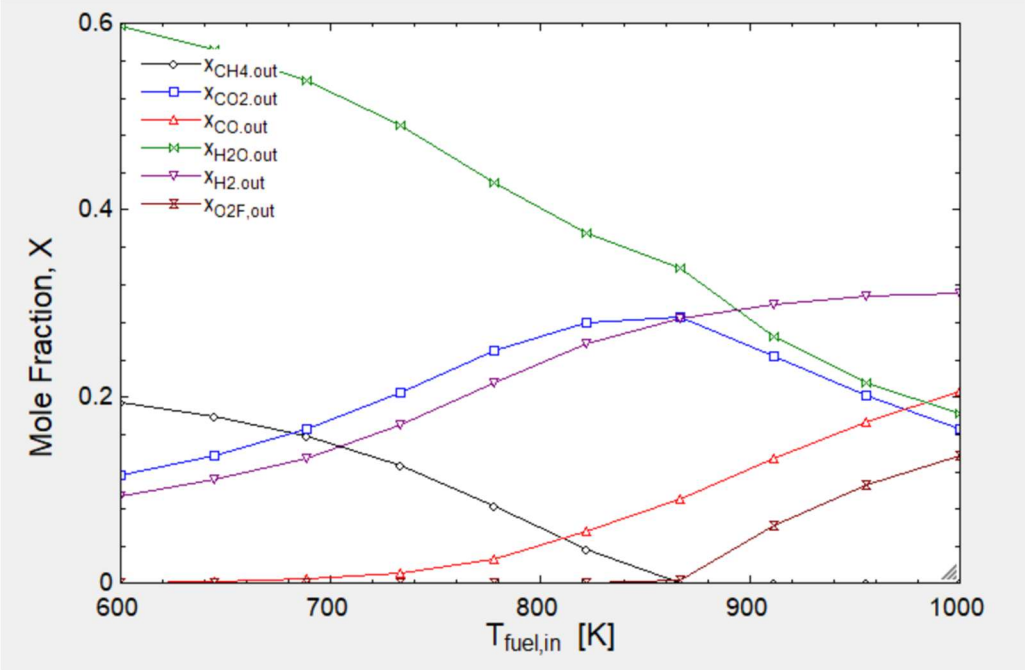

Figure 38: Exit emissions from PCER unit at different temperatures utilizing ideal emissions

A similar trend is observed for the water gas shift reaction shown in Figure 40, with a reduction in temperature increasing the length step at which the reaction reaches its peak and begins to become less effective. A noticeable trend for both steam methane reforming and water gas shift is that the reaction is far more active at the start of the reaction, but the final step begins to promote a backward reaction. The higher the operating temperatures, the more prominent the backwards reactions become. This relationship makes sense, with the methane becoming exhausted more quickly while the non-diffused hydrogen and water allow for reverse steam methane reforming and water gas shift.

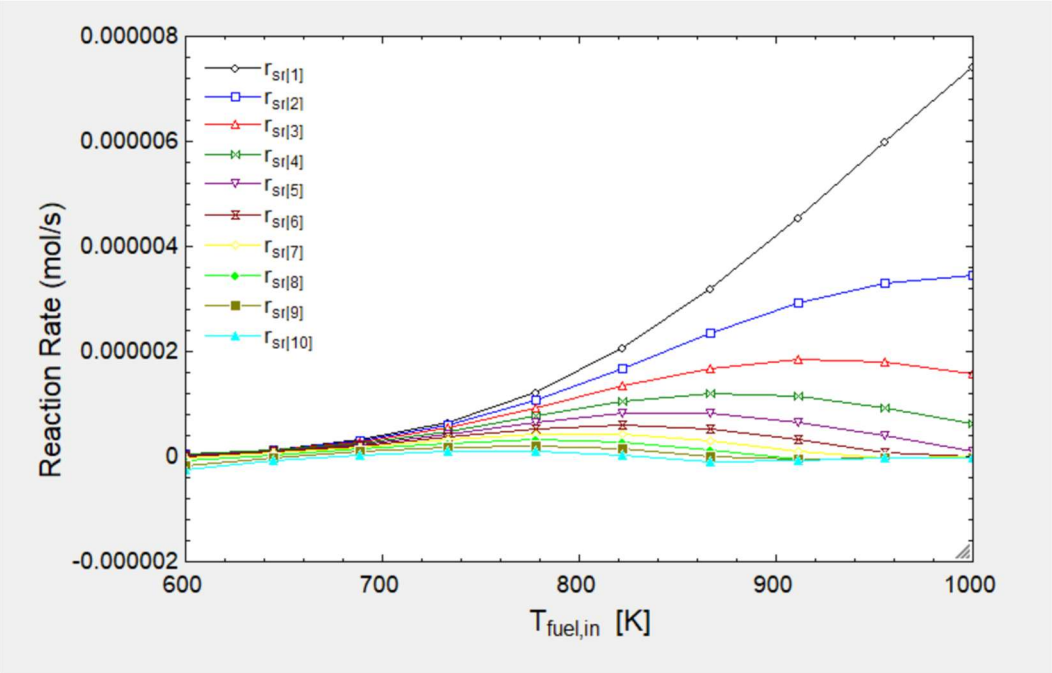

Figure 39: Rate of steam methane reforming along the length of the cell at different temperatures

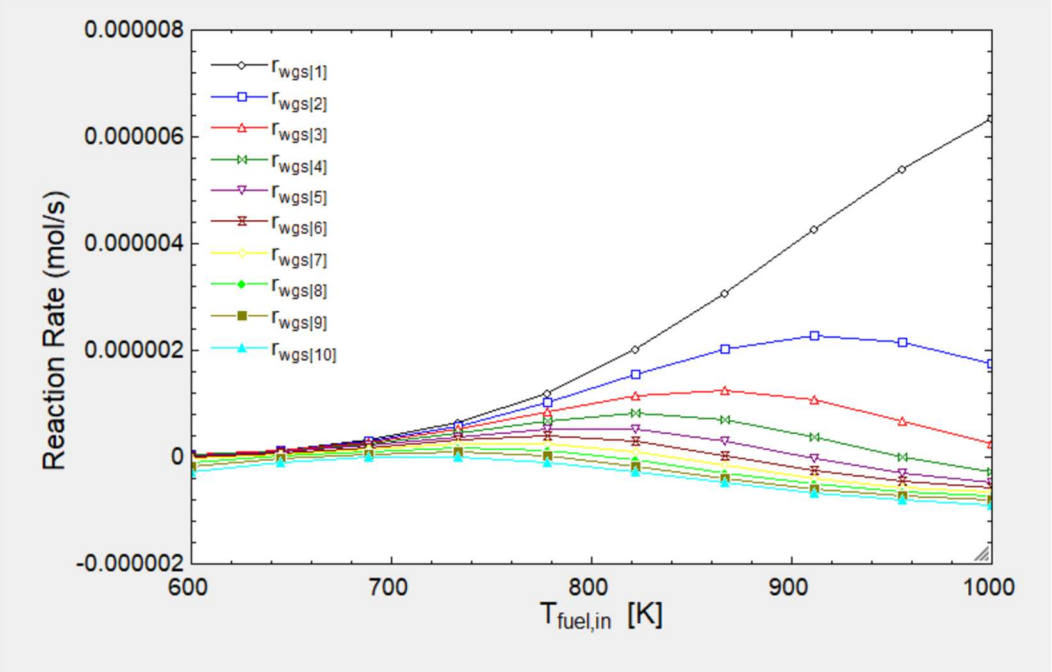

Figure 40: Rate of water gas shift reaction along the length of the cell at different temperatures

Methane oxidation is dependent on methane and oxygen being present in the system. We can see that the reaction rate for methane oxidation in Figure 41 is fairly consistent until 900K is reached, at which point the last steps of the reaction go to almost zero. This trend can be explained with complete conversion of methane happening within a short length of the cell when the PCER is operating at high temperatures. This trend can be confirmed with a sudden rise in oxygen after 900K in Figure 41, reflecting the deactivation of the methane oxidation reaction. From these results we can conclude that the optimal operational temperature is 850K with a range of 800-900K being acceptable.

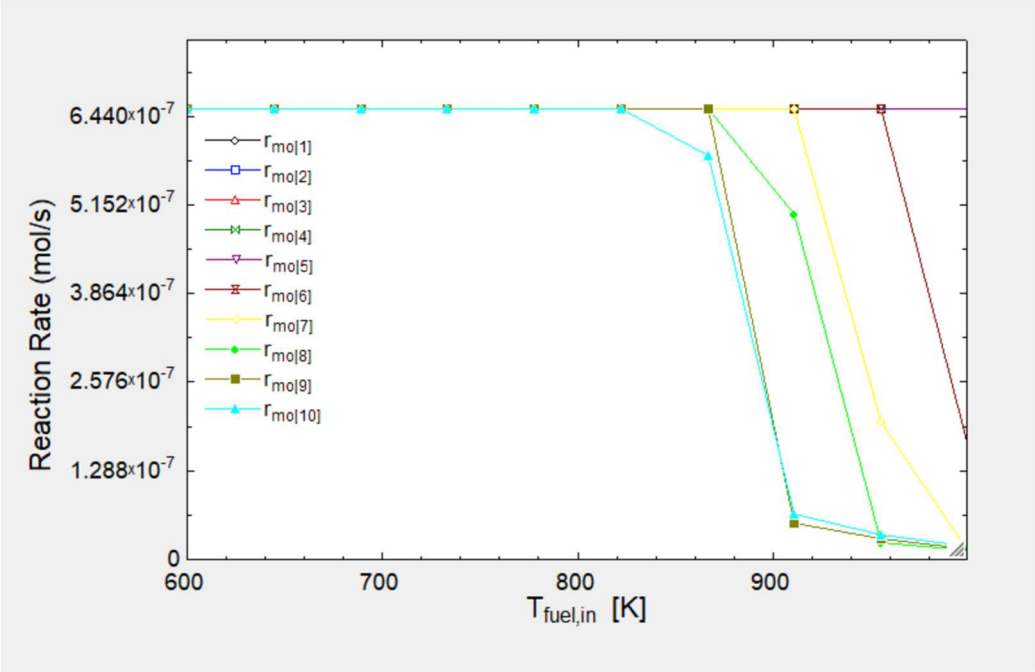

Figure 41: Rate of methane oxidation along the length of the cell at different temperatures

We will now look at the real-world modified engine emissions to obtain some optimized conditions for a PCER unit. Figure 42 shows the exiting mole fraction from the PCER unit at different temperatures. We can see that, due to the methane mole fraction being 0.081, electrolysis becomes the dominant reaction and the oxygen and hydrogen concentrations level out at around 0.50 and 0.15 respectively. This is further shown with the high-water uptake before below 773K. Looking at the CO and CO_2 mole fractions in Figure 43, we can see that the CO and CO_2 mole fractions begin to switch trends as early as 650K, with the mole fraction of CO becoming higher than CO_2 after 950K. This trend would indicate that the WGS, SMR, and MO reactions may be going backwards instead of becoming non-active. To validate this claim, we will now study each reaction rate at a range of temperatures.

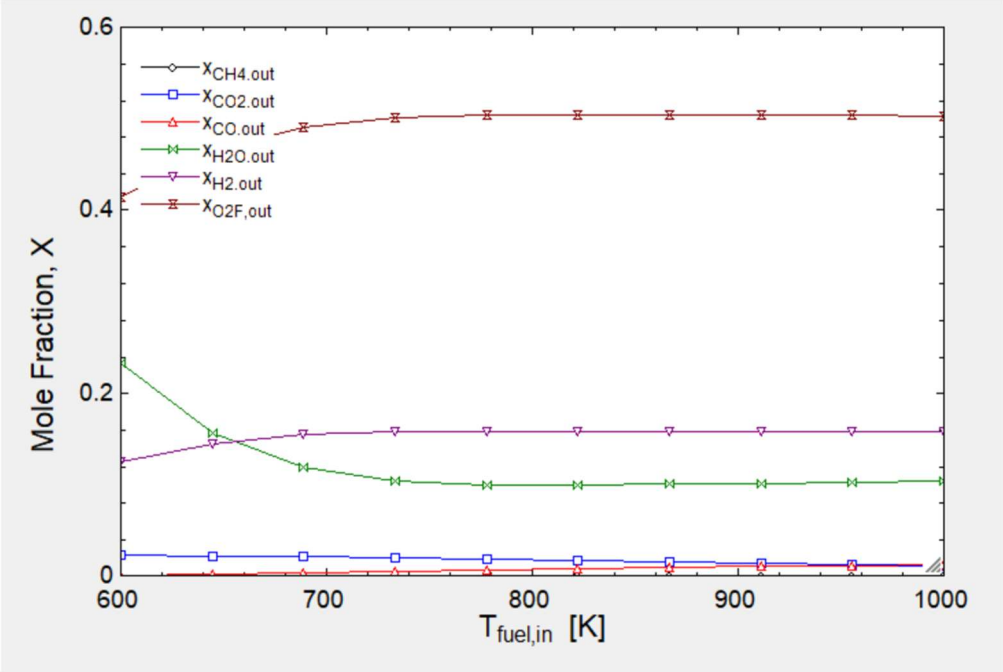

Figure 42: Exit emissions from PCER unit at different temperatures utilizing real modified emissions

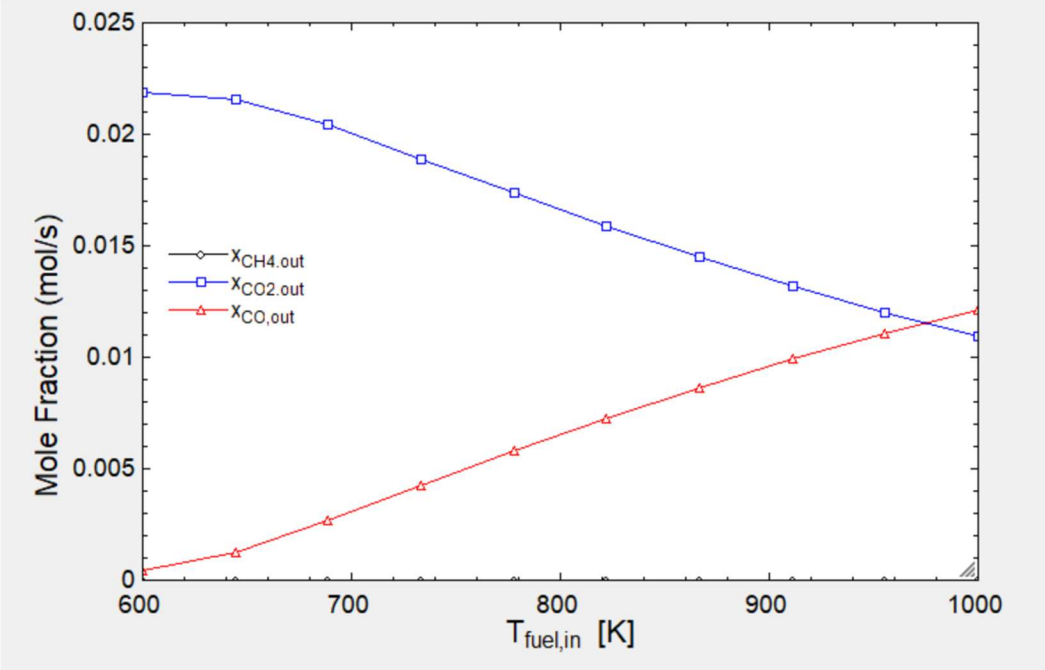

Figure 43: Exit emissions from PCER unit at different temperatures utilizing real modified emissions, CO2 and CO enhancement

Steam methane reforming in Figure 44 and water gas shift in Figure 45 are observed to be negative along the entire length of the PCER at all temperature ranges. This trend is due to the high oxygen content allowing methane oxidation in Figure 46 to utilize all of the available methane. This explains the negative WGS and SMR reaction rates. Methane oxidation becomes more active closer to the end of the cell, which is occurring because of the increase in oxygen concentration further along the cell length. This trend also explains why the WGS and SMR reactions get more active backward reactions further in the length of the cell.

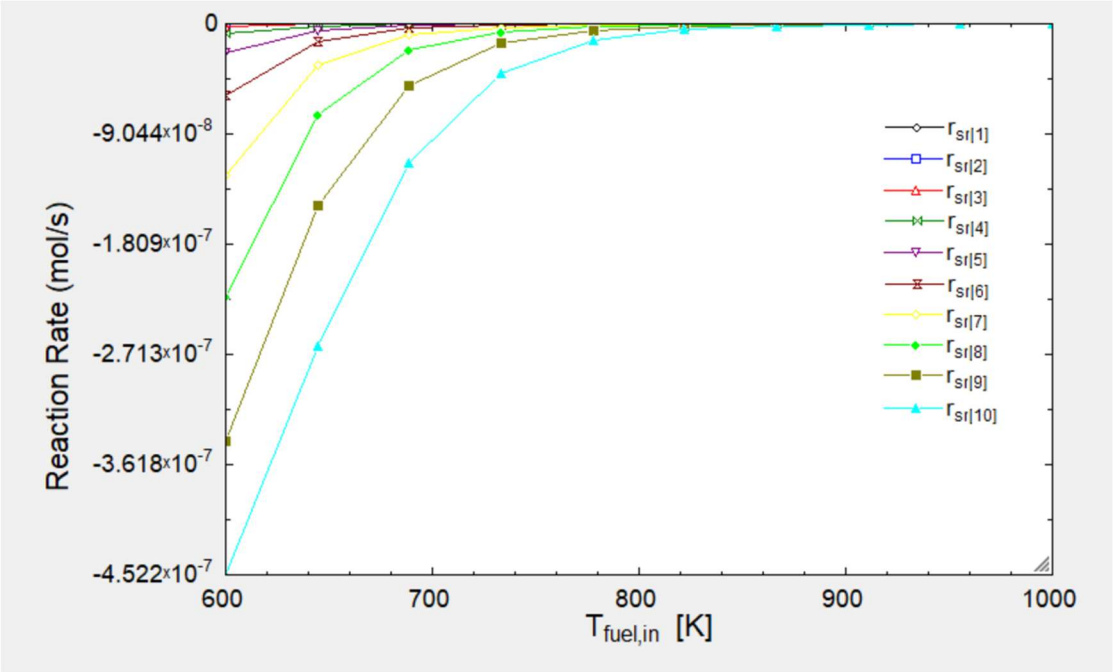

Figure 44: Rate of steam methane reforming along the length of the cell at different temperatures

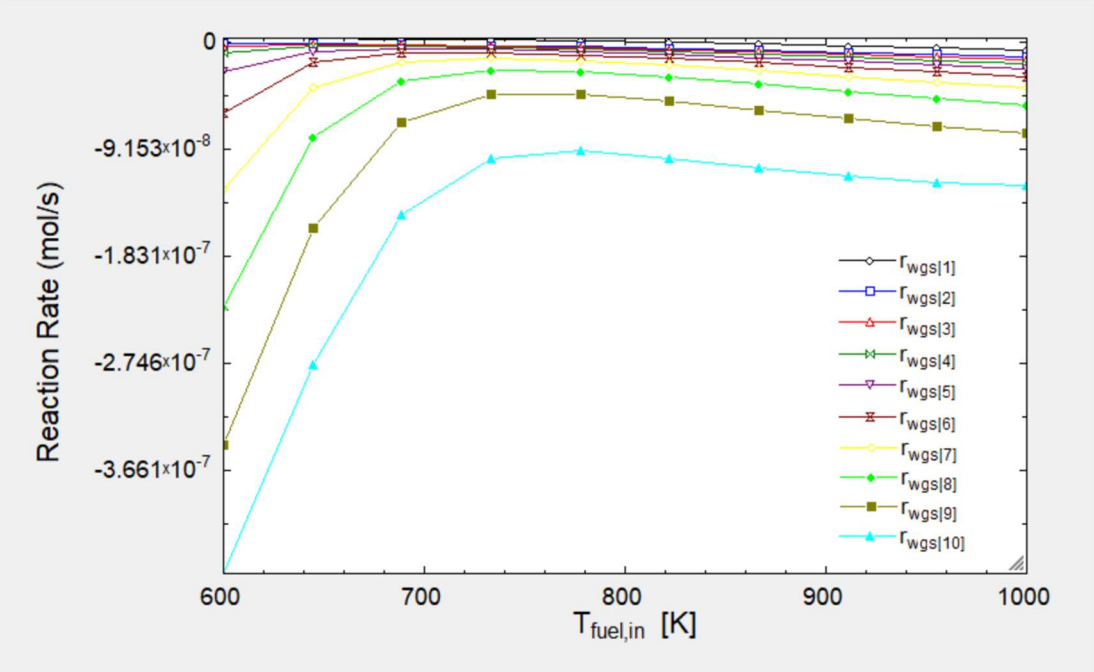

Figure 45: Rate of water gas shift reaction along the length of the cell at different temperatures

As the temperature increases above 800K, steam methane reforming becomes inactive. This is due to the lack of methane and a lack of water in the system to allow for the reaction to go backwards. Water gas shift on the other hand switches at 720K, slightly rising in activity at higher temperatures. At low temperatures, reverse water gas shift (RWGS) becomes more active, producing small amounts of water and CO and utilizing some of the hydrogen produced from electrolysis and the CO_2 produced from the methane oxidation reaction. Although high temperatures make methane oxidation less active further along the cell, the methane oxidation reaction stays consistent at all of the studied temperatures at the entry of the cell. This can be explained by the available methane at the entrance being the limiting reactant. These results indicate that an operating temperature of 720K and a range of 700-800K would minimize the RWGS and SMR reactions while keeping an optimum production of hydrogen.

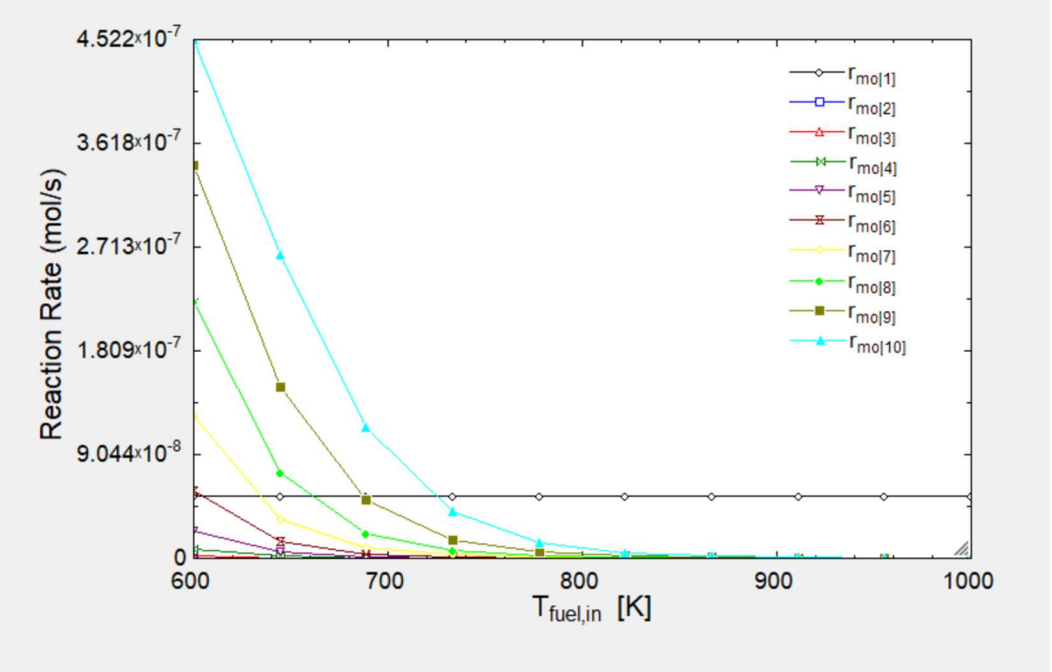

Figure 46: Rate of methane oxidation along the length of the cell at different temperatures

The ideal emissions obtained an ideal temperature of 850K while the real-world modified emissions obtained an ideal temperature 720K. Although the real-world case had 40% water added to the system, the methane emissions indicate that a small amount of methane may aid in the catalytic reactions to avoid reverse reactions. Although the ideal PCER inlet methane mole fraction of 25% may be too high, we will look at the impact that adding 5% mole fraction of methane to the modified stream has to the reaction rates and mole fractions.

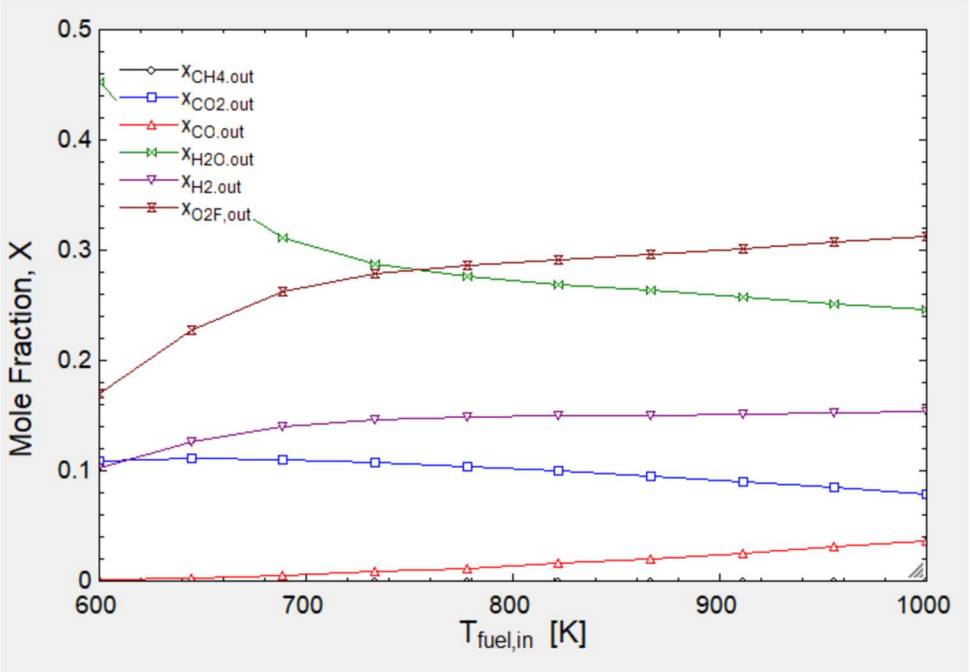

Figure 47: Temp vs. mole fraction for the modified exhaust emissions with 5% methane added

We can see from Figure 47 that, although the methane is immediately converted at all temperatures, the various mole fractions are changing far more than without the added 5% methane. The reactions in Figure 48 show the full story, with the notable exception for methane oxidation at the first cell length step because it is a constant and much larger than all of the reactions shown. We can see that the WGS and SMR reactions are positive at the entrance and then become negative further along the length of the cell. Higher temperatures reduce the strength of the reverse reactions, with the exiting reactions for water gas shift and methane oxidation going to 0 mol/s. The exiting water gas shift reaction is the only reaction that continues to become negative at higher temperatures, but this trend is also observed in the ideal case to a smaller scale. The ideal operating case using the 11.5BTDC and 20% H_2 blend engine emissions with 5% methane added is between 720-770K.

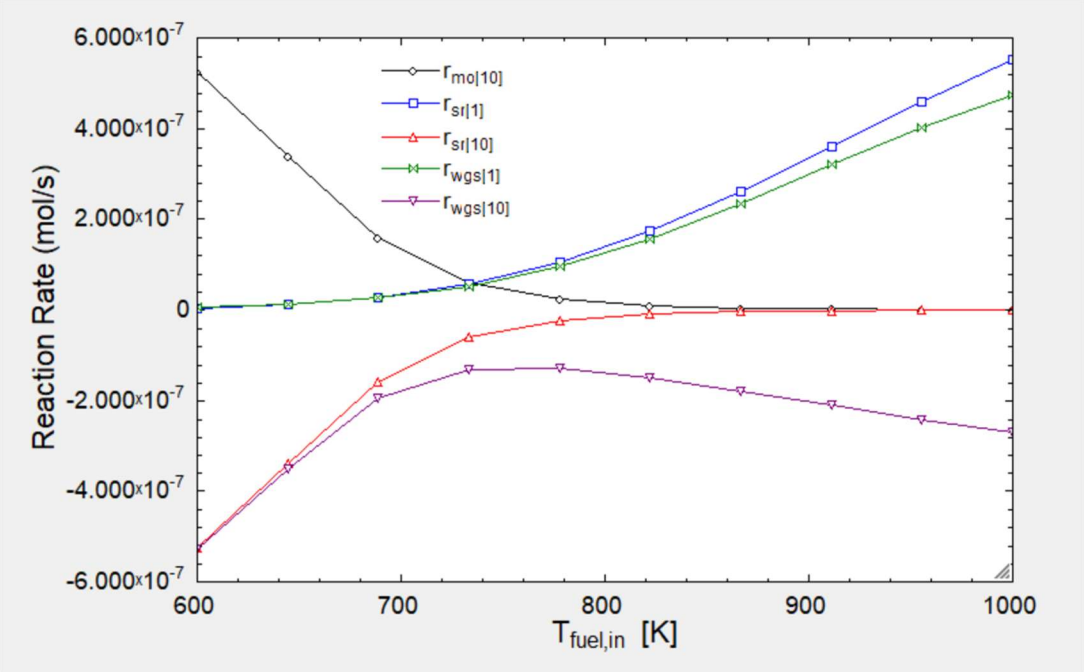

Figure 48: Temp vs. reaction rates for the modified exhaust emissions with 5% methane added

4.2.2: PCER Flowrate Impact

The flow rate for the PCER in this thesis is utilizing catalyst grams per second as the flow rate and is modified through the GHSV value. A higher flow rate reduces the amount of time that the gases have to interact with the catalyst, so the reaction rates will be lower at higher flow rates. In this section we will be studying the impact that flow rate has to the performance of the PCER cell. The temperature is kept at 750K, the current density is set to 2,000 A/m^2, and the geometry is kept constant. The ideal inlet composition and the real engine emissions from an advanced spark timing and hydrogen blend (5 mol% of methane and 40% water added) will both be used for testing. Figure 49 Shows that the electrolysis reaction becomes far less active from $1*10^6$ to $2*10^6$ h^{-1}, with almost no methane conversion or electrolysis occurring after $6*10^6$ h^{-1}. This would indicate that a slower flow rate is necessary for the cell to convert methane. Due to

the high flow rates from the natural gas compressor, the flow rate needs to be kept relatively high so as to not require as many PCER cells in a stack configuration.

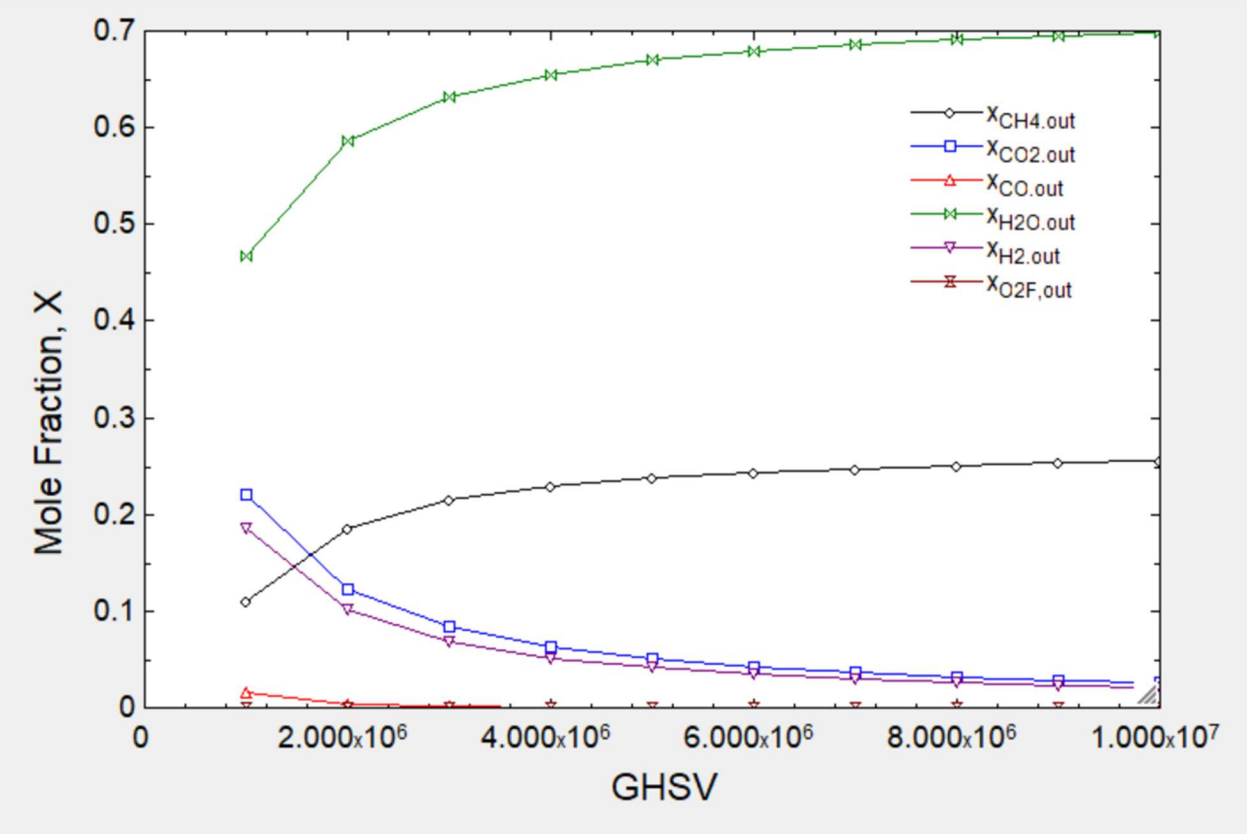

Figure 49: GHSV vs. mole fraction from an ideal feed concentration

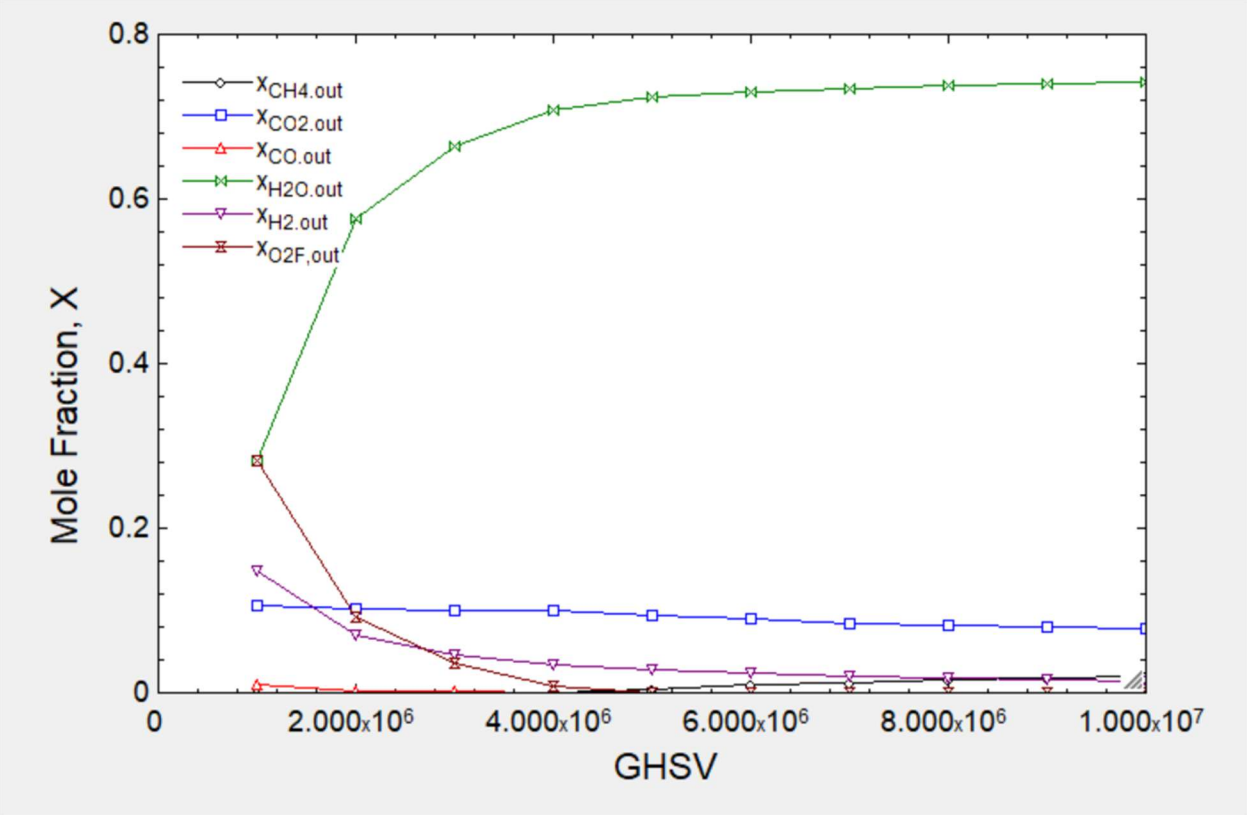

Figure 50: GHSV vs. mole fraction using the modified engine emissions from the engine settings 11.5BTDC with 20% hydrogen addition. 5% methane and 40% water were added for model convergence purposes.

The modified emission case is tested in Figure 50 and Figure 51, with even the 5.08% methane in the stream not being completely converted after $5*10^6$ h^{-1}. Electrolysis with the modified emissions are shown as inactive in Figure 51, with oxygen reaching a mole fraction of 0.000085 after $4*10^6$ h^{-1}. The produced hydrogen in the modified emission case comes from steam methane reforming, with CO_2 still being present in the steam in similar quantities to H_2. These results that a GHSV of 1,000,000 or lower is necessary for the cell to function effectively. Due to modeling limitations, this model does not work well with very low flow rates. This is due to the water and methane going to a mole fraction of 0 within the first step, limiting the convergence of the electrochemical and reaction equations.

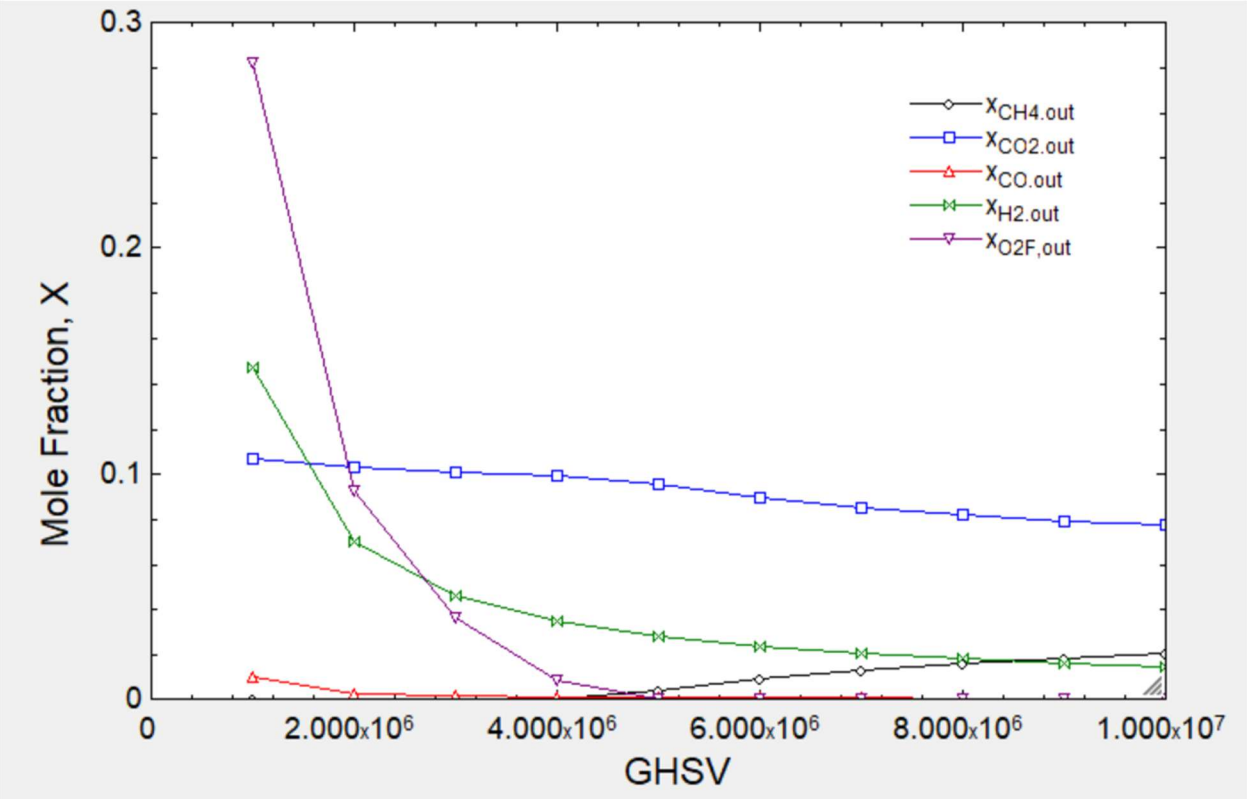

Figure 51: Zoomed in GHSV vs. mole fraction using the modified engine emissions from the engine settings 11.5BTDC with 20% hydrogen addition. 5% methane and 40% water were added for model convergence purposes.

4.2.3: PCER Electrochemical Model

Protonic ceramic electrochemical reactors require an input of electricity to operate. When sourced with electricity, the cell will experience losses due to the material, the chemical makeup of the inlet gas, and the activation barrier for the catalyst to start working. In this section we will study the impact that current density and temperature have on the cell when fueled with an ideal 3:1 water-to-methane ratio and the ideal tuning conditions from the real-world emissions with 5% methane and 40% water mixed into the exhaust stream. The temperature testing utilizes a current density of 2,000 A/m^2 and a GHSV of 1,000,000. The current density is tested for 673K, 873K, and 1000K to gain a deeper understanding of the electrochemical systems at key temperature ranges. We will first investigate the electrochemical operation across a range of

temperatures for both inlet emission conditions and then look more specifically at a range of current densities.

4.2.3.1: Electrochemical Operation at Different Operating Temperatures

The ideal emissions sustain a functional voltage range for the cell in Figure 52, with the operating voltage never dropping below the Nernst voltage. The lowest required voltage for this condition is found at 873K, with a sudden jump after this identified temperature. To understand what is happening, the voltage losses are graphed in Figure 53. The concentration losses make up a majority of the cell losses. The concentration losses spike at 780K, but the Nernst voltage also drops at this condition. This indicates that the water at the anode surface drops while the hydrogen production increases. The oxygen partial pressure is very low at this condition because of methane oxidation utilizing the produced oxygen from electrolysis.

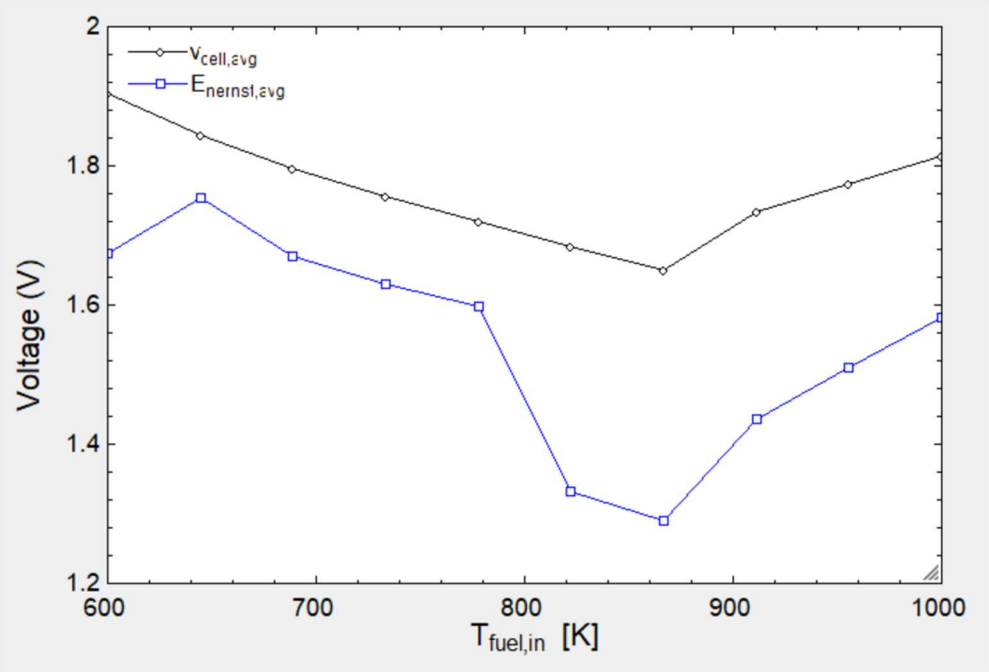

Figure 52: Temperature vs. operating voltage for an ideal inlet stream at 2,000 a/m²

With this knowledge, we know that the concentration losses at the cathode increase after 873 due to the complete conversion of methane and the sudden rise in oxygen concentration in the system. The increase in oxygen reduces the active sites for hydrogen diffusion, increasing the concentration losses.

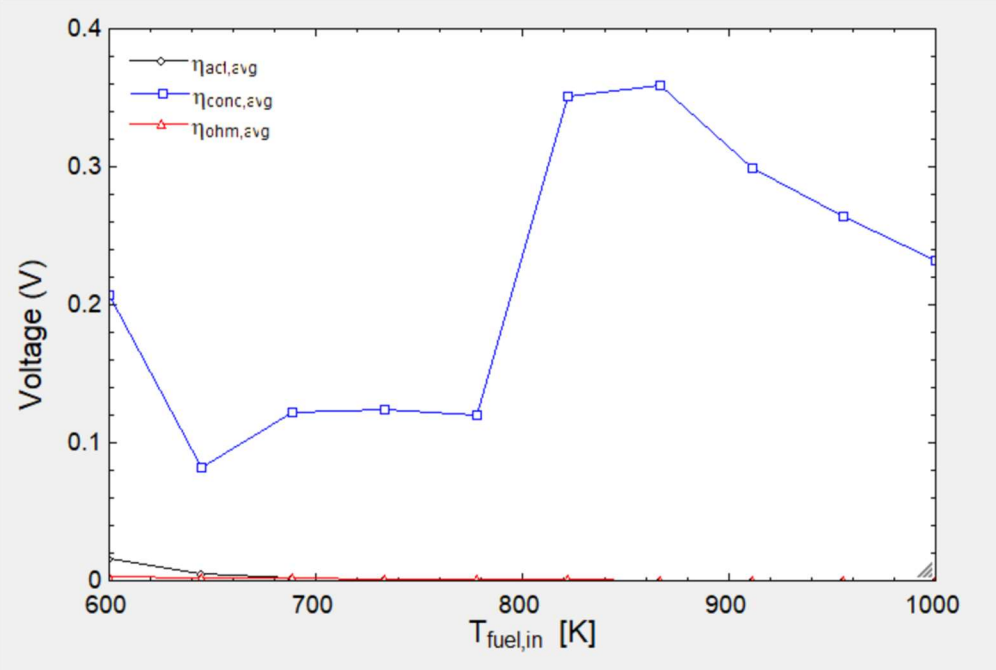

Figure 53: Temperature vs. voltage losses for an ideal inlet stream at 2,000 a/m2

We will now shift our focus to the modified engine emission condition. In Figure 54 we can see that the cell operating voltage is still higher than the Nernst voltage, indicating that the cell can still operate as an electrolyzer with the smaller methane content when the cell is operating at 2,000 A/m^2. The concentration losses in Figure 55 make up a majority of the losses in the PCER cell. A spike at 783K is observed due to the oxygen concentration becoming larger than the water concentration. The activation losses and ohmic losses are present at 600K and become negligible after 800K. These results indicate that the lack of methane allows the methane oxidation reaction to become deactivated at a much lower temperature in the case of the modified emission being used as the PCER feed. These results for both the ideal and the

modified feed gases indicate that the ideal operating temperatures are between 773K and 873K for the case that the current density is operating at 2,000 A/m^2. The target temperature for the PCER unit is between 600-773K (350-500°C), so either the current density needs to be changed or the flow rate can be increased to speed up the methane oxidation reaction, but the temperature would need to be low enough as to reduce the change for RWGS and RSMR to occur. We will now shift our focus to the current density to understand how the current impacts the operational voltage and chemical conversion. In order to study both the impact of temperature and current density, the cell temperature will be set at 673, 873, and 1000K for each test.

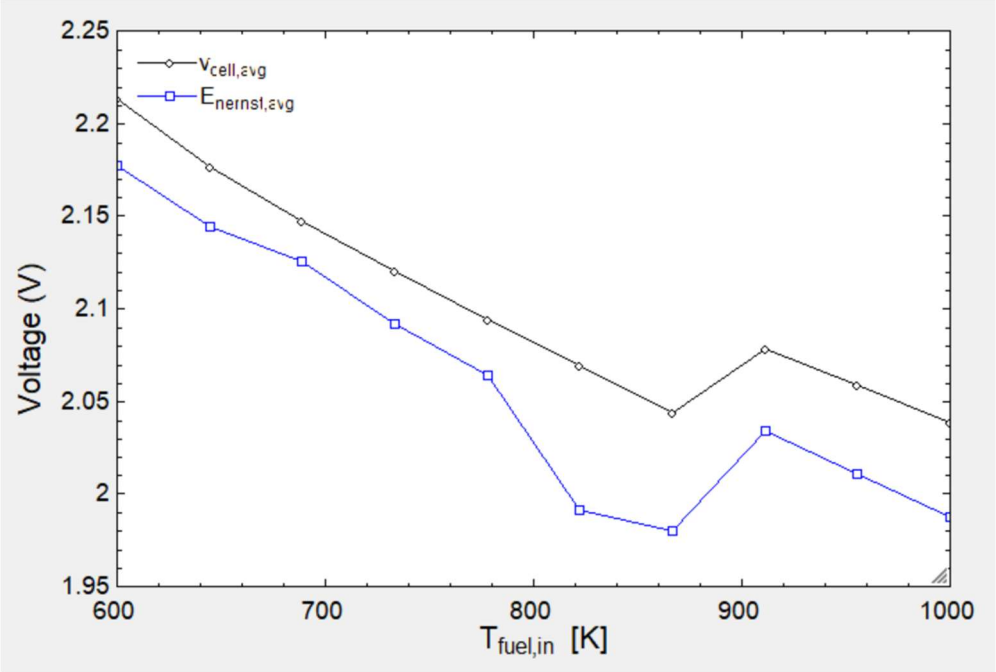

Figure 54: Temperature vs. operating voltage for a modified real inlet stream at 2,000 a/m2

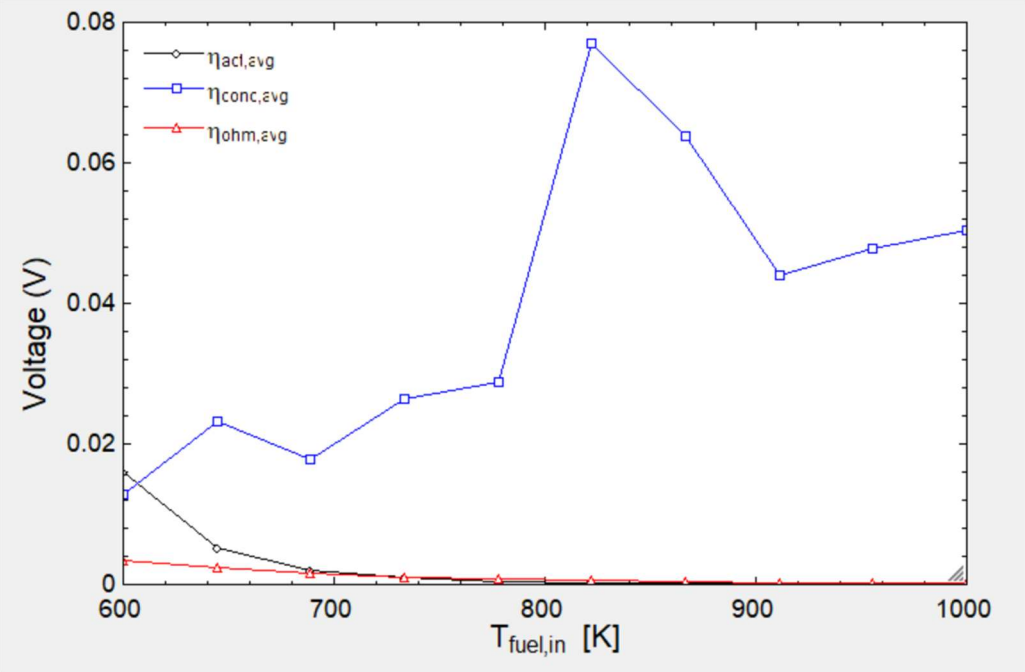

Figure 55: Temperature vs. voltage losses for a modified real inlet stream at 2,000 a/m2

4.2.3.2: Ideal Feedstock Electrochemical Operation at Different Current Densities

The current density reflects the speed at which electrolysis will occur within the cell. Higher current densities allow for the PCER unit to produce more hydrogen, but it also increases the amount of oxygen and hydrogen in the cell, reducing the water concentration at the cathode. We will now compare the impact that the ideal feed composition has at different current densities for each temperature rating.

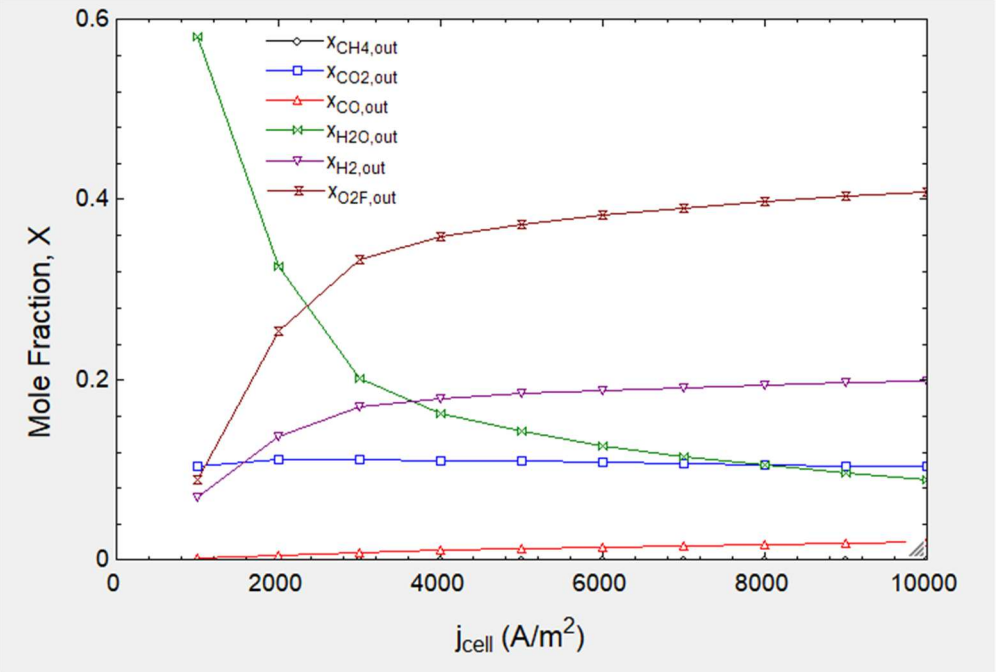

Figure 56: Current density vs. mole fraction for an ideal feed stream at 673K

At 673K we can see in Figure 56 that the water is the primary limiting reactant, with the concentration dropping rapidly from 1000 A/m^2 to 3,000 A/m^2 before reaching a more consistent trend with the other reactants in the stream. The concentration losses in Figure 59 reflect this drop, with the ohmic and activation overpotential losses becoming larger than the concentration losses between 4,000 A/m^2 and 5000 A/m^2. Due to the hydrogen evolution reaction becoming the dominant reaction after 3,000 A/m^2, the conversion of methane from methane oxidation becomes less impactful to the system with the more abundant oxygen content from the HER reaction. We can see that a small quantity of CO is being produced as the current density is increased while the CO decreases very slightly, indicating the occurrence of a backwards reaction. The reactions in Figure 58 indicate that as the current density is increased, the methane oxidation reaction increases while reverse steam methane reforming becomes more powerful. As previously discussed, the increase in oxygen in the system from the HER reaction allows for the methane oxidation reaction to become stronger. Due to the increased concentration of hydrogen in the

system while sustaining water, the stream methane reforming reaction can become more active at lower temperatures than previously observed. This observed reverse steam methane reforming reaction may limit the optimal current density for the cell, with the methane oxidation reaction needing to intake more of the produced oxygen to stop the chance of methane being produced from the cell. This observation will need to be further studied in the modified case.

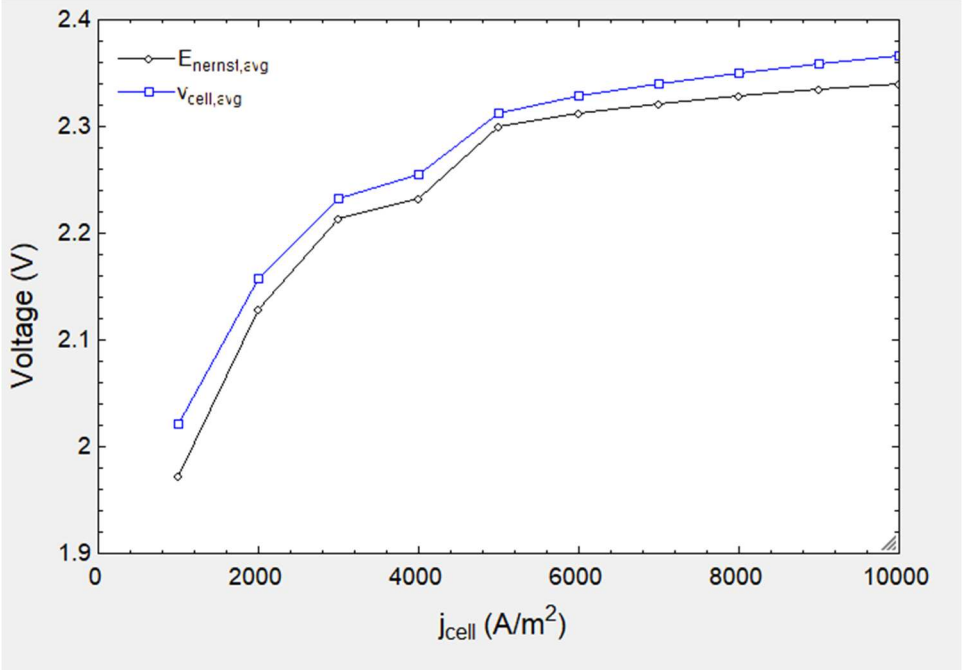

Figure 57: Current density vs. operating voltage for an ideal feed stream at 673K

The operational voltage is always higher than the Nernst voltage, indicating that the cell can operate as an electrolyzer even at high current densities. The losses are also minimal when compared to the Nernst voltage, indicating that, for an ideal gas feed stream, the lower operational temperature with a higher current density may be the ideal operational condition. This may not be the case for the low methane case found in the modified reaction emission situation.

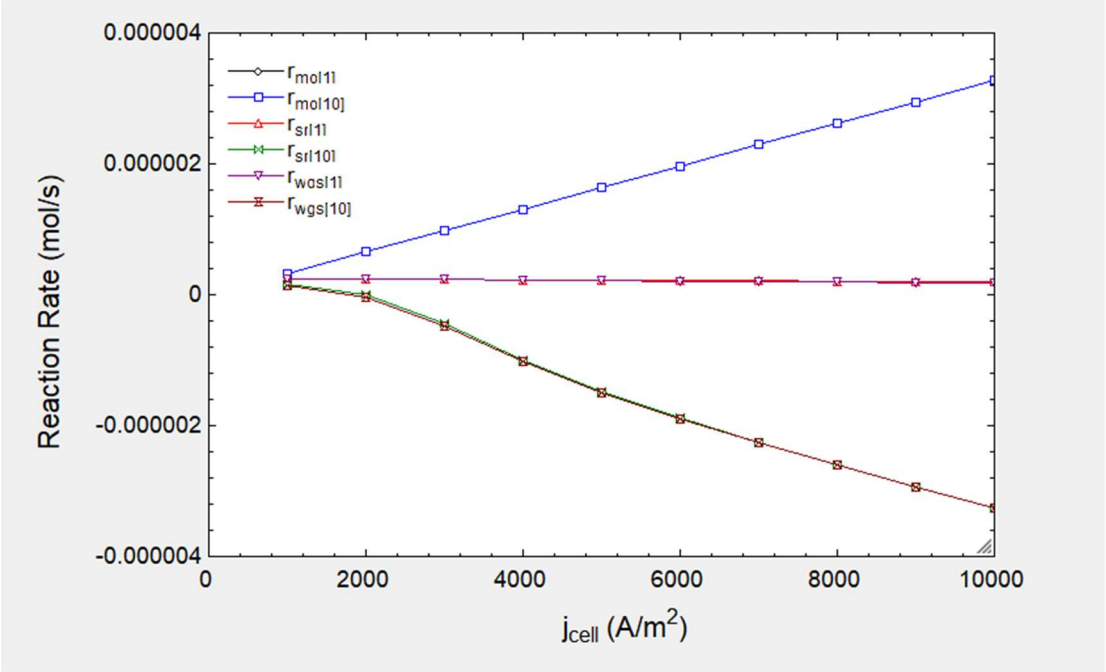

Figure 58: Current density vs. reaction rates for an ideal gas feed at 673K

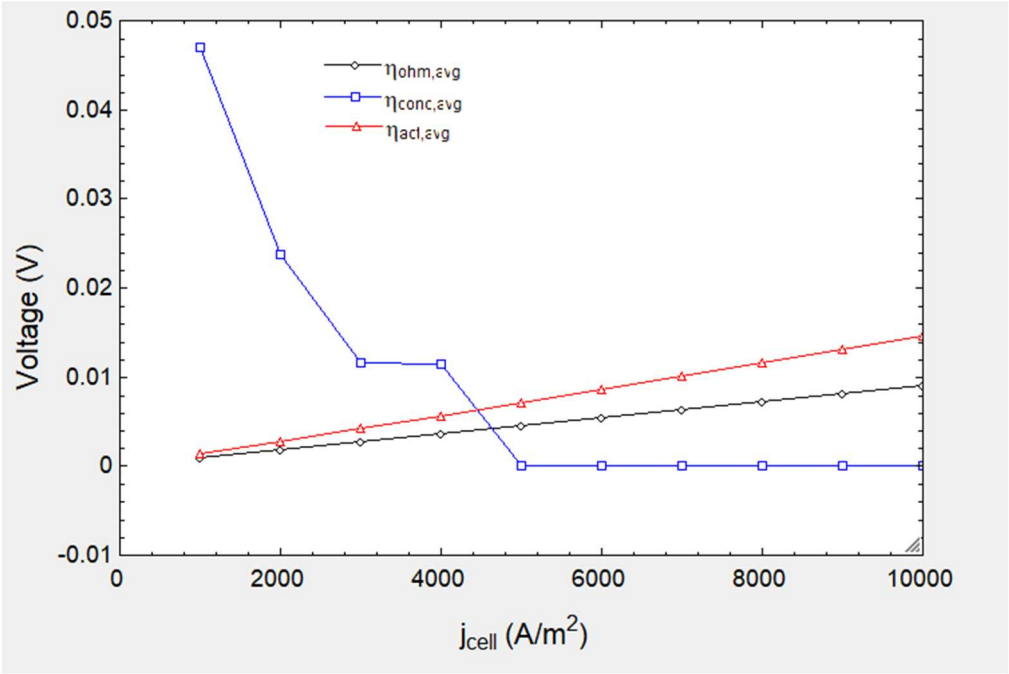

Figure 59: Current density vs. voltage losses for an ideal feed stream at 673K

We will not look at the current density results for the ideal case at 873K. Figure 60 shows a complete utilization of water after 6,000 A/m^2, indicating a potential limitation for cell operation when the cell is operating at 873K. The reaction rates in Figure 61 indicate that the

reverse water gas shift reaction and the methane oxidation reactions are relatively similar until the cell reaches a current density higher than 4000 A/m^2, at which point the RWGS reaction becomes much more active as the current density is increased. This trend is validated in Figure 60 with CO overtaking CO_2 at 4,000 A/m^2 and the hydrogen concentration dropping after 5,000 A/m^2.

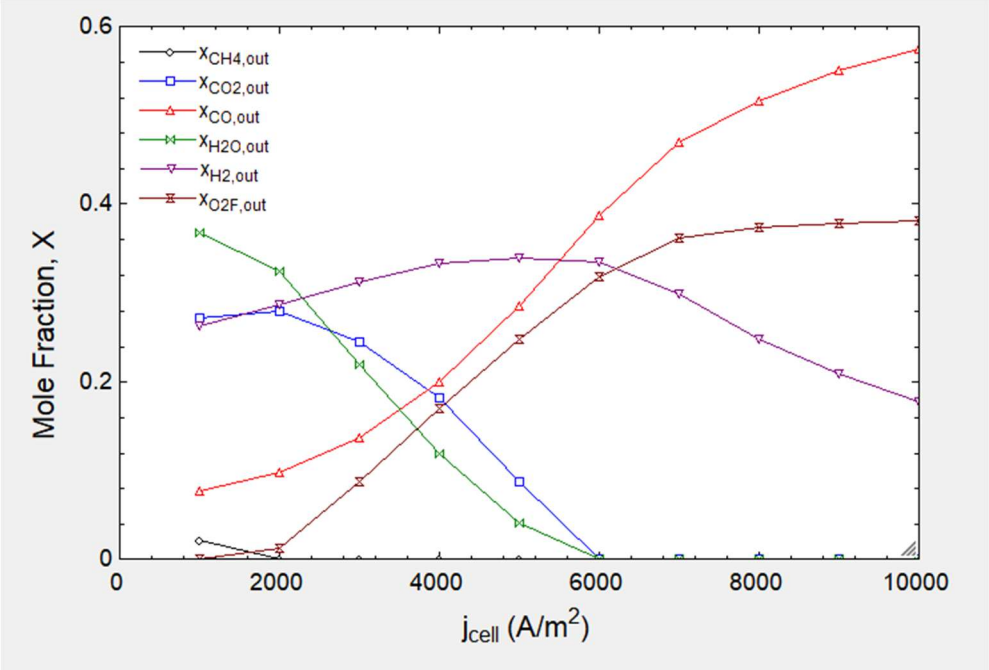

Figure 60: Current density vs. mole fraction for an ideal feed stream at 873K

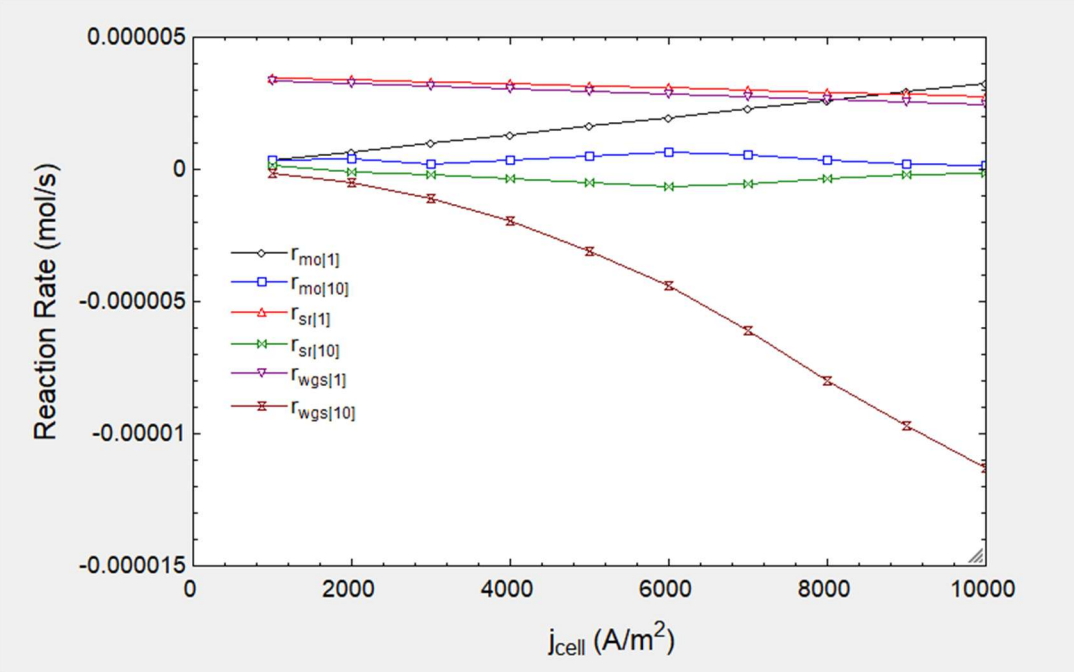

Figure 61: Current density vs. reaction rates for an ideal gas feed at 873K

The operating voltage and the voltage losses in Figure 62 and Figure 63 indicate that the cell cannot operate as an electrolyzer after 7,000 A/m^2, with the operating voltage dropping below the Nernst voltage. This is due to the production of water and CO from the RWGS reaction instead of using the water for the production of oxygen and hydrogen, making the anode partial pressure negative. In the case that the cell is operating at 873K, The PCER unit an only operate so long as water is available in the system. Because of this, the PCER cannot operate at a current density higher than 6,000 A/m^2.

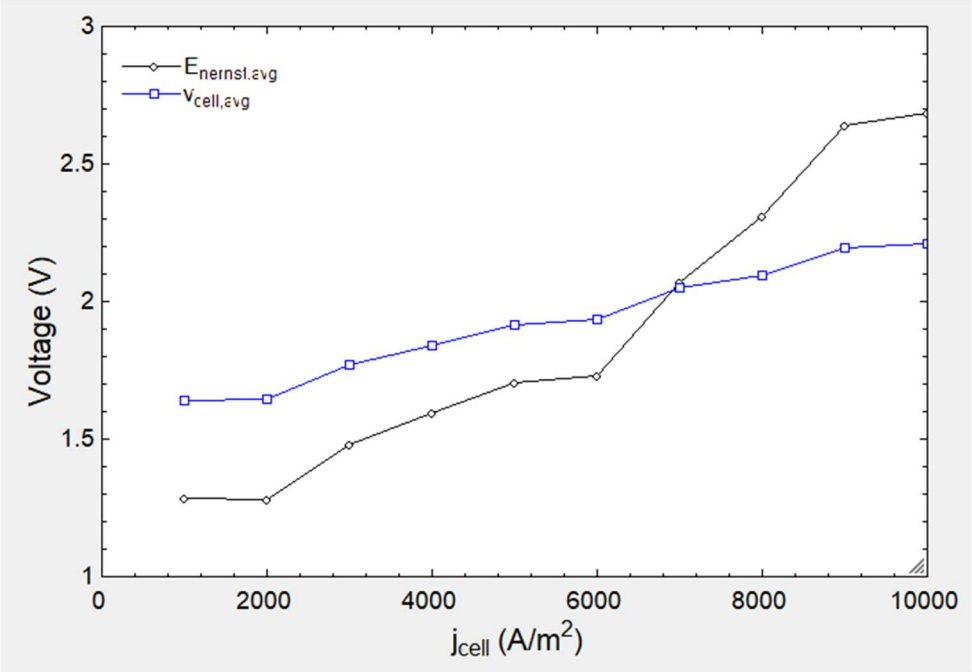

Figure 62: Current density vs. operating voltage for an ideal feed stream at 873K

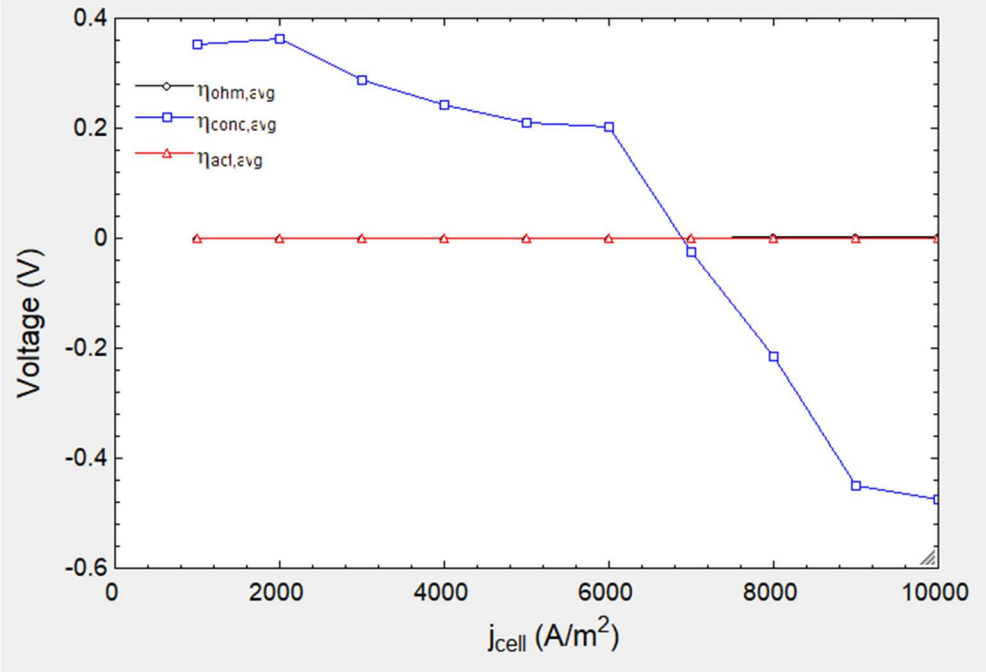

Figure 63: Current density vs. voltage losses for an ideal feed stream at 873K

We will not look at how the current density impacts cell operations when it is operating at 1000K. In Figure 64 we can see that the water usage is exacerbated with the water being fully

utilized by 4,000 A/m^2. After 4,000 A/m^2 the hydrogen content drops and becomes inversely proportional to the CO concentration. This phenomenon can be explained when analyzing the reaction kinetics shown in Figure 65. Methane oxidation increases as the current density is increased while the water gas shift increases drastically in the reverse direction. This high level of RWGS and a slight increase in methane oxidation and steam reforming indicates that the cell operates in a fuel cell configuration, utilizing the produced hydrogen as fuel to produce methane.

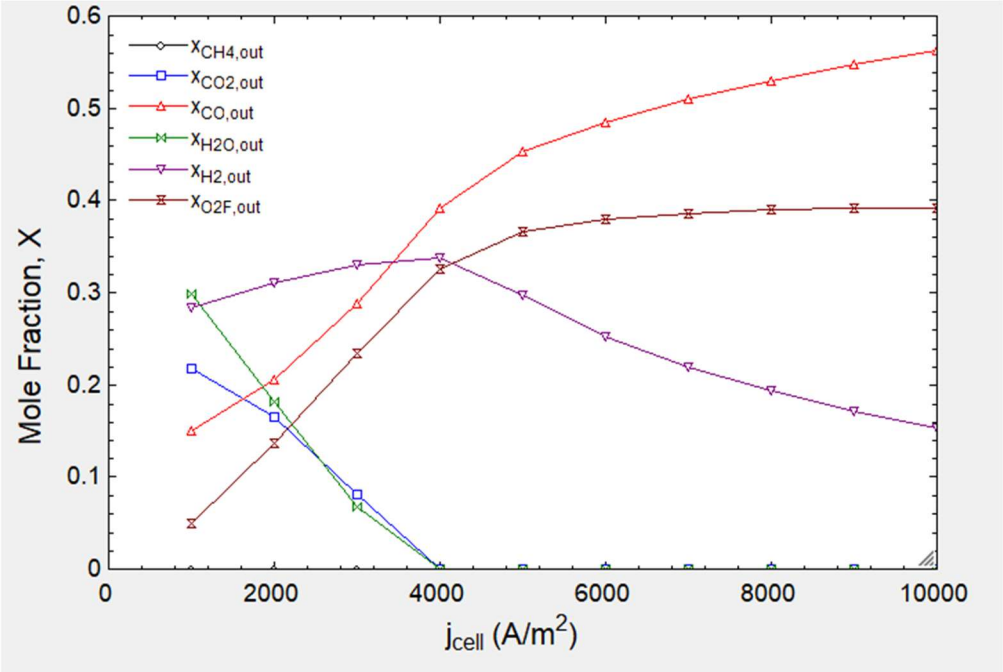

Figure 64: Current density vs. mole fraction for an ideal feed stream at 1000K

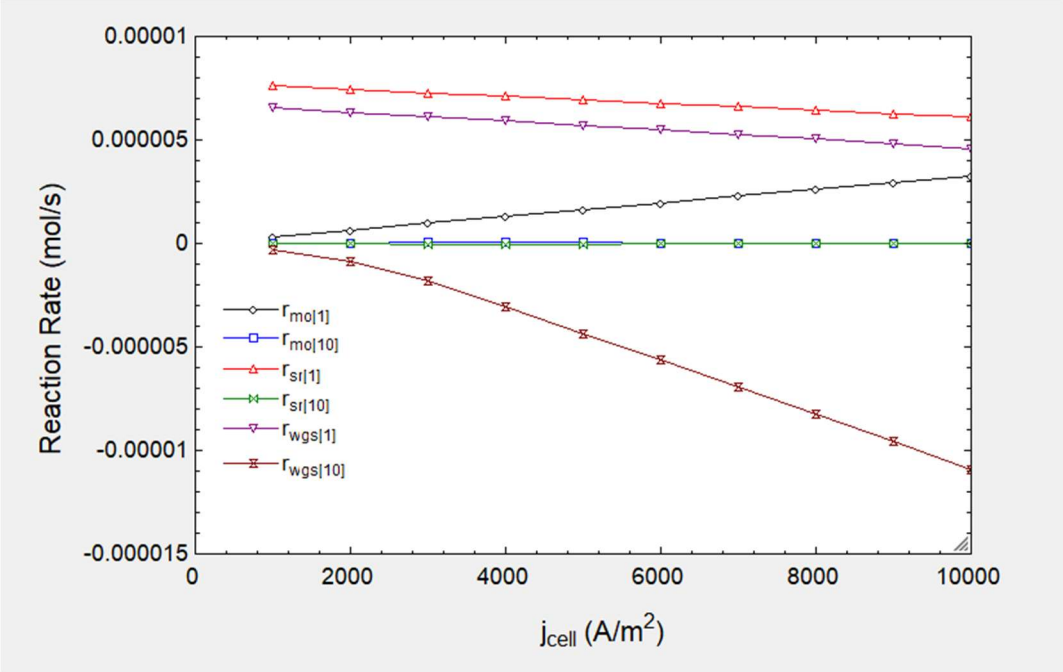

Figure 65: Current density vs. reaction rates for an ideal gas feed at 1000K

This swap from an electrolyzer to fuel cell configuration is validated by the voltage graphic and voltage losses shown in Figure 66 and Figure 67. After 4,000 A/m^2 the Nernst voltage spikes and overtakes the operational voltage between 4,000 A/m^2 and 5,000 A/m^2. Similar to the 873K condition, the production of water and the use of hydrogen causes the natural log of the pressure relationship for the anode and cathode to go negative, which indicates a loss of electrolyzer function. Although a negative concentration overpotential is not physically possible in a real cell, it does indicate when the cell is no longer operating in a electrolyzer configuration. These results indicate that when the PCER cell is operating at 1000K, the current density must be kept below 4,000 A/m^2.

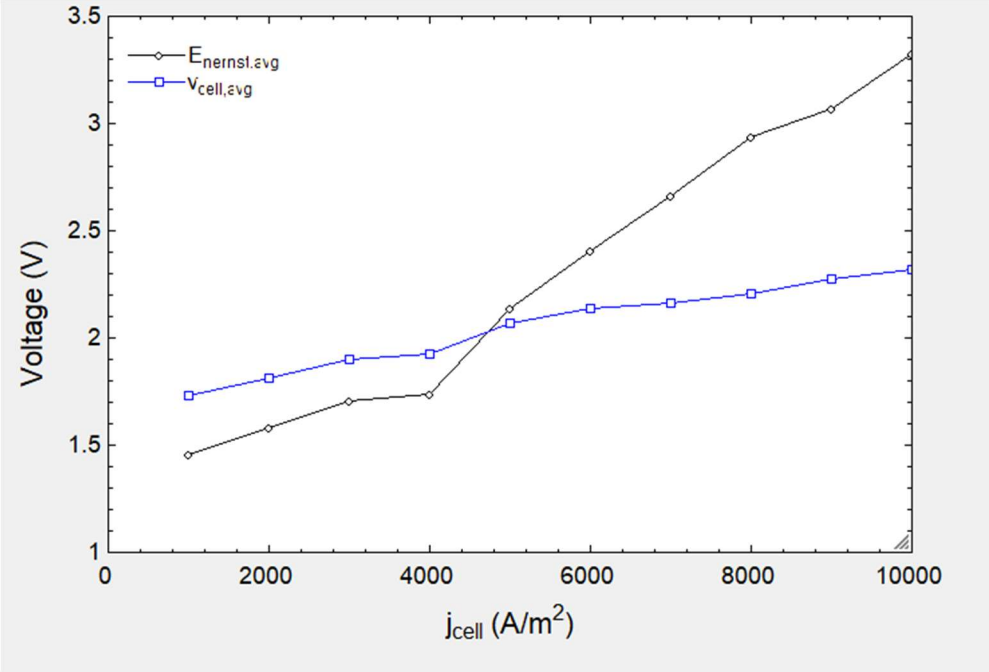

Figure 66: Current density vs. operating voltage for an ideal feed stream at 1000K

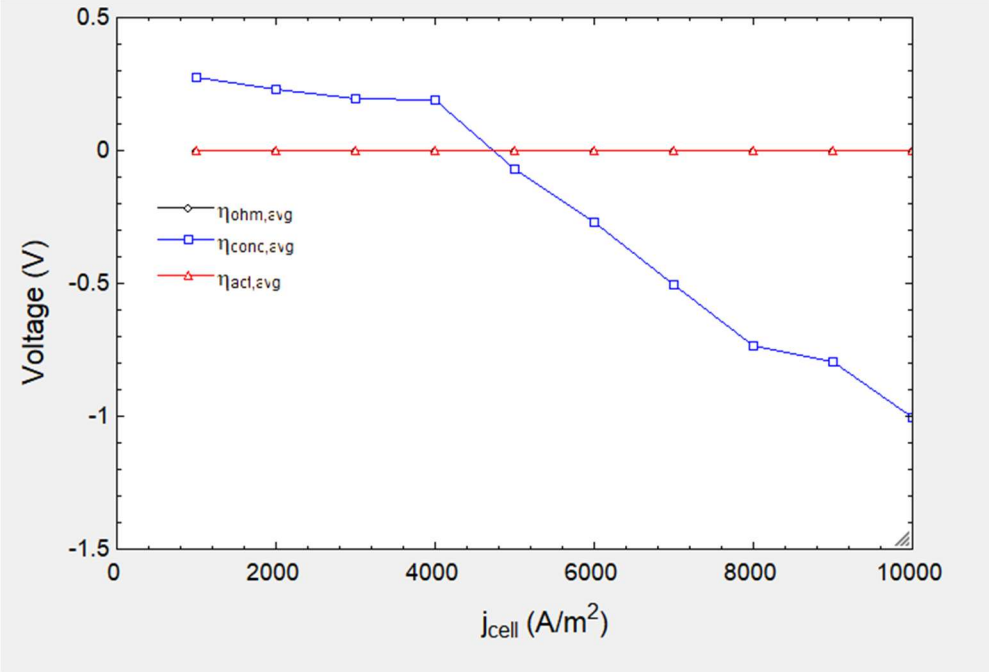

Figure 67: Current density vs. voltage losses for an ideal feed stream at 1000K

4.2.3.3: Real World Feedstock Electrochemical Operation at Different Current Densities

We will now study the impact that feeding the PCER unit the fuel composition obtained from the optimized engine testing at a spark timing of 11.5BTDC and a hydrogen blend of 20 mol%. As previously discussed, the composition utilizes an additional feed of water and methane in quantities of 40 mol% and 5 mol% respectively. We will now study the impact that the current density has on the electrochemical operation and outlet concentration from the cell at 673K, 873K, and then 1000K. The modified emissions at 673K show that the water content does not get fully utilized at any current density within this study, as shown in Figure 68. The reaction kinetics in Figure 69 show that both steam methane reforming and the water gas shift reaction are backwards by the last cell length, but the methane oxidation reaction is stronger than either of the reverse reactions. The methane oxidation reaction levels out at 5,000 A/m^2, so this condition will be further investigated.

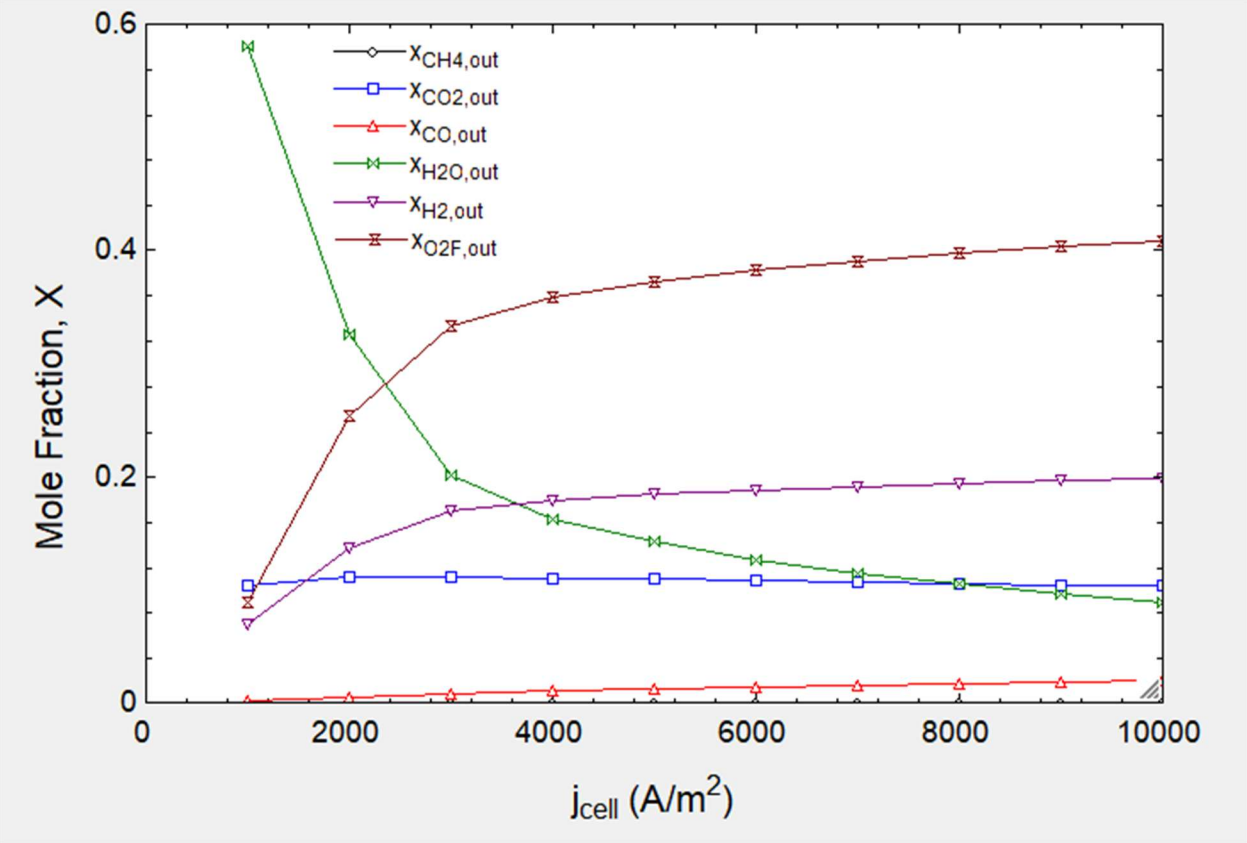

Figure 68: Current density vs. mole fraction for the modified feed condition at 673K

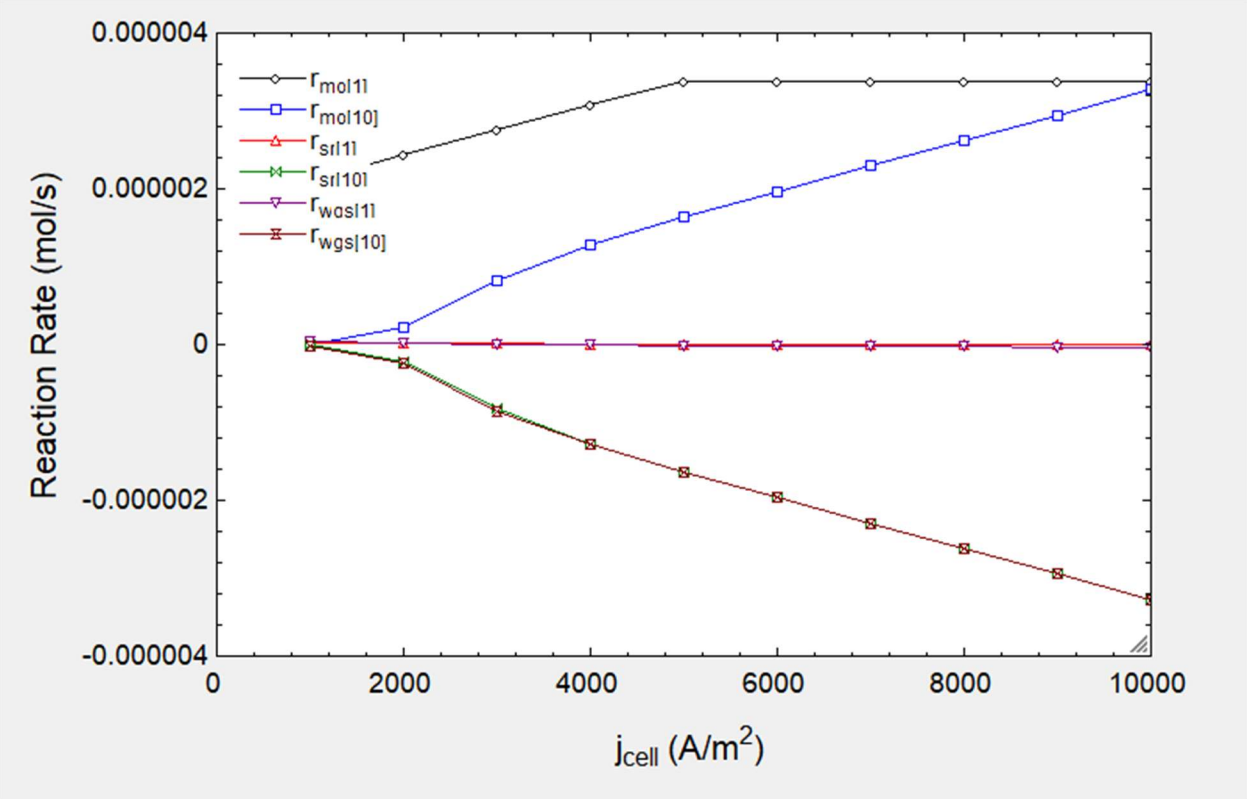

Figure 69: Current density vs. reaction rates for the modified feed case at 673K

At 673K the operating voltage shown in Figure 70 never goes below the Nernst voltage, although this results becomes less ideal when we study the losses in Figure 71. Between 4,000 A/m^2 and 5,000 A/m^2 the concentration losses become less than the ohmic and the activation losses, with the concentration losses leveling out slightly negative after 5,000 A/m^2. The activation losses are larger than the ohmic losses, with both losses increasing with an increase in current density. This pattern makes sense, with a higher current density putting more strain on the materials and the material needs a higher voltage for the system to overcome the activation limits. The concentration losses going to a slight negative are due to the RWGS and RSMR reactions creating small amounts of water, methane, and CO while utilizing CO_2 and H_2. Methane is not an issue because the methane oxidation reaction is more active than RWGS or RSMR. The issue comes from concentration losses, limiting the operating of the cell to less than 5,000 A/m^2. The

concentration losses are quite small, so this limitation may not be the case in experimental testing. This conclusion can be made because the concentration losses, when compared to other explored cases, is very small. This is even more apparent with ohmic losses and activation losses becoming larger than the concentration losses, which is a case that we have not see so far.

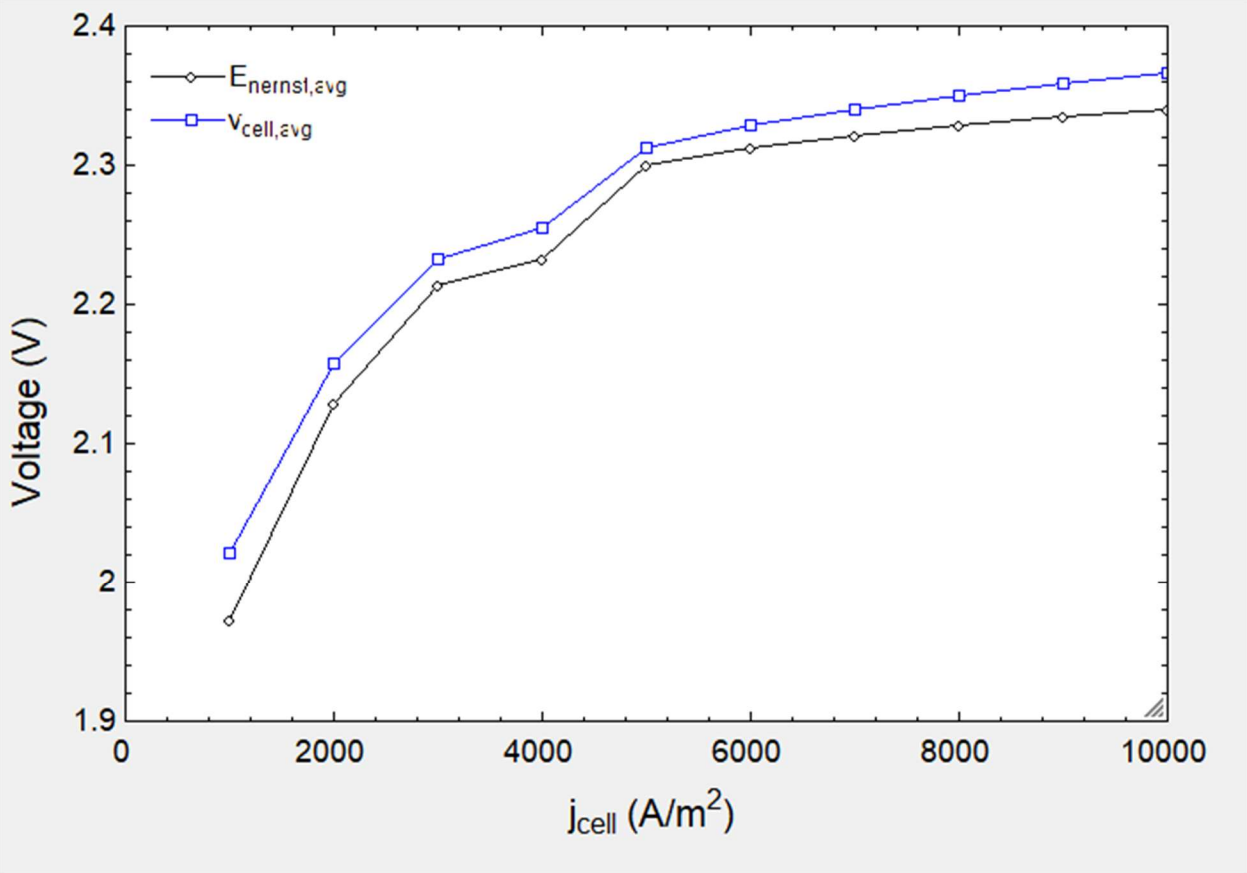

Figure 70: Current density vs. operating voltage with a modified cell feed at 673K

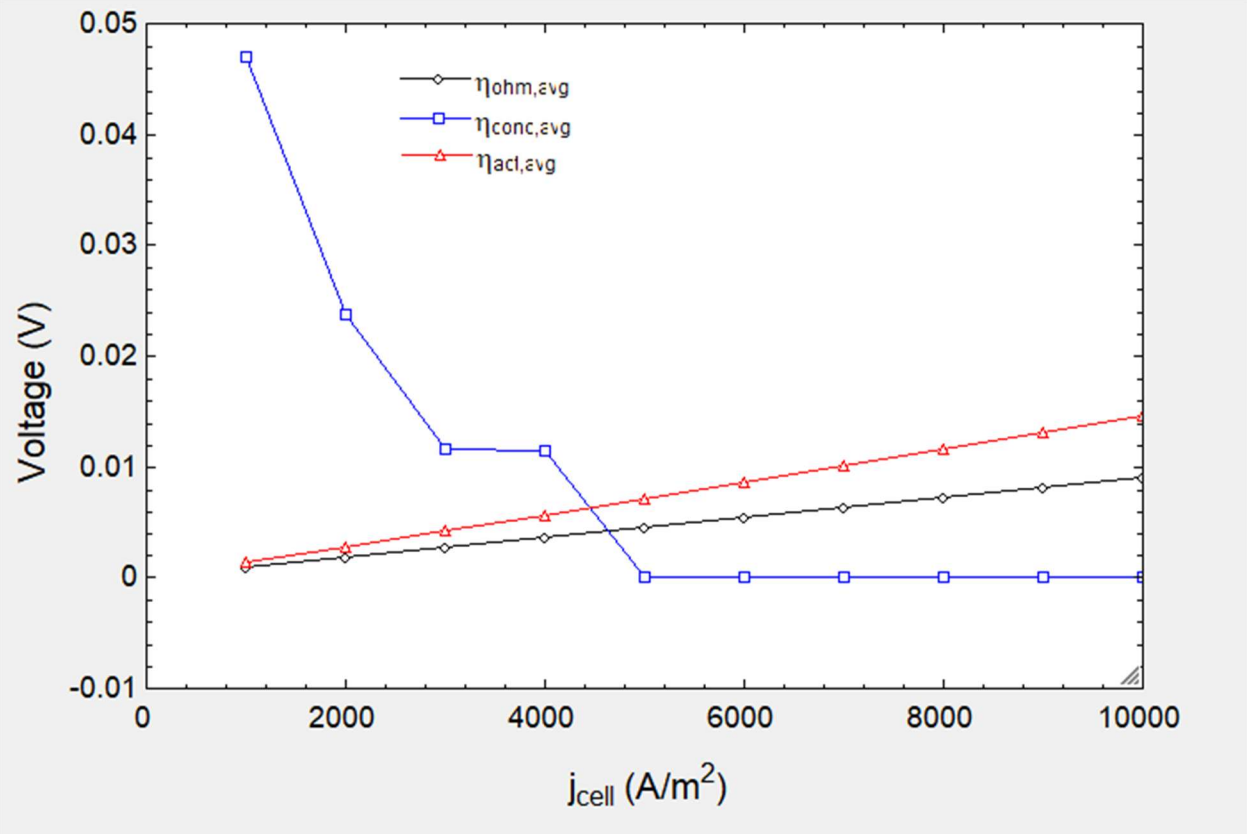

Figure 71: Current density vs. voltage losses with a modified cell feed operating at 673K

We will now look at the current density impact when the PCER model is set to 873K. Higher temperatures promote catalyst-driven reactions, which have been demonstrated in previous sections. With this being the case, we can see in Figure 72 that all of the water is fully utilized by 3,000 A/m^2 and the hydrogen peaks at this current density after dropping consistently as the current density is increased. The reaction rates in Figure 73 giver more context to this trend with the reverse water gas shift reaction overtaking the methane oxidation reaction after 3,000 A/m^2. This results in a drop in CO_2 early on and a consistent spike in CO as the current density increases. This issue translates to the electrochemical results, with the operating voltage in Figure 74 being higher than the Nernst voltage below 3,000 A/m^2. The concentration losses are the highest than seen previously goes as high as -1.2 volts at a current density of 8,000 A/m^2.

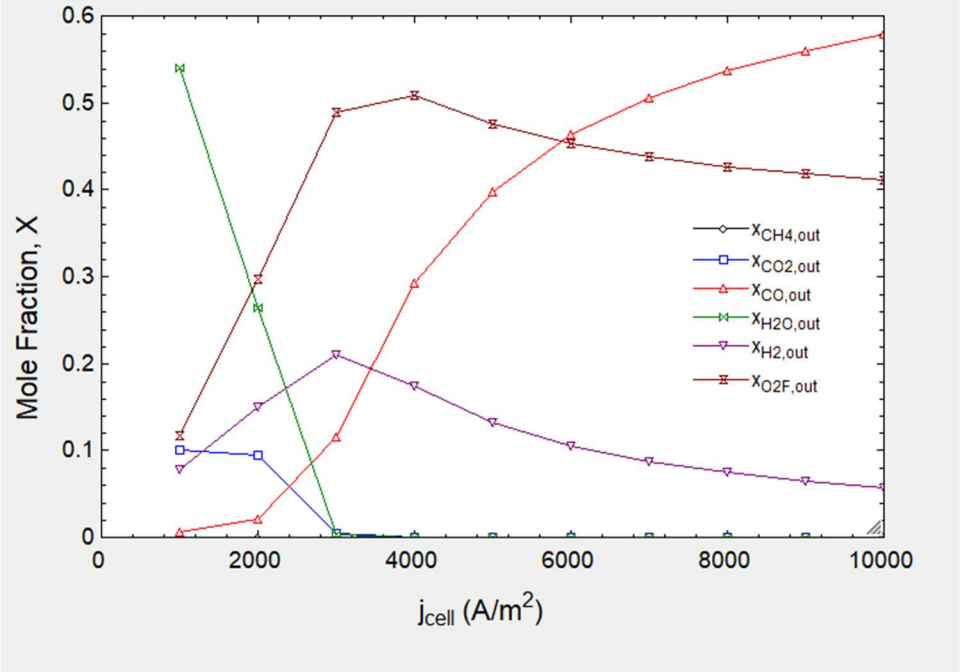

Figure 72: Current density vs. mole fraction for the modified feed condition at 873K

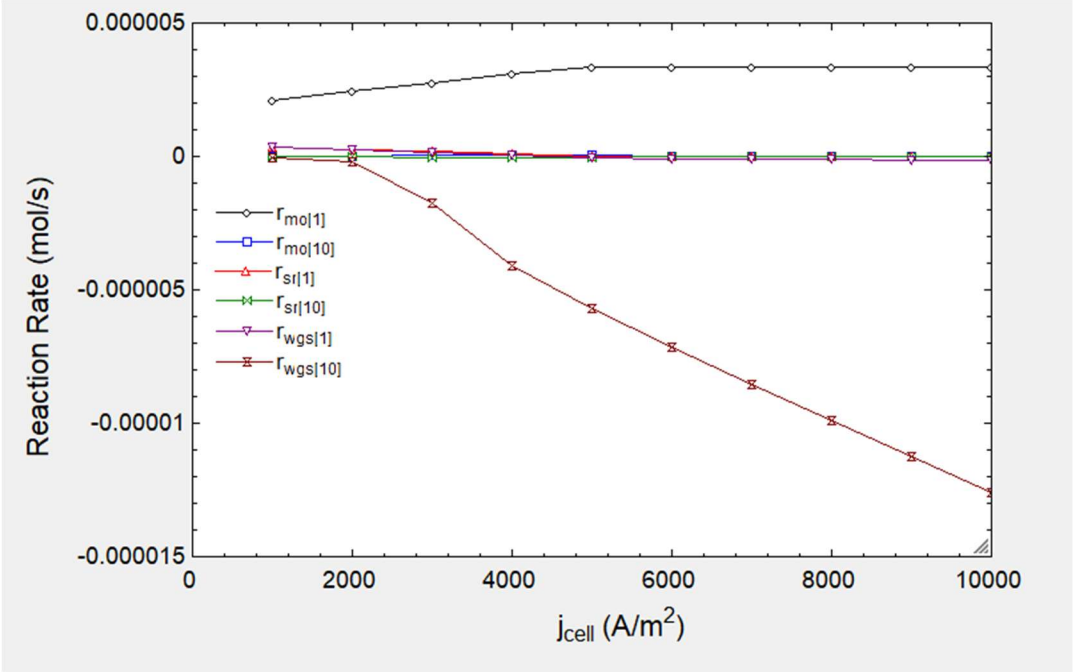

Figure 73: Current density vs. reaction rates for the modified feed case at 873K

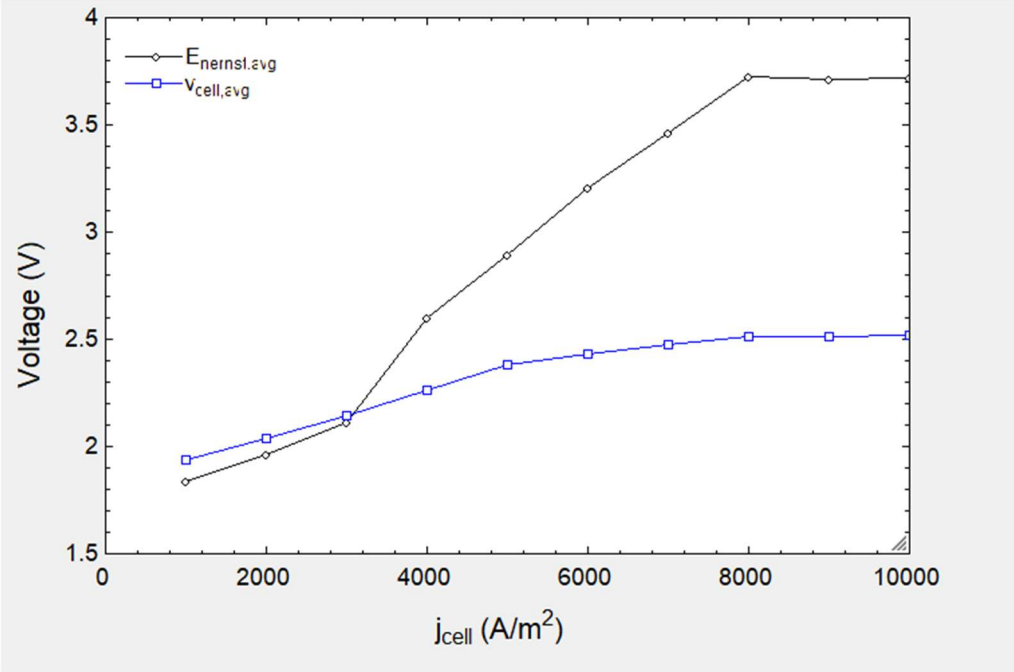

Figure 74: : Current density vs. operating voltage with a modified cell feed at 873K

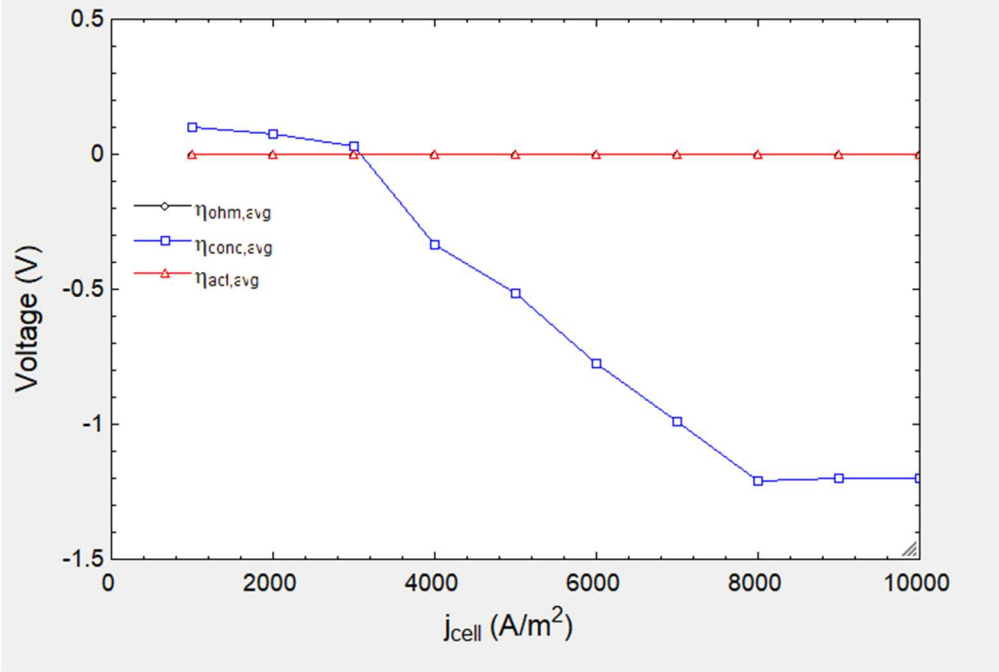

Figure 75: Current density vs. voltage losses with a modified cell feed operating at 873K

At 1000K the results are very similar to the 873K results with the mole fraction conversion of water dropping to 0 at 3,000 A/m^2 and hydrogen, CO_2, and oxygen all dropping

consistently at higher current densities as shown in Figure 76. The reactions have a similar trend to the reaction at 873K with the RWGS reaction becoming more powerful at 1000K as shown in Figure 77. Although the RWGS reaction is higher at 1000K, the electrical operating is not changed much when compared to 873K, with the maximum current density of 3,000 A/m^2 being the boundary before the concentration losses go negative as shown in Figure 79. At 3,000 A/m^2 the Nernst voltage overtakes the estimated operational voltage as shown in Figure 78.

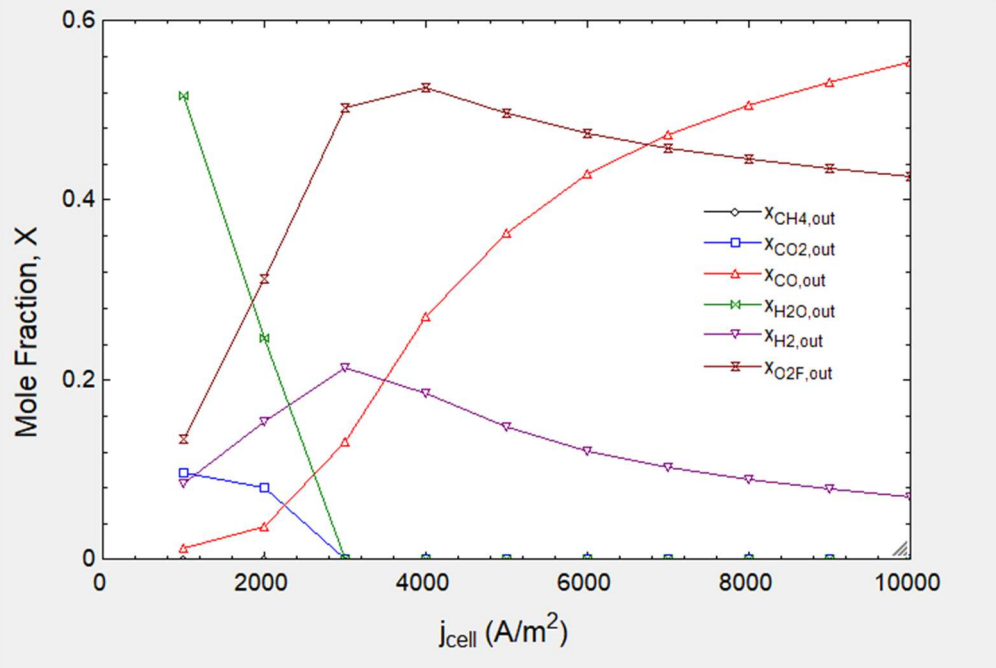

Figure 76: Current density vs. mole fraction for the modified feed condition at 1000K

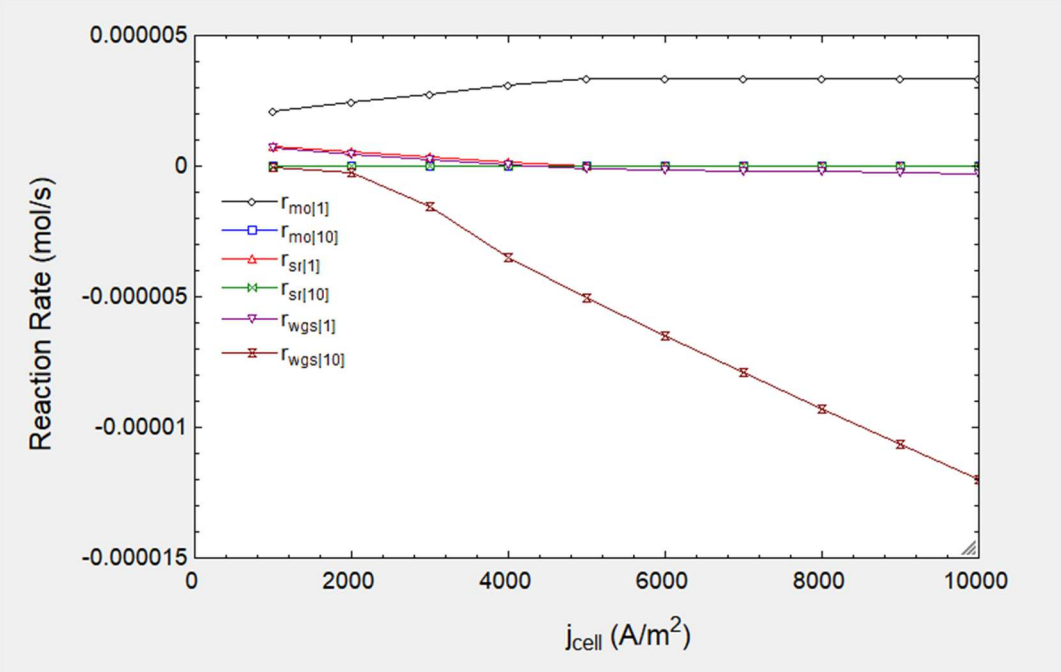

Figure 77: Current density vs. reaction rates for the modified feed case at 1000K

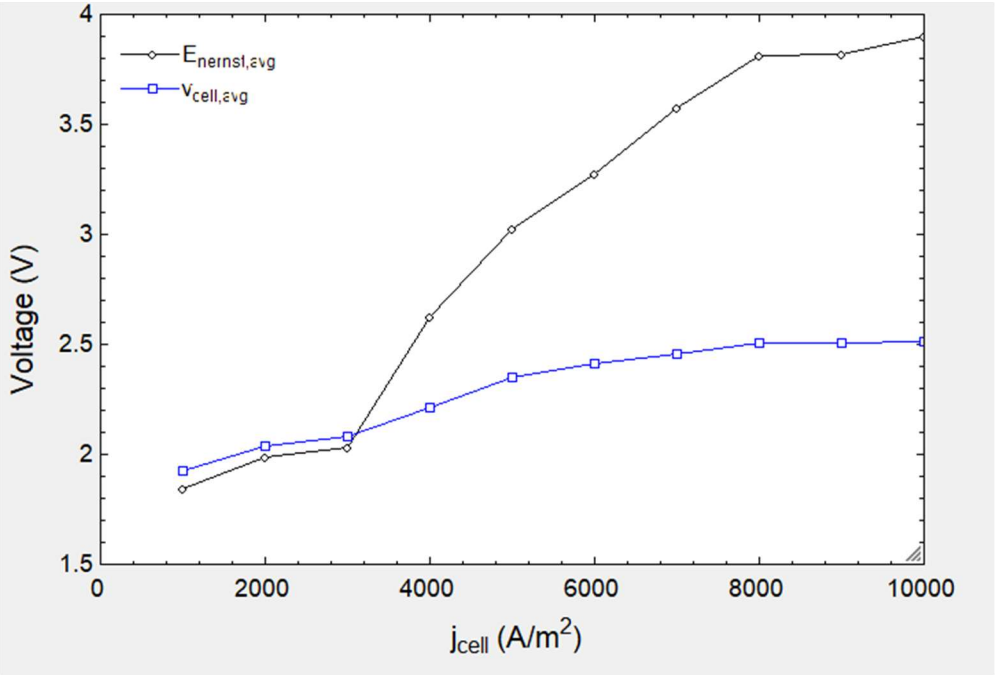

Figure 78: Current density vs. operating voltage with a modified cell feed at 1000K

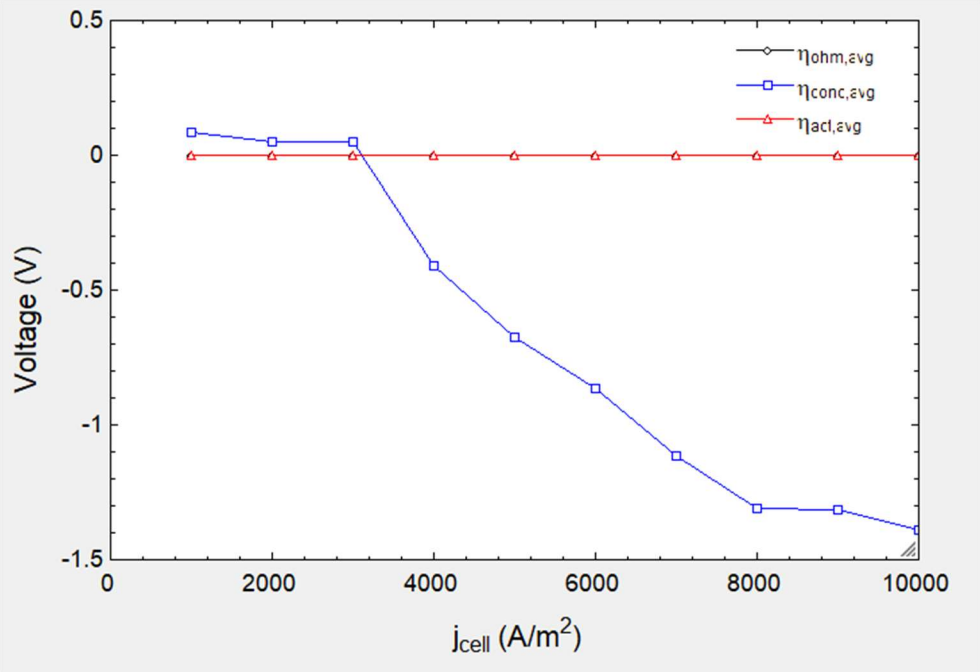

Figure 79: Current density vs. voltage losses with a modified cell feed operating at 1000K

After analyzing the real world modified emissions as a feedstock for the PCER cell for 673K, 873K, and 1000K, it can be concluded that a lower temperature operation benefits the cell by limiting the reversal of the water gas shift reaction and steam methane reaction, allowing for the maximum production of hydrogen and CO_2 while reducing the production of CO. By reducing these reactions, the cell can effectively operate in an electrolyzer configuration. The ideal case with real world modified emissions is to have the cell operating at a current density from 2,000 A/m^2 to 5,000 A/m^2 at a temperature of 673K. In section 4.2.1: Operating Temperature Impact it was observed that the cell was viable for operation at 780k, so further testing can be conducted to obtain an ideal current-to-temperature value, but for the sake of this study a range of 2,000-5,000 A/m^2 at a temperature between 673-780K will be used as a reference range for experimental testing.

4.2.4: PCER Validation Data

As previously discussed, no PCER system with the specified design and materials selections currently exists. The model framework is built off the work conducted by Norman et. al., so the general framework is validated [78]. The electrochemical model was built utilizing the work from Norman et. al. and Kazempoor et. al. [78], [124]. The steam methane reforming and water gas shift reactions are validated by matching the inlet concentration and temperature range that Palma et. al. had obtained and graphed the observed methane conversion rate from their work as shown in Figure 80. With the developed PCER model operating with water gas shift and steam methane reforming and the HER and MO reactions turned off, the model was able to obtain similar trends to what Palma et. al. had observed [116].

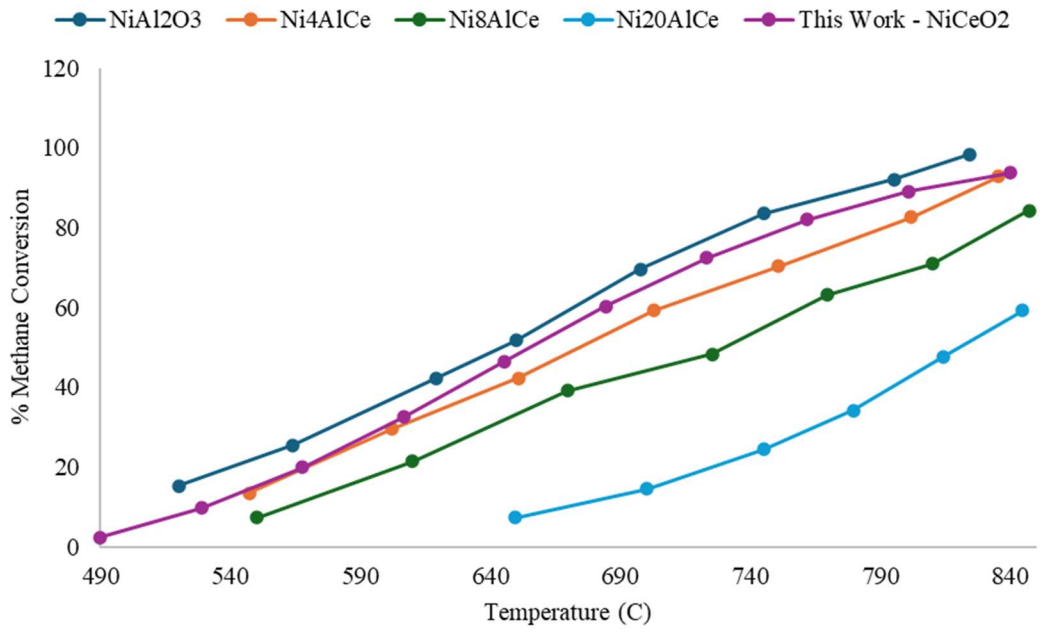

Figure 80: Temperature vs. methane conversion validation dataset matching this work to Palma et. al. [116]

4.3: Aspen HYSYS Modeling Results

The aspen HYSYS model simulates the combustion engine properties and operational conditions that are not measured on the experimental engine. It was observed in PCER modeling

that the addition of water and methane back into the system was necessary for effective PCER operation, along with pre-stream heating. Because of this, the Aspen HYSYS model was constructed as shown in Figure 81.

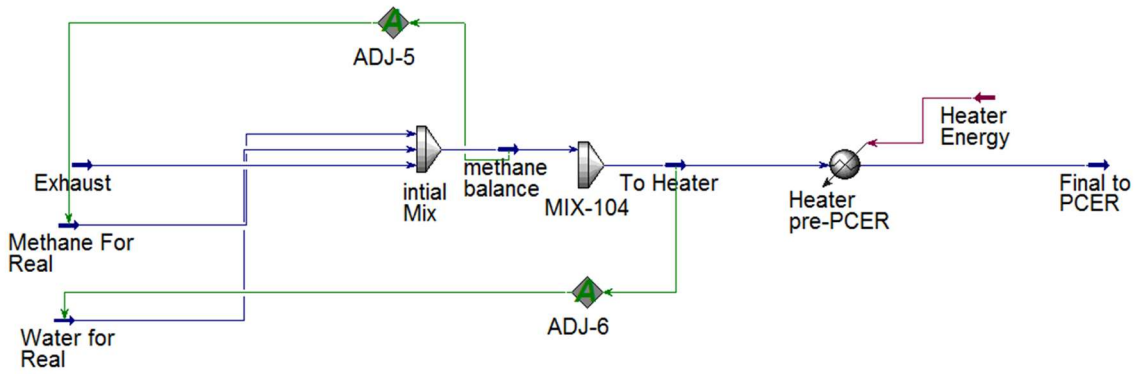

Figure 81: Aspen HYSYS engine model

The operational conditions from this model provided the flow rates and engine temperatures found in Table 14.

Table 14: Flow conditions used in the HYSYS model

Angle	$\dot{m}_{NG}$ (lb/min)	$\dot{V}_{air}$(ft^3/min)	Fuel Temperature (F)	Exhaust Temperature (F)
Baseline (11°BTDC, 0% H2)	0.485	372	97.0	479.6
11.5°BTDC, 20% H2	0.452	372	89.7	481.0

This thesis will focus on the modified engine condition emissions because it was used in the PCER modeling section. The modified emissions require the addition of 5 mol% of methane and 40 mol% of water. Due to the PCER unit operating at atmospheric pressure, no pumps were installed. The primary focus is to raise the flow temperature to 500°C as an estimate, as that

temperature found to be in the upper ranges for the cell operation utilizing the modified real-world exhaust stream. At this condition, the mass flows and heater duty for the addition of water and methane into the stream as shown in Table 15.

Table 15: HYSYS model and PCER parameters for PCER integration

Angle	Mol % CH4	Mol % H2O	$\dot{m}_{CH4}$ (kg/s)	$\dot{m}_{H2O}$ (kg/s)	$\dot{m}_{exhaust}$ (kg/s)	Heater Duty (KJ/h)
11.5°BTDC, 20% H2	5.15	49.17	$1.123*10^2$	0.1188	0.3396	$1.74*10^6$

Chapter 5: Conclusion and Future Works

In this thesis, various methods of reducing methane emissions from industrials engines are proposed and studied. The concept of hydrogen blending and spark ignition timing are studied experimentally on an AJAX DPC105. The spark ignition timing modification is able to reduce methane emissions when the engine timing is advanced to 11.5 degrees before top dead center (BTDC) and 12 degrees BTDC. The engine performance is also studied, with the thermal efficiency increasing when the timing is advanced. The addition of hydrogen to an optimized spark timing of 11.5°BTDC observed a methane reduction of 68.5% when 20% hydrogen is added to the system. The primary dataset analyzed used an engine load of 60%, with the validation data operating at 55% engine load. Future work can look at the impact that hydrogen blending and spark ignition timing can have on methane emission reductions at different engine loads and operational conditions. Additionally, a cost analysis needs to be conducted to understand the long-term cost difference that hydrogen blending in an engine that operates 24 hours a day, 7 days a week may incur when compared to the cost of replacing the engine. To complete the process and fully mitigate methane emissions, an electrochemical reactor is also proposed which is able to convert the tail gas of engine to hydrogen and CO2 through surface and electrochemical reactions. The protonic ceramic electrochemical reactor is modeled to convert engine exhaust emissions, namely methane, and produce hydrogen as a value-added chemical. The model is able to fully convert the methane emissions for both ideal and modified real-world cases. The real-world emissions in the PCER cell are found to be limited to an operational range of 2,000-5,000 A/m^2 at a temperature between 673-780K. Experimental testing is needed to further understand how the cell functions under real world conditions relating to both the electrochemical resistances and the effectiveness of the reaction kinetics. The PCER

model in this thesis is also quite small, so more work will have to be done to understand the operations of a larger cell. The aspen HYSYS model demonstrates a theoretical process blueprint for how to blend water and methane into the engine exhaust stream, but this condition should be modified and tuned based on the exact flow rates and heating requirements put forth by the real PCER cell when installed into the exhaust line of the DPC 105 natural gas compressor.

Citations:

[1] "Climate change impacts | National Oceanic and Atmospheric Administration." Accessed: Aug. 30, 2024. [Online]. Available: https://www.noaa.gov/education/resource-collections/climate/climate-change-impacts

[2] "Effects of Climate Change | Threats | WWF," World Wildlife Fund. Accessed: Aug. 30, 2024. [Online]. Available: https://www.worldwildlife.org/threats/effects-of-climate-change

[3] B. E. S. Team NASA's Earth Science News, "The Anatomy of Glacial Ice Loss," Climate Change: Vital Signs of the Planet. Accessed: Aug. 30, 2024. [Online]. Available: https://climate.nasa.gov/news/3038/the-anatomy-of-glacial-ice-loss

[4] "Climate Change: Mountain glaciers | NOAA Climate.gov." Accessed: Aug. 30, 2024. [Online]. Available: http://www.climate.gov/news-features/understanding-climate/climate-change-mountain-glaciers

[5] "Where are Earth's glaciers located? | U.S. Geological Survey." Accessed: Aug. 30, 2024. [Online]. Available: https://www.usgs.gov/faqs/where-are-earths-glaciers-located

[6] C. J. Huber *et al.*, "High-altitude glacier archives lost due to climate change-related melting," *Nat. Geosci.*, vol. 17, no. 2, pp. 110–113, Feb. 2024, doi: 10.1038/s41561-023-01366-1.

[7] "Isotope Analysis." Accessed: Aug. 30, 2024. [Online]. Available: https://groups.seas.harvard.edu/climate/eli/research/equable/isotope.html

[8] "What Are Proxy Data?," National Centers for Environmental Information (NCEI). Accessed: Aug. 30, 2024. [Online]. Available: https://www.ncei.noaa.gov/news/what-are-proxy-data

[9] O. US EPA, "Climate Change Indicators: Greenhouse Gases." Accessed: Sep. 03, 2024. [Online]. Available: https://www.epa.gov/climate-indicators/greenhouse-gases

[10] O. US EPA, "Overview of Greenhouse Gases." Accessed: Sep. 03, 2024. [Online]. Available: https://www.epa.gov/ghgemissions/overview-greenhouse-gases

[11] O. US EPA, "Importance of Methane." Accessed: Mar. 07, 2024. [Online]. Available: https://www.epa.gov/gmi/importance-methane

[12] "Methane | Vital Signs," Climate Change: Vital Signs of the Planet. Accessed: Sep. 03, 2024. [Online]. Available: https://climate.nasa.gov/vital-signs/methane?intent=121

[13] O. US EPA, "Greenhouse Gas Reporting Program (GHGRP)." Accessed: Dec. 15, 2024. [Online]. Available: https://www.epa.gov/ghgreporting

[14] "Regulatory Impact Analysis of the Waste Emissions Charge," U.S. Environmental Protection Agency Office of Atmospheric Protection Climate Change Division, Washington, D.C, EPA-430/R-24-007, Nov. 2024. Accessed: Dec. 15, 2024. [Online]. Available: https://www.regulations.gov/document/EPA-HQ-OAR-2023-0434-1097

[15] "The Demographic Outlook: 2024 to 2054 | Congressional Budget Office." Accessed: Dec. 10, 2024. [Online]. Available: https://www.cbo.gov/publication/59697

[16] "USDA Agricultural Projections to 2024," United States Department of Agriculture, Feb. 2015. Accessed: Dec. 10, 2024. [Online]. Available: https://www.ers.usda.gov/webdocs/outlooks/37753/51680_oce151e.pdf?v=9339#:~:text=As%20production%20increases%2C%20per%20capita,about%20215%20pounds%20by%202024.&text=remainder%20of%20the%20projection%20period.,over%20the%20next%20several%20years.

[17] O. US EPA, “National Overview: Facts and Figures on Materials, Wastes and Recycling.” Accessed: Dec. 10, 2024. [Online]. Available: https://www.epa.gov/facts-and-figures-about-materials-waste-and-recycling/national-overview-facts-and-figures-materials
[18] “DOE Explains...the Carbon Cycle,” Energy.gov. Accessed: Dec. 10, 2024. [Online]. Available: https://www.energy.gov/science/doe-explainsthe-carbon-cycle
[19] O. US EPA, “Inventory of U.S. Greenhouse Gas Emissions and Sinks: 1990-2022.” Accessed: Dec. 11, 2024. [Online]. Available: https://www.epa.gov/ghgemissions/inventory-us-greenhouse-gas-emissions-and-sinks-1990-2022
[20] O. US EPA, “Estimates of Methane Emissions by Segment in the United States.” Accessed: Dec. 11, 2024. [Online]. Available: https://www.epa.gov/natural-gas-star-program/estimates-methane-emissions-segment-united-states
[21] “Inventory of U.S. Greenhouse Gas Emissions and Sinks 1990-2022: Updates for Transmission Compressor Station Activity,” United States Environmental Protection Agency, Apr. 2024. [Online]. Available: https://www.epa.gov/system/files/documents/2024-04/2024-ghgi-update_transmissionactivity_april2024.pdf
[22] J. G. Speight, “Chapter 10 - Combustion of Hydrocarbons,” in *Handbook of Industrial Hydrocarbon Processes*, J. G. Speight, Ed., Boston: Gulf Professional Publishing, 2011, pp. 355–393. doi: 10.1016/B978-0-7506-8632-7.10010-6.
[23] “Biogas (a promising bioenergy source): A critical review on the potential of biogas as a sustainable energy source for gaseous fuelled spark ignition engines - ScienceDirect.” Accessed: Dec. 21, 2024. [Online]. Available: https://www.sciencedirect.com/science/article/pii/S0360319922055112
[24] Y. Zhang, M. Jeanson, R. Mével, Z. Chen, and N. Chaumeix, “Tailored mixture properties for accurate laminar flame speed measurement from spherically expanding flames: Application to H2/O2/N2/He mixtures,” *Combustion and Flame*, vol. 231, p. 111487, Sep. 2021, doi: 10.1016/j.combustflame.2021.111487.
[25] E. Porpatham, A. Ramesh, and B. Nagalingam, “Effect of hydrogen addition on the performance of a biogas fuelled spark ignition engine,” *International Journal of Hydrogen Energy*, vol. 32, no. 12, pp. 2057–2065, Aug. 2007, doi: 10.1016/j.ijhydene.2006.09.001.
[26] P. Cai, H. Liu, Y. Liu, Y. Zhou, A. Yu, and Z. Yang, “Effect of gas composition and initial turbulence on the propagation dynamics of premixed flames of hydrogen-blended natural gas fuel,” *Case Studies in Thermal Engineering*, vol. 61, p. 104838, Sep. 2024, doi: 10.1016/j.csite.2024.104838.
[27] M. Aravindan *et al.*, “Unlocking clean gas with hydrogen: A combustion optimization study,” *Results in Engineering*, vol. 23, p. 102363, Sep. 2024, doi: 10.1016/j.rineng.2024.102363.
[28] M. Ozturk, F. Sorgulu, N. Javani, and I. Dincer, “An experimental study on the environmental impact of hydrogen and natural gas blend burning,” *Chemosphere*, vol. 329, p. 138671, Jul. 2023, doi: 10.1016/j.chemosphere.2023.138671.
[29] J. Thangaraja and C. Kannan, “Effect of exhaust gas recirculation on advanced diesel combustion and alternate fuels - A review,” *Applied Energy*, vol. 180, pp. 169–184, Oct. 2016, doi: 10.1016/j.apenergy.2016.07.096.
[30] C. S. Callahan, E. Gatica, S. C. Coburn, G. J. Hampson, and G. B. Rieker, “Compact, real-time exhaust gas recirculation rate sensor for use in natural gas combustion engine

control," *Proceedings of the Combustion Institute*, vol. 40, no. 1, p. 105692, Jan. 2024, doi: 10.1016/j.proci.2024.105692.
[31] "14.4: Heterogeneous Catalysts," Chemistry LibreTexts. Accessed: Dec. 27, 2024. [Online]. Available: https://chem.libretexts.org/Bookshelves/Inorganic_Chemistry/Inorganic_Chemistry_(LibreTexts)/14%3A_Organometallic_Reactions_and_Catalysis/14.04%3A_Heterogeneous_Catalysts
[32] B. Guan, R. Zhan, H. Lin, and Z. Huang, "Review of the state-of-the-art of exhaust particulate filter technology in internal combustion engines," *Journal of Environmental Management*, vol. 154, pp. 225–258, May 2015, doi: 10.1016/j.jenvman.2015.02.027.
[33] M. Giuliano, G. Ricchiardi, A. Damin, M. Sgroi, G. Nicol, and F. Parussa, "Thermal Ageing Effects in a Commercial Three-Way Catalyst: Physical Characterization of Washcoat and Active Metal Evolution," *Int.J Automot. Technol.*, vol. 21, no. 2, pp. 329–337, Apr. 2020, doi: 10.1007/s12239-020-0031-x.
[34] R. Prins, A. Wang, and X. Li, *Introduction to Heterogeneous Catalysis*, Second edition., vol. Volume 1. in Advanced Textbooks in Chemistry, no. Volume 1, vol. Volume 1. WORLD SCIENTIFIC (EUROPE), 2015. doi: 10.1142/q0024.
[35] A. P. E. York and A. Tsolakis, "Cleaner Vehicle Emissions," in *Encyclopedia of Materials: Science and Technology*, K. H. J. Buschow, R. W. Cahn, M. C. Flemings, B. Ilschner, E. J. Kramer, S. Mahajan, and P. Veyssière, Eds., Oxford: Elsevier, 2010, pp. 1–7. doi: 10.1016/B978-008043152-9.02253-3.
[36] D. Kim *et al.*, "High-Performance Protonic Ceramic Electrochemical Cells," *ACS Energy Lett.*, vol. 7, no. 7, pp. 2393–2400, Jul. 2022, doi: 10.1021/acsenergylett.2c01370.
[37] W. Sitte and R. Merkle, *High-temperature electrolysis: from fundamentals to applications*. Bristol: IOP publishing, 2023.
[38] Z. Fu, Y. Li, H. Chen, J. Du, Y. Li, and W. Gao, "Effect of Hydrogen Blending on the Combustion Performance of a Gasoline Direct Injection Engine," *ACS Omega*, vol. 7, no. 15, pp. 13022–13030, Apr. 2022, doi: 10.1021/acsomega.2c00343.
[39] S. M. M. E. Ayad, C. R. P. Belchior, G. L. R. da Silva, R. S. Lucena, E. S. Carreira, and P. E. V. de Miranda, "Analysis of performance parameters of an ethanol fueled spark ignition engine operating with hydrogen enrichment," *International Journal of Hydrogen Energy*, vol. 45, no. 8, pp. 5588–5606, Feb. 2020, doi: 10.1016/j.ijhydene.2019.05.151.
[40] U. Rajak, K. C. Apparao, T. N. Verma, and Ü. Ağbulut, "Enhancing performance, and combustion efficiency, and reducing tailpipe emissions of an engine fuelled with hydrogen-enriched diesel and ethanol blends at varying CRs using RSM," *International Journal of Hydrogen Energy*, vol. 92, pp. 1236–1247, Nov. 2024, doi: 10.1016/j.ijhydene.2024.10.289.
[41] W. C. Nadaleti, G. Przybyla, P. Belli Filho, and S. Souza, "Methane-hydrogen fuel blends for SI engines in Brazilian public transport: Efficiency and pollutant emissions," *International Journal of Hydrogen Energy*, vol. 42, no. 49, pp. 29585–29596, Dec. 2017, doi: 10.1016/j.ijhydene.2017.10.068.
[42] X. Yu *et al.*, "Effects of hydrogen blending ratio on combustion and emission characteristics of an ammonia/hydrogen compound injection engine under different excess air coefficients," *International Journal of Hydrogen Energy*, vol. 49, pp. 1033–1047, Jan. 2024, doi: 10.1016/j.ijhydene.2023.10.049.

[43] F. Moreno, M. Muñoz, J. Arroyo, O. Magén, C. Monné, and I. Suelves, “Efficiency and emissions in a vehicle spark ignition engine fueled with hydrogen and methane blends,” *International Journal of Hydrogen Energy*, vol. 37, no. 15, pp. 11495–11503, Aug. 2012, doi: 10.1016/j.ijhydene.2012.04.012.
[44] H. Zhunqing, S. Nannan, J. Yi, and Z. Xin, “Experimental research on a blended hydrogen-fuel engine,” *International Journal of Hydrogen Energy*, vol. 48, no. 19, pp. 7115–7121, Mar. 2023, doi: 10.1016/j.ijhydene.2022.05.053.
[45] J. Zheng, E. Hu, Z. Huang, D. Ning, and J. Wang, “Combustion and emission characteristics of a spray guided direct-injection spark-ignition engine fueled with natural gas-hydrogen blends,” *International Journal of Hydrogen Energy*, vol. 36, no. 17, pp. 11155–11163, Aug. 2011, doi: 10.1016/j.ijhydene.2011.05.119.
[46] L. De Simio, S. Iannaccone, C. Guido, P. Napolitano, and A. Maiello, “Natural Gas/Hydrogen blends for heavy-duty spark ignition engines: Performance and emissions analysis,” *International Journal of Hydrogen Energy*, vol. 50, pp. 743–757, Jan. 2024, doi: 10.1016/j.ijhydene.2023.06.194.
[47] N. Kahraman, B. Çeper, S. O. Akansu, and K. Aydin, “Investigation of combustion characteristics and emissions in a spark-ignition engine fuelled with natural gas–hydrogen blends,” *International Journal of Hydrogen Energy*, vol. 34, no. 2, pp. 1026–1034, Jan. 2009, doi: 10.1016/j.ijhydene.2008.10.075.
[48] P. T. Nitnaware and J. G. Suryawanshi, “Effects of MBT spark timing on performance emission and combustion characteristics of S.I engine using hydrogen-CNG blends,” *International Journal of Hydrogen Energy*, vol. 41, no. 1, pp. 666–674, Jan. 2016, doi: 10.1016/j.ijhydene.2015.11.074.
[49] S. Di Iorio, P. Sementa, and B. M. Vaglieco, “Experimental investigation on the combustion process in a spark ignition optically accessible engine fueled with methane/hydrogen blends,” *International Journal of Hydrogen Energy*, vol. 39, no. 18, pp. 9809–9823, Jun. 2014, doi: 10.1016/j.ijhydene.2014.04.065.
[50] Y. Ichikawa, “Retrofit concept for 100% hydrogen operation on natural gas lean-burn engine with spark ignition and prechamber system: Engine performance under hydrogen-mixing and load limits,” *International Journal of Hydrogen Energy*, vol. 60, pp. 1275–1287, Mar. 2024, doi: 10.1016/j.ijhydene.2024.02.159.
[51] C. Ingo, J. Tuuf, and M. Björklund-Sänkiaho, “Experimental study of the performance of a SI-engine fueled with hydrogen-natural gas mixtures,” *International Journal of Hydrogen Energy*, vol. 63, pp. 1036–1043, Apr. 2024, doi: 10.1016/j.ijhydene.2024.03.252.
[52] G. Verma, R. K. Prasad, R. A. Agarwal, S. Jain, and A. K. Agarwal, “Experimental investigations of combustion, performance and emission characteristics of a hydrogen enriched natural gas fuelled prototype spark ignition engine,” *Fuel*, vol. 178, pp. 209–217, Aug. 2016, doi: 10.1016/j.fuel.2016.03.022.
[53] J. Liu, X. Duan, Z. Yuan, Q. Liu, and Q. Tang, “Experimental study on the performance, combustion and emission characteristics of a high compression ratio heavy-duty spark-ignition engine fuelled with liquefied methane gas and hydrogen blend,” *Applied Thermal Engineering*, vol. 124, pp. 585–594, Sep. 2017, doi: 10.1016/j.applthermaleng.2017.06.067.
[54] S. M. V. Sagar and A. K. Agarwal, “Knocking behavior and emission characteristics of a port fuel injected hydrogen enriched compressed natural gas fueled spark ignition engine,”

Applied Thermal Engineering, vol. 141, pp. 42–50, Aug. 2018, doi: 10.1016/j.applthermaleng.2018.05.102.
[55] V. Pandey, I. A. Badruddin, and T. M. Y. Khan, "Effect of H2 blends with compressed natural gas on emissions of SI engine having modified ignition timings," *Fuel*, vol. 321, p. 123930, Aug. 2022, doi: 10.1016/j.fuel.2022.123930.
[56] X. Duan, X. Chu, M. Lai, and Z. Sun, "Effects of industrial hydrogen-rich gases on the performance of the spark ignition engine under various combustion modes," *Case Studies in Thermal Engineering*, vol. 63, p. 105358, Nov. 2024, doi: 10.1016/j.csite.2024.105358.
[57] R. K. Prasad, N. Mustafi, and A. K. Agarwal, "Effect of spark timing on laser ignition and spark ignition modes in a hydrogen enriched compressed natural gas fuelled engine," *Fuel*, vol. 276, p. 118071, Sep. 2020, doi: 10.1016/j.fuel.2020.118071.
[58] P. Xu *et al.*, "Realizing low emissions on a hydrogen-fueled spark ignition engine at the cold start period under rich combustion through ignition timing control," *International Journal of Hydrogen Energy*, vol. 44, no. 16, pp. 8650–8658, Mar. 2019, doi: 10.1016/j.ijhydene.2019.01.275.
[59] P. Dimopoulos, C. Bach, P. Soltic, and K. Boulouchos, "Hydrogen–natural gas blends fuelling passenger car engines: Combustion, emissions and well-to-wheels assessment," *International Journal of Hydrogen Energy*, vol. 33, no. 23, pp. 7224–7236, Dec. 2008, doi: 10.1016/j.ijhydene.2008.07.012.
[60] E. Hu, Z. Huang, B. Liu, J. Zheng, X. Gu, and B. Huang, "Experimental investigation on performance and emissions of a spark-ignition engine fuelled with natural gas–hydrogen blends combined with EGR," *International Journal of Hydrogen Energy*, vol. 34, no. 1, pp. 528–539, Jan. 2009, doi: 10.1016/j.ijhydene.2008.10.042.
[61] B. Huang, E. Hu, Z. Huang, J. Zheng, B. Liu, and D. Jiang, "Cycle-by-cycle variations in a spark ignition engine fueled with natural gas–hydrogen blends combined with EGR," *International Journal of Hydrogen Energy*, vol. 34, no. 19, pp. 8405–8414, Oct. 2009, doi: 10.1016/j.ijhydene.2009.08.002.
[62] R. Peters, R. Dahl, U. Klüttgen, C. Palm, and D. Stolten, "Internal reforming of methane in solid oxide fuel cell systems," *Journal of Power Sources*, vol. 106, no. 1, pp. 238–244, Apr. 2002, doi: 10.1016/S0378-7753(01)01039-4.
[63] F. Liu, H. Deng, H. Ding, P. Kazempoor, B. Liu, and C. Duan, "Process-intensified protonic ceramic fuel cells for power generation, chemical production, and greenhouse gas mitigation," *Joule*, vol. 7, no. 6, pp. 1308–1332, Jun. 2023, doi: 10.1016/j.joule.2023.05.009.
[64] B. Zhang *et al.*, "A real-time multiphysics model of a pressurized solid oxide electrolysis cell (SOEC) for cyber-physical simulation," *Energy Conversion and Management*, vol. 298, p. 117778, Dec. 2023, doi: 10.1016/j.enconman.2023.117778.
[65] B. Hu, F. Rosner, H. Breunig, A. Sarycheva, R. Kostecki, and M. C. Tucker, "Electrochemical conversion of methane to ethylene, olefins, and paraffins using metal-supported solid oxide cells," *International Journal of Hydrogen Energy*, vol. 48, no. 86, pp. 33537–33547, Oct. 2023, doi: 10.1016/j.ijhydene.2023.05.114.
[66] J.-H. Zhang, L.-B. Lei, D. Liu, F.-Y. Zhao, M. Ni, and F. Chen, "Mathematical modeling of a proton-conducting solid oxide fuel cell with current leakage," *Journal of Power Sources*, vol. 400, pp. 333–340, Oct. 2018, doi: 10.1016/j.jpowsour.2018.08.038.

[67] A. K. Nayak and A. Sasmal, “Recent advance on fundamental properties and synthesis of barium zirconate for proton conducting ceramic fuel cell,” *Journal of Cleaner Production*, vol. 386, p. 135827, Feb. 2023, doi: 10.1016/j.jclepro.2022.135827.
[68] S. Hossain, A. M. Abdalla, S. N. B. Jamain, J. H. Zaini, and A. K. Azad, “A review on proton conducting electrolytes for clean energy and intermediate temperature-solid oxide fuel cells,” *Renewable and Sustainable Energy Reviews*, vol. 79, pp. 750–764, Nov. 2017, doi: 10.1016/j.rser.2017.05.147.
[69] D. Clark *et al.*, “Single-step hydrogen production from NH3, CH4, and biogas in stacked proton ceramic reactors,” *Science*, vol. 376, no. 6591, pp. 390–393, Apr. 2022, doi: 10.1126/science.abj3951.
[70] H. H. Al Naji, O. Siddiqui, S. N. Paglieri, and A. Alahmed, “Multi-physics open-source computational modeling of a protonic membrane reformer for lower-carbon compressed hydrogen production,” *International Journal of Hydrogen Energy*, vol. 103, pp. 951–963, Feb. 2025, doi: 10.1016/j.ijhydene.2025.01.147.
[71] H. Malerød-Fjeld *et al.*, “Thermo-electrochemical production of compressed hydrogen from methane with near-zero energy loss,” *Nat Energy*, vol. 2, no. 12, pp. 923–931, Dec. 2017, doi: 10.1038/s41560-017-0029-4.
[72] I. Yuste-Tirados, X. Liu, C. Kjølseth, and T. Norby, “Impedance of a tubular electrochemical cell with BZCY electrolyte and Ni-BZCY cermet electrodes for proton ceramic membrane reactors,” *International Journal of Hydrogen Energy*, vol. 48, no. 77, pp. 30027–30038, Sep. 2023, doi: 10.1016/j.ijhydene.2023.03.401.
[73] A. Dubois, S. Ricote, and R. J. Braun, “Benchmarking the expected stack manufacturing cost of next generation, intermediate-temperature protonic ceramic fuel cells with solid oxide fuel cell technology,” *Journal of Power Sources*, vol. 369, pp. 65–77, Nov. 2017, doi: 10.1016/j.jpowsour.2017.09.024.
[74] A. Moranti, J. Dailly, M. Santarelli, and F. Smeacetto, “Techno-economic analysis on proton conductor ceramic based technologies for various materials, configurations, applications and products,” *Energy Conversion and Management*, vol. 321, p. 119082, Dec. 2024, doi: 10.1016/j.enconman.2024.119082.
[75] D. Yan *et al.*, “Multi-Physical and Electrochemical Coupling Model for the Protonic Ceramic Fuel Cells with H+/e−/O2− Mixed Conducting Cathodes,” *Applied Sciences*, vol. 12, no. 8, p. 3889, Apr. 2022, doi: 10.3390/app12083889.
[76] Sasmoko, S.-W. Lee, M. Bhavanari, W. Wijayanti, N. Osman, and C.-J. Tseng, “System analysis of a protonic ceramic fuel cell and gas turbine hybrid system with methanol reformer,” *International Journal of Hydrogen Energy*, vol. 48, no. 30, pp. 11421–11430, Apr. 2023, doi: 10.1016/j.ijhydene.2022.06.220.
[77] S. Lei, A. Wang, G. Weng, Y. Wu, J. Xue, and H. Wang, “Simultaneous generation of electricity, ethylene and decomposition of nitrous oxide via protonic ceramic fuel cell membrane reactor,” *Journal of Energy Chemistry*, vol. 77, pp. 359–368, Feb. 2023, doi: 10.1016/j.jechem.2022.10.035.
[78] J. Norman, A. Yousuf, C. Duan, H. Ding, H. Shabgard, and P. Kazempoor, “Dual-function protonic ceramic fuel cell for efficient natural gas conversion to power and chemicals,” *Chemical Engineering Journal*, vol. 507, p. 160527, Mar. 2025, doi: 10.1016/j.cej.2025.160527.

[79] N. H. Hadi *et al.*, “Understanding the Impact of Sintering Temperature on the Properties of Ni–BCZY Composite Anode for Protonic Ceramic Fuel Cell Application,” *Processes*, vol. 11, no. 7, Art. no. 7, Jul. 2023, doi: 10.3390/pr11071902.
[80] H. Ding *et al.*, “Self-sustainable protonic ceramic electrochemical cells using a triple conducting electrode for hydrogen and power production,” *Nat Commun*, vol. 11, no. 1, p. 1907, Apr. 2020, doi: 10.1038/s41467-020-15677-z.
[81] L. A. Jolaoso, J. Asadi, C. Duan, and P. Kazempoor, “A novel green hydrogen production using water-energy nexus framework,” *Energy Conversion and Management*, vol. 276, p. 116344, Jan. 2023, doi: 10.1016/j.enconman.2022.116344.
[82] Z. Li *et al.*, “Revealing interactions between the operating parameters of protonic ceramic electrolysis cell: A modelling study,” *Applied Energy*, vol. 351, p. 121886, Dec. 2023, doi: 10.1016/j.apenergy.2023.121886.
[83] C. Wang *et al.*, “Performance analysis and optimization of a zero-emission solar-driven hydrogen production system based on solar power tower plant and protonic ceramic electrolysis cells,” *International Journal of Hydrogen Energy*, vol. 83, pp. 1415–1428, Sep. 2024, doi: 10.1016/j.ijhydene.2024.08.174.
[84] D. Gussow, “Natural Gas Specs Sheet,” Specifications List R040609, Jun. 2024. Accessed: Jun. 09, 2004. [Online]. Available: https://www.naesb.org/pdf2/wgq_bps100605w2.pdf
[85] Y. A. Çengel and M. A. Boles, *Thermodynamics: an engineering approach*, 8. edition in SI units. New York, NY: McGraw-Hill Education, 2015.
[86] M. Bahrami, “Chemical Reactions Definitions Air Fuel Ratio,” Simon Fraser University. [Online]. Available: https://www.google.com/url?client=internal-element-cse&cx=016365272213985876953:yqbmx6rj4ze&q=https://www.sfu.ca/~mbahrami/ENSC%2520461/Notes/Chemical%2520Reactions.pdf&sa=U&ved=2ahUKEwjnuN7g2P6LAxU2MEQIHWwuL-IQFnoECAEQAQ&usg=AOvVaw0vQKaJcxdawUFRR19dtSEX
[87] S. C. Hill and L. Douglas Smoot, “Modeling of nitrogen oxides formation and destruction in combustion systems,” *Progress in Energy and Combustion Science*, vol. 26, no. 4, pp. 417–458, Aug. 2000, doi: 10.1016/S0360-1285(00)00011-3.
[88] C. T. Bowman, “Kinetics of nitric oxide formation incombustion processes,” *Symposium (International) on Combustion*, vol. 14, no. 1, pp. 729–738, Jan. 1973, doi: 10.1016/S0082-0784(73)80068-2.
[89] “AJAX,” Cooper Machinery Services. Accessed: Mar. 08, 2025. [Online]. Available: https://www.cooperservices.com/engines-and-compressors/brands/AJAX/
[90] “Stainless Steel Pressure Transducers - PX309 Series.” Accessed: Mar. 10, 2025. [Online]. Available: https://www.dwyeromega.com/en-us/general-purpose-stainless-steel-pressure-transducers/p/PX309
[91] ChampionX, “Portable Compressor Analyzer - Portable Engine Analyzer | ChampionX.” Accessed: Mar. 10, 2025. [Online]. Available: https://www.championx.com/products-and-solutions/digital-control-automation-and-optimization/windrock-equipment-monitoring-optimization/portable-analysis/
[92] “Model FT1 | Fox Thermal Products | Fox Thermal.” Accessed: Mar. 10, 2025. [Online]. Available: https://www.foxthermal.com/products/ft1.php
[93] “Micro Motion F025S Coriolis Meter, 1/4 Inch (DN6), 316L Stainless Steel | EMR.” Accessed: Mar. 10, 2025. [Online]. Available: https://www.emerson.com/en-us/catalog/micro-motion-sku-

f025s?fetchFacets=true#facet:&partsFacet:&modelsFacet:&facetLimit:&searchTerm:&partsSearchTerm:&modelsSearchTerm:&productBeginIndex:0&partsBeginIndex:0&modelsBeginIndex:0&orderBy:&partsOrderBy:&modelsOrderBy:&pageView:list&minPrice:&maxPrice:&pageSize:&facetRange:&

[94] "Thermocouple Probes with Many Industrial Protection Heads." Accessed: Mar. 10, 2025. [Online]. Available: https://www.dwyeromega.com/en-us/thermocouple-probes-with-industrial-protection-heads-choices/p/NB1-ICIN-INDUST-TC

[95] "MultiGas 2030 FTIR Gas Analyzers." Accessed: Mar. 10, 2025. [Online]. Available: https://www.mks.com/f/multigas-2030g-ftir-gas-analyzer

[96] "NOxCANt Kit," ECM. Accessed: Oct. 16, 2023. [Online]. Available: https://ecm-co.com/product/noxcant-kit/

[97] T. Nguyen, "The Impact of Hydrogen Blending on Emissions and Performance of a Naturally Aspirated Engine," University of Oklahoma, Norman, OK, 2023.

[98] J.-R. Youn *et al.*, "Highly efficient Co-added Ni/CeO2 catalyst for co-production of hydrogen and carbon nanotubes by methane decomposition," *Fuel Processing Technology*, vol. 263, p. 108130, Nov. 2024, doi: 10.1016/j.fuproc.2024.108130.

[99] P. G. Lustemberg, Z. Mao, A. Salcedo, B. Irigoyen, M. V. Ganduglia-Pirovano, and C. T. Campbell, "Nature of the Active Sites on Ni/CeO2 Catalysts for Methane Conversions," *ACS Catal.*, vol. 11, no. 16, pp. 10604–10613, Aug. 2021, doi: 10.1021/acscatal.1c02154.

[100] J. H. Lee and D. L. Trimm, "Catalytic combustion of methane," *Fuel Processing Technology*, vol. 42, no. 2, pp. 339–359, Apr. 1995, doi: 10.1016/0378-3820(94)00091-7.

[101] D. L. Hoang and S. H. Chan, "Modeling of a catalytic autothermal methane reformer for fuel cell applications," *Applied Catalysis A: General*, vol. 268, no. 1, pp. 207–216, Aug. 2004, doi: 10.1016/j.apcata.2004.03.056.

[102] L. Fan, A. Mokhov, S. A. Saadabadi, N. Brandon, and P. V. Aravind, "Methane steam reforming reaction in solid oxide fuel cells: Influence of electrochemical reaction and anode thickness," *Journal of Power Sources*, vol. 507, p. 230276, Sep. 2021, doi: 10.1016/j.jpowsour.2021.230276.

[103] A. Thallam Thattai, L. van Biert, and P. V. Aravind, "On direct internal methane steam reforming kinetics in operating solid oxide fuel cells with nickel-ceria anodes," *Journal of Power Sources*, vol. 370, pp. 71–86, Dec. 2017, doi: 10.1016/j.jpowsour.2017.09.082.

[104] Y. Gao, M. Jiang, L. Yang, Z. Li, F.-X. Tian, and Y. He, "Recent progress of catalytic methane combustion over transition metal oxide catalysts," *Front. Chem.*, vol. 10, Aug. 2022, doi: 10.3389/fchem.2022.959422.

[105] "14.4.2: Water-Gas Shift Reaction," Chemistry LibreTexts. Accessed: Apr. 11, 2024. [Online]. Available: https://chem.libretexts.org/Bookshelves/Inorganic_Chemistry/Inorganic_Chemistry_(LibreTexts)/14%3A_Organometallic_Reactions_and_Catalysis/14.04%3A_Heterogeneous_Catalysts/14.4.02%3A_Water-Gas_Shift_Reaction

[106] E. Baraj, K. Ciahotný, and T. Hlinčík, "The water gas shift reaction: Catalysts and reaction mechanism," *Fuel*, vol. 288, p. 119817, Mar. 2021, doi: 10.1016/j.fuel.2020.119817.

[107] R. Prins, A. Wang, and X. Li, *Introduction to Heterogeneous Catalysis*. in Advanced Textbooks in Chemistry. WORLD SCIENTIFIC (EUROPE), 2015. doi: 10.1142/q0024.

[108] L. Mingyi, Y. Bo, X. Jingming, and C. Jing, "Thermodynamic analysis of the efficiency of high-temperature steam electrolysis system for hydrogen production," *Journal of Power Sources*, vol. 177, no. 2, pp. 493–499, Mar. 2008, doi: 10.1016/j.jpowsour.2007.11.019.

[109] W. Addy Majewski and Hannu Jääskeläinen, “Methane Oxidation Catalysts,” DieselNet. Accessed: Apr. 10, 2024. [Online]. Available: https://dieselnet.com/tech/catalyst_methane_oxidation.php
[110] Md. S. A. Sher Shah, C. Oh, H. Park, Y. J. Hwang, M. Ma, and J. H. Park, “Catalytic Oxidation of Methane to Oxygenated Products: Recent Advancements and Prospects for Electrocatalytic and Photocatalytic Conversion at Low Temperatures,” *Advanced Science*, vol. 7, no. 23, p. 2001946, 2020, doi: 10.1002/advs.202001946.
[111] P. Münster and H. J. Grabke, “Kinetics of the steam reforming of methane with iron, nickel, and iron-nickel alloys as catalysts,” *Journal of Catalysis*, vol. 72, no. 2, pp. 279–287, Dec. 1981, doi: 10.1016/0021-9517(81)90010-5.
[112] P. Ebrahimi, A. Kumar, and M. Khraisheh, “A review of recent advances in water-gas shift catalysis for hydrogen production,” *emergent mater.*, vol. 3, no. 6, pp. 881–917, Dec. 2020, doi: 10.1007/s42247-020-00116-y.
[113] L. Bobrova *et al.*, “Water–Gas Shift Reaction over Ni/CeO2 Catalysts,” *Catalysts*, vol. 7, no. 10, Art. no. 10, Oct. 2017, doi: 10.3390/catal7100310.
[114] “Basics of Soil Bulk Density - Oklahoma State University.” Accessed: Apr. 17, 2025. [Online]. Available: https://extension.okstate.edu/fact-sheets/basics-of-soil-bulk-density.html
[115] H. S. Fogler, *Essentials of chemical reaction engineering*. in Prentice Hall international series in the physical and chemical engineering sciences. Upper Saddle River, NJ Munich: Prentice Hall, 2011.
[116] V. Palma, E. Meloni, S. Renda, and M. Martino, “Catalysts for Methane Steam Reforming Reaction: Evaluation of CeO2 Addition to Alumina-Based Washcoat Slurry Formulation,” *C*, vol. 6, no. 3, Art. no. 3, Sep. 2020, doi: 10.3390/c6030052.
[117] J. Chen *et al.*, “Mechanistic Understanding of Methane Combustion over Ni/CeO2: A Combined Experimental and Theoretical Approach,” *ACS Catal.*, vol. 11, no. 15, pp. 9345–9354, Aug. 2021, doi: 10.1021/acscatal.1c01088.
[118] K. Ferguson, A. Dubois, K. Albrecht, and R. J. Braun, “High performance protonic ceramic fuel cell systems for distributed power generation,” *Energy Conversion and Management*, vol. 248, p. 114763, Nov. 2021, doi: 10.1016/j.enconman.2021.114763.
[119] J. M. Sierra, S. J. Pathiyamattom, and S. Gamboa, “Study of Activation Losses and Ohmic Resistance in a PEM Fuel Cell using Computational Fluid Dynamics,” *ECS Trans.*, vol. 20, no. 1, p. 395, Nov. 2009, doi: 10.1149/1.3268407.
[120] D. A. Noren and M. A. Hoffman, “Clarifying the Butler–Volmer equation and related approximations for calculating activation losses in solid oxide fuel cell models,” *Journal of Power Sources*, vol. 152, pp. 175–181, Dec. 2005, doi: 10.1016/j.jpowsour.2005.03.174.
[121] M. Ni, M. K. H. Leung, and D. Y. C. Leung, “A modeling study on concentration overpotentials of a reversible solid oxide fuel cell,” *Journal of Power Sources*, vol. 163, no. 1, pp. 460–466, Dec. 2006, doi: 10.1016/j.jpowsour.2006.09.024.
[122] A. K. Baral, S. Choi, B. K. Kim, and J.-H. Lee, “Processing and characterizations of a novel proton-conducting BaCe0.35Zr0.50Y0.15O3-δ electrolyte and its nickel-based anode composite for anode-supported IT-SOFC,” *Mater Renew Sustain Energy*, vol. 3, no. 4, p. 35, Aug. 2014, doi: 10.1007/s40243-014-0035-4.

[123] K. Huang, P. Y. Hou, and J. B. Goodenough, “Reduced area specific resistance for iron-based metallic interconnects by surface oxide coatings,” *Materials Research Bulletin*, vol. 36, no. 1, pp. 81–95, Jan. 2001, doi: 10.1016/S0025-5408(01)00506-2.
[124] P. Kazempoor and R. J. Braun, “Model validation and performance analysis of regenerative solid oxide cells for energy storage applications: Reversible operation,” *International Journal of Hydrogen Energy*, vol. 39, no. 11, pp. 5955–5971, Apr. 2014, doi: 10.1016/j.ijhydene.2014.01.186.
[125] J. O. Bockris and Z. Nagy, “Symmetry factor and transfer coefficient. A source of confusion in electrode kinetics,” *J. Chem. Educ.*, vol. 50, no. 12, p. 839, Dec. 1973, doi: 10.1021/ed050p839.
[126] X. Yang *et al.*, “Ni−CeO2 Heterostructure Promotes Hydrogen Evolution Reaction via Tuning of the O−H Bond Length of Adsorbed Water at the Electrolyte/Electrode Interface,” *ChemSusChem*, vol. 16, no. 17, p. e202300348, 2023, doi: 10.1002/cssc.202300348.
[127] H. Zhu, S. Ricote, and R. J. Kee, “Faradaic efficiency in protonic-ceramic electrolysis cells,” *J. Phys. Energy*, vol. 4, no. 1, p. 014002, Jan. 2022, doi: 10.1088/2515-7655/ac3729.
[128] L. Zhang *et al.*, “Efficient Hydrogen Evolution Electrocatalysis at Alkaline pH by Interface Engineering of Ni2P–CeO2,” *Inorg. Chem.*, vol. 57, no. 2, pp. 548–552, Jan. 2018, doi: 10.1021/acs.inorgchem.7b02665.
[129] H. Zhu and R. J. Kee, “Modeling Protonic-Ceramic Fuel Cells with Porous Composite Electrodes in a Button-Cell Configuration,” *J. Electrochem. Soc.*, vol. 164, no. 13, pp. F1400–F1411, 2017, doi: 10.1149/2.0591713jes.
[130] “Key properties of nickel.” Accessed: Apr. 17, 2025. [Online]. Available: https://nickelinstitute.org/en/nickel-applications/properties-of-nickel
[131] “CX-032963: Highly Replicable, and Integrated System for Mitigating Methane Emissions from Natural Gas-fired Lean-Burn,” Energy.gov. Accessed: Apr. 06, 2025. [Online]. Available: https://www.energy.gov/nepa/articles/cx-032963-highly-replicable-and-integrated-system-mitigating-methane-emissions